FEDERAL UNIVERSITY OF SÃO CARLOS
CENTER OF EXACT SCIENCE AND TECHNOLOGY
GRADUATE PROGRAM IN MATERIALS SCIENCE AND ENGINEERING

MULTILAYERED REFILL FRICTION STIR SPOT WELDING OF AA2024 AND ALUMINUM FOILS FOR ELECTRIC VEHICLE BATTERY APPLICATION

Dennis Balbino Gera

São Carlos-SP
2020

FEDERAL UNIVERSITY OF SÃO CARLOS
CENTER OF EXACT SCIENCE AND TECHNOLOGY
GRADUATE PROGRAM IN MATERIALS SCIENCE AND ENGINEERING

MULTILAYERED REFILL FRICTION STIR SPOT WELDING OF AA2024 AND ALUMINUM FOILS FOR ELECTRIC VEHICLE BATTERY APPLICATION

Dennis Balbino Gera

Masters Dissertation presented to Graduate Program in Materials Science and Engineering (PPGCEM) in partial fulfillment of the requirements for the MASTER OF SCIENCE DEGREE IN MATERIALS SCIENCE AND ENGINEERING.

Supervisor: Prof. Dr. Nelson Guedes de Alcântara
Co-Supervisor: Prof. Dr. Athos Henrique Plaine
Funding Agency: CNPq – Process no. 134360/2019-2

São Carlos - SP
2020

DEDICATION

To my beloved family.

VITAE

Bachelor's degree in Materials Engineering from UFSCar (2019)

UNIVERSIDADE FEDERAL DE SÃO CARLOS

Centro de Ciências Exatas e de Tecnologia
Programa de Pós-Graduação em Ciência e Engenharia de Materiais

Folha de Aprovação

Defesa de Dissertação de Mestrado do candidato Dennis Balbino Gera, realizada em 06/11/2020.

Comissão Julgadora:

Prof. Dr. Nelson Guedes de Alcântara (UFSCar)

Prof. Dr. Guilherme Zepon (UFSCar)

Prof. Dr. Jorge Fernandez dos Santos (WMP/HZG)

O presente trabalho foi realizado com apoio da Coordenação de Aperfeiçoamento de Pessoal de Nível Superior - Brasil (CAPES) - Código de Financiamento 001.
O Relatório de Defesa assinado pelos membros da Comissão Julgadora encontra-se arquivado junto ao Programa de Pós-Graduação em Ciência e Engenharia de Materiais.

ACKNOWLEDGMENTS

This work marks the end of my journey as a Master of Science Student in materials science and engineering. I could not have come so far without so many whom I feel obliged to acknowledge.

First and foremost, I want to thank my entire family for everything. My parent's past struggles have created opportunities for me and my siblings, making us who we are today. Furthermore, the importance they gave to education during my upbringing made me appreciate every opportunity and always look towards the next step.

My brothers have helped me in ways they probably don't understand. Thank you, David, for always being that beam of joy innate in children that could soften any moment of hardship. And thank you, Kevin, for sharing your struggles and allowing me to share mines. Our discussions during all this time have helped me push forward and continuously improve my worldview.

I want to thank my friends and close ones. Every moment of joy is only experienced if shared with real friends. So, thank you all for being there when I needed it the most. Know that every one of you inspires me in some way and that I wish you nothing but absolute happiness and success.

I want to thank my girlfriend, Júlia, for being so compassionate, loving, and admirable. You make me strive to be a better person, and I cannot thank you enough for all the moments we share.

Lastly, I want to thank Prof. Dr. Nelson, Prof. Dr. Jorge, and Helmholtz-Zentrum Geesthacht for allowing me to work on this project, which has enriched me as a professional, as an engineer, and as a person.

I am also grateful to CNPq - Conselho Nacional de Desenvolvimento Científico e Tecnológico for the grant under process nº 134360/2019-2. This study was financed in part by the Coordenação de Aperfeiçoamento de Pessoal de Nível Superior - Brasil (CAPES) - Finance Code 001.

ABSTRACT

Different processes are currently being used to weld aluminum and copper in a multilayered configuration in battery pouches for the automotive industry. The methods most used are mechanical joint, ultrasonic welding, laser welding, and resistance spot welding. However, these techniques have limitations such as added mass, cracks, intermetallic compound formation, and thermal conductivity. Refill Friction Stir Spot Welding (refill FSSW) is an alternative process for welding overlap joints. In this work, the microstructure and properties of a multilayered weld of AA2024/CP-Al produced by refill FSSW were investigated. CP-Al foils and AA2024 sheets with thicknesses of 0.013 mm and 0.3 mm, respectively, were used. Statistical analysis was conducted to assess the influence of processing parameters on the joint's mechanical properties, process temperature, contact resistance, and microstructural features. Specimens with up to 50 layers of CP-Al foils were successfully welded. Response surface methodology indicated that plunge speed was significantly influential to LSS and process temperature; plunge speed was found to influence process temperature significantly, and rotational speed showed no influence in any of the investigated properties. The one-factor-at-a-time analysis showed that plunge depth, plunge speed, and rotational speed alter the AA2024 island's morphology, the bottom sheet's deformation, and the number of unbonded interfaces in the center of the weld. Microstructural analysis depicted intermetallic compounds, eutectic constituents, and unbonded foils; however, these features were not detrimental to the weld's mechanical properties. A maximum LSS of 1890 N, and minimum process temperature and contact resistance of 167ºC and 0.183 mΩ, respectively, were found. Therefore, mechanical properties were superior to aerospace application requisites, and contact resistance values are smaller than conventional lithium-ion batteries' internal resistance. Infrared analysis showed that temperatures below 80ºC are obtained at 30 mm from the welding tool, indicating the possibility of using refill FSSW in batteries while avoiding cell degradation.

Keywords: Friction Welding; Refill FSSW; multilayered; contact resistance; battery; CP-Al foils; AA2024 alloy.

RESUMO

SOLDAGEM A PONTO POR FRICÇÃO EM MULTICAMADAS DE FOLHAS DE ALUMÍNIO E AA2024 PARA APLICAÇÃO EM BATERIAS DE CARROS ELÉTRICOS

Diferentes processos são usados atualmente para soldar multicamadas de alumínio e cobre em bolsas de bateria para a indústria automotiva. A soldagem por refill Friction Stir Spot Welding (Refill FSSW) é um processo alternativo para soldar juntas de sobreposição. Neste trabalho, a microestrutura e as propriedades de uma solda multicamadas de AA2024/CP-Al produzida por refill FSSW foram investigadas. Foram utilizadas folhas de CP-Al e chapas de AA2024 com espessuras de 0,013 mm e 0,3 mm, respectivamente. Uma análise estatística foi conduzida para avaliar a influência dos parâmetros de processamento nas propriedades mecânicas, temperatura do processo, resistência de contato e características microestruturais da junta. Amostras com até 50 camadas de folhas de CP-Al foram soldadas com sucesso. A metodologia de superfície de resposta indicou que a velocidade de penetração influencia significativamente o LSS e a temperatura do processo; a velocidade de penetração tem influência significativa na temperatura do processo; e a velocidade de rotação não influenciou em nenhuma das propriedades investigadas. A análise de um fator por vez mostrou que os parâmetros do processo investigados alteram a morfologia da ilha AA2024, a deformação da chapa inferior e o número de interfaces não aderidas no centro da solda. A análise microestrutural representou compostos intermetálicos, constituintes eutéticos e folhas não aderidas no centro da solda; no entanto, isso não prejudicou as propriedades mecânicas da solda. Também se encontrou um LSS máximo de 1890 N, e uma temperatura mínima de processo e resistência de contato de 167ºC e 0,183 mΩ, respectivamente. Assim, as propriedades mecânicas foram superiores aos requisitos de aplicação aeroespacial e os valores de resistência de contato são menores do que a resistência interna das baterias convencionais de íon-lítio. A análise de infravermelho mostrou que temperaturas abaixo de 80ºC são obtidas a 30 mm da ferramenta de soldagem.

Palavras-chave: Soldagem; Estado sólido; Refill FSSW; multicamadas; resistência de contato; bateria; folhas de CP-Al; liga AA2024.

PUBLICATIONS

Suhuddin, Uceu ; Gera, Dennis ; Alcantara, Nelson ; dos Santos, Jorge . Welding Multilayer Materials by Refill Friction Stir Spot Welding. The Minerals, Metals & Materials Series. 1ed.: Springer International Publishing, 2019, v. , p. 245-253.

x

TABLE OF CONTENTS

LIST OF TABLES

LIST OF FIGURES

SYMBOLS AND ABBREVIATIONS

AA	Aluminum Alloy
ANOVA	Analysis of Variance
BBD	Box-Behnken Design
BEV	Battery Electric Vehicle
BM	Base Metal
CCD	Central Composite Design
CR	Contact Resistance
DEMa	Department of Materials Science
DT	Dwell Time
EDS	Energy Dispersive X-ray Spectroscopy
EV	Electric Vehicle
FR	Friction Riveting
FSpW	Friction Spot Welding
FSW	Friction Stir Welding
	Green House Gases
H_0	Null Hypotheses
HAZ	Heat Affected Zone
HEV	Hybrid Electric Vehicle
HZG	Helmholtz-Zentrum Geesthacht
IMC	Intermetallic Compound
LSS	Lap Shear Strength
LBW	Laser Beam Welding
MS	Mean Square
OM	Optical Microscopy
PD	Plunge Depth
PS	Plunge Speed
PHEV	Plug-in Hybrid Electric Vehicles GHG
FSSW	Friction Stir Spot Welding
RS	Rotational Speed
RSM	Response Surface Methodology
RSW	Resistance Spot Welding
SEM	Scanning Electron Microscopy
Sigma	Variance
SS_T	Total Sum of Squares
SS_E	Sum of Squares due to Error
SZ	Stir Zone
TMAZ	Thermal
UTS	Ultimate Tensile Strength
USW	Ultrasonic Welding
WF	Welding Force

YS Yield Strength

1 INTRODUCTION

As global warming continues to threaten the planet's stability, scientists and entrepreneurs are increasingly devoted to finding new ways to reduce greenhouse gas (GHG) emissions, the primary cause of climate change. Currently, one-third of all GHG emissions are accounted to the transportation sector [1], thus attracting attention from researchers and developers around the world to replace gasoline-powered vehicles with electric vehicles (EVs) [2, 3]. However, compared to gasoline-powered cars, EVs still have many limitations, such as range, long refueling time, and higher acquisition costs [4]. For this reason, a high degree of automation on battery manufacturing is required to make this technology more accessible.

The majority of EVs battery currently consists of Li-ion technology. However, the battery type differs from each car manufacturer to another; some use pouches, others use prismatic or cylindrical, each offering its ad- and disadvantage. The cylindrical cells, the first format of Li-ion cells, are easy to manufacture and present good mechanical stability but are less volumetric efficient than prismatic cells. Prismatic cells make optimal use of space using the layered approach, surpassed only by the pouch cell, which reaches 90-95 percent packaging efficiency, the highest among battery packs [5]. The latter, illustrated in Figure 1.1, rather than using a metallic cylinder and glass-to-metal electric feed through, uses conductive foil-tabs welded to the electrodes and then brought together in a fully sealed way.

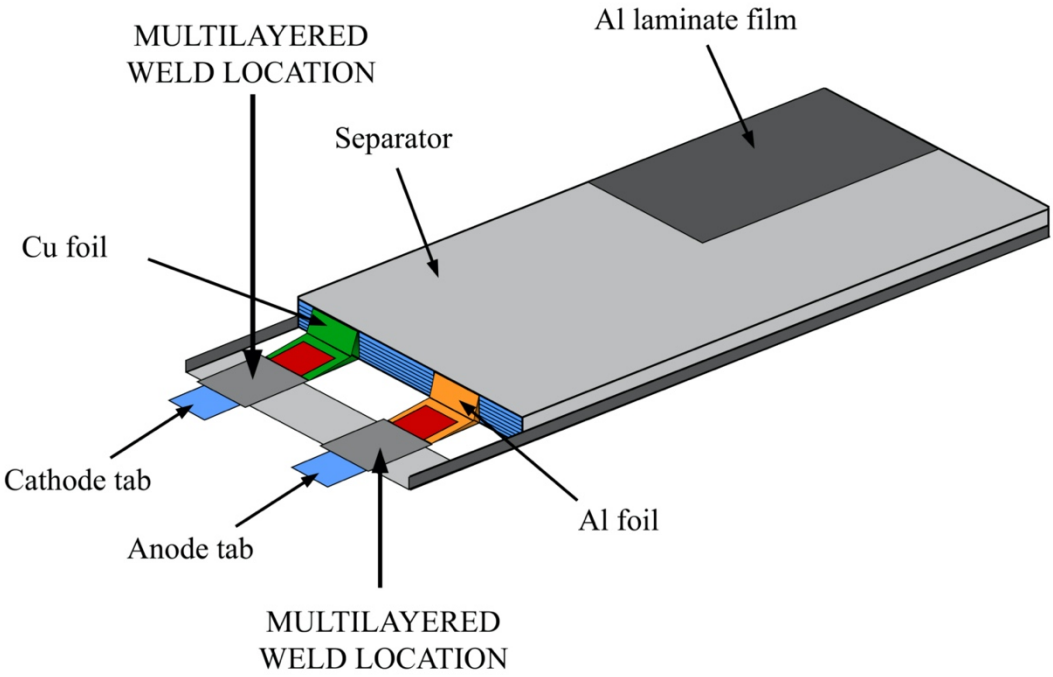

Figure 1.1 – Schematic representation of a pouch cell battery. Location of welds included. Credit to the author.

The lithium-ion battery is composed of a positive and negative electrode, usually a pure lithium oxide and graphite, an electrolyte solution that allows lithium ions to flow freely, a separator permeable only to ions, avoiding short circuit, and conductive surfaces, usually aluminum and copper [6]. The process of joining a battery with a pouch cell configuration consists of four steps, as shown in Figure 1.2. At the cell level, there are alternating electrodes and conductive surfaces. These electrodes are welded to a standard conductive tab, indicated in Figure 1.1, to create a cell, which will later be sealed. The number of current collectors typically welded in an electrode tab range from 1 – 100 layers with a thickness of 10 μm - 30 μm [7].

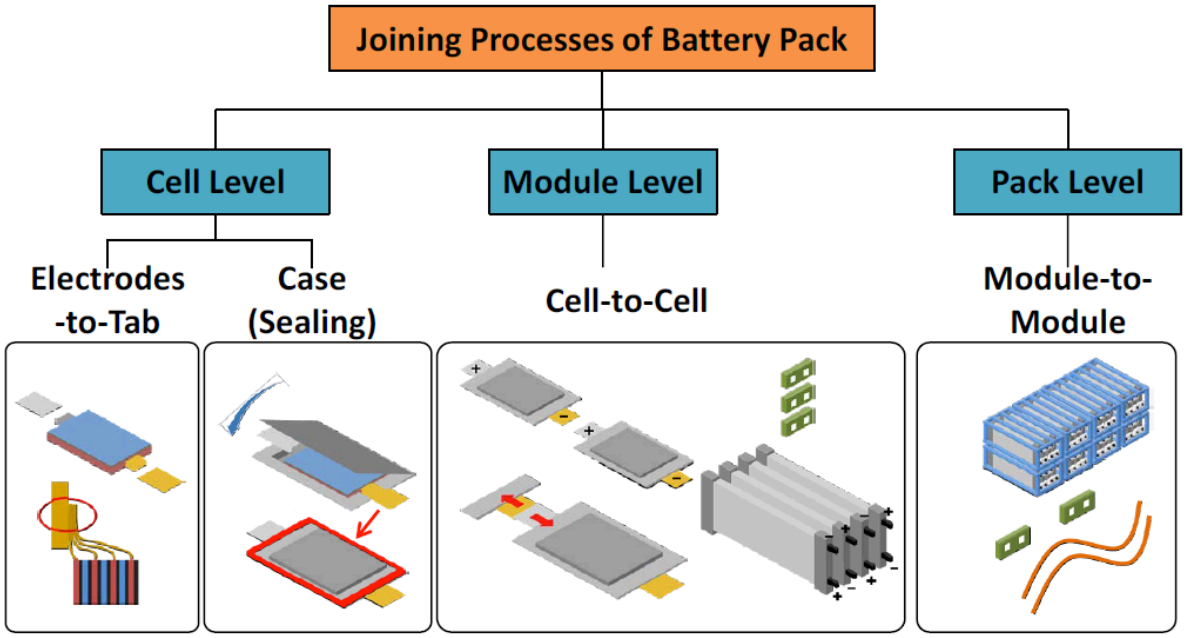

Figure 1.2 – Joining process of a battery pack with a pouch-type cell [6].

Many processes are being used for welding and joining aluminum and copper, in a multilayered configuration, to a conductive tab in battery pouches [8]. The methods differ from one car manufacturer to another, but the most commonly used are mechanical joint, ultrasonic welding, laser welding, and resistance spot welding [6]. However, these techniques have limitations such as added mass, cracks, intermetallic compound formation, and thermal conductivity, respectively.

Refill Friction Stir Spot Welding (refill FSSW), also known as Friction Spot Welding (FSpW), is an alternative process for welding overlap joints. This technique has proved to be feasible in welding similar and dissimilar materials of different thicknesses with good mechanical properties [9–11]. Before elaborating this dissertation, no studies have been published in the literature investigating the use of refill FSSW in multilayer conductive materials such as Al and Cu. Therefore, there is a lack of knowledge concerning the use of this technique in such an application.

Due to the limitations presented by the techniques currently used to perform welding on batteries, a technical investigation of refill FSSW on multilayered conductive materials is convenient. In the referred study, such investigation assessed the technical feasibility of welding multilayered aluminum alloys

through refill FSSW. Since the number of current collectors typically welded in an electrode tab range from 1 – 100 layers with a thickness of 10 μm - 30 μm, this work used 50 foils of commercial aluminum, with a thickness of 13 μm, in between two AA2024-T3 sheets. A design of experiments (DoE) approach was used to optimize the processing parameters and study the influence of such parameters on the joint properties. Also, microstructural analysis of the multilayered joint was conducted to correlate the processing parameters to the microstructural transformations and metallurgical zones encountered in the welded specimen. Lastly, comparisons between refill FSSW and the welding techniques most commonly used in the manufacture of batteries were made by analyzing the latter's literature. Thus, this work is relevant not only to evaluate the use of refill FSSW for welding multilayered materials – becoming a standpoint for further works analyzing multilayered refill FSSW welds – but also to evaluate the use of such technology on battery applications – becoming a reference for electric vehicle battery manufacturers seeking alternative welding techniques.

2 OBJECTIVES

This work's primary objective was to study the technical feasibility of using Refill Friction Stir Spot Welding for obtaining a multilayered joint of commercially pure aluminum foils with AA2024-T3 sheets, for electric battery applications. Therefore, the objectives can be structured into the following:

- Assess the technical feasibility of welding multilayered aluminum alloys through Refill Friction Stir Spot Welding, proposing a novel technique for welding electric vehicle batteries.
    - Through the Design of Experiments (DOE), optimize the processing parameters to attain the best properties desired in electric batteries. That is, high mechanical properties, low process temperature, and low contact resistance.
    - Study the influence of processing parameters, through statistical analysis, on the weld's mechanical and electrical properties, and process temperature. Hence, enabling the evaluation of the processing-properties relationship for the multilayered-aluminum configuration.
    - Investigate the microstructural transformations that occur during the welding process and how these transformations define the metallurgical zones of the system. Here, the aim is to perform a microstructural characterization and correlate it to the processing parameters and material properties previously studied.
    - Approach a technological bias based on making comparisons with the welding techniques most used in the manufacture of batteries. These comparisons are based on published data and aim to critically analyze mainly the mechanical properties, process temperatures, and electrical resistivity of welds.

3 LITERATURE REVIEW

3.1 Battery Challenges in the Automotive Industry

Automotive battery packs for electric vehicles (EV), hybrid electric vehicles (HEV), and plug-in hybrid electric vehicles (PHEV) typically consist of a large number of battery cells, sometimes several hundred, even thousands, to meet desired power and capacity needs. These cells must be assembled with robust mechanical and electrical joints. Several cells are usually joined to form a module. There are tens of modules in a battery pack [12].

As a result, a significant amount of joining, such as welding, is needed to deliver electricity in a battery pack. It is not easy to join such many battery cells because of the difficulty with welding multiple layers of thin, highly conductive, and dissimilar materials, with 100% reliability. Also, automobile battery is exposed to harsh driving environments such as vibration, severe temperature, and possible crash, affecting battery performance and safety. Furthermore, hundreds of thousands of battery packs will be produced annually for automotive volume production. As such, batteries must be assembled using robust joining processes. The development of effective joining technologies for battery manufacturing is becoming an essential condition for auto manufacturers as the battery pack's size increases for battery electric vehicles (BEVs), new manufacturing challenges are being presented. Currently, most auto manufacturers are entering the BEV market, but they have difficulties performing battery manufacturing due to the lack of experience or precedent technologies, especially battery joining methods.

In general, ultrasonic, laser, resistance spot welding, and mechanical joining are used by car manufacturers to weld and join multilayered aluminum and copper alloys to a conducting tab in battery pouches.

Mechanical joining can be classified into two distinct groups: fasteners and integral joints. While fasteners include bolts, screws, and rivets, integral joints are made up of seams or snap-fits, allowing an attachment of the components. In battery pack manufacturing, welding is an effective solution to small-scale joining, such as in connecting cells to tabs. By avoiding the use of fasteners or snap-fits, the battery manufacturer avoids adding mass to the component and requiring

intensive labor [13]. However, due to battery maintenance and service concerns, mechanical joining is preferred when performing module-to-module joining. Not only does this grant ease of disassembly, but also, no heat source is used.

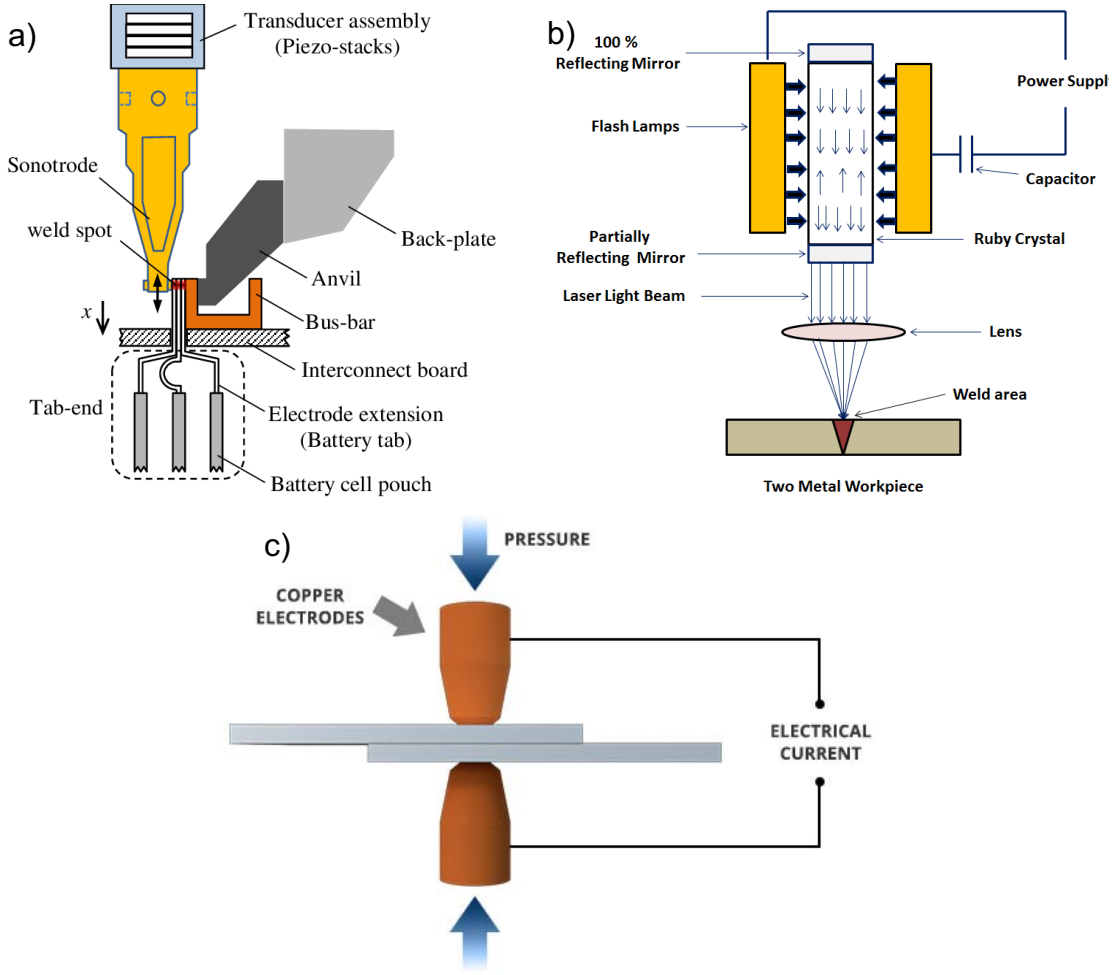

Figure 3.1 – Schematic of a (a) ultrasonic welding[14]*, (b) laser welding*[15]*, and (c) resistance spot welding setup* [16].

Ultrasonic welding (USW), Figure 3.1a, is a solid-state joining process that presses two or more materials together with a pressure *p* and rubs them using an ultrasonic vibration *u(t)*. During the process, the vibrations disrupt the oxides and contaminants on the material's surface, leaving pure metals in contact with each other. Further vibrations cause these metals to plasticize due to the shearing forces, while longer welding times lead to increased pure metal surfaces and temperature. Therefore, ultrasonic welding is excellent for materials with low hardness and surface roughness, such as copper and aluminum. It has also been

seen that this technique can weld multilayered materials, given enough time, since the vibrations weld layer to layer.

Nonetheless, it has been reported that this process's vibrations can damage the pouch cell, primarily when the conductors inside the battery pouch have also been ultrasonically welded. Besides, further studies and metallographic analysis from ultrasonic welds show tiny spots of connection between the materials, generally limited to the area immediately below the weld indentation. An increase of welding time and pressure would increase this welded area [17]; however, it would also lead to cracks due to the prolonged time the material is under mechanical vibrations. Consequently, the welds produced by UW usually present higher contact resistances.

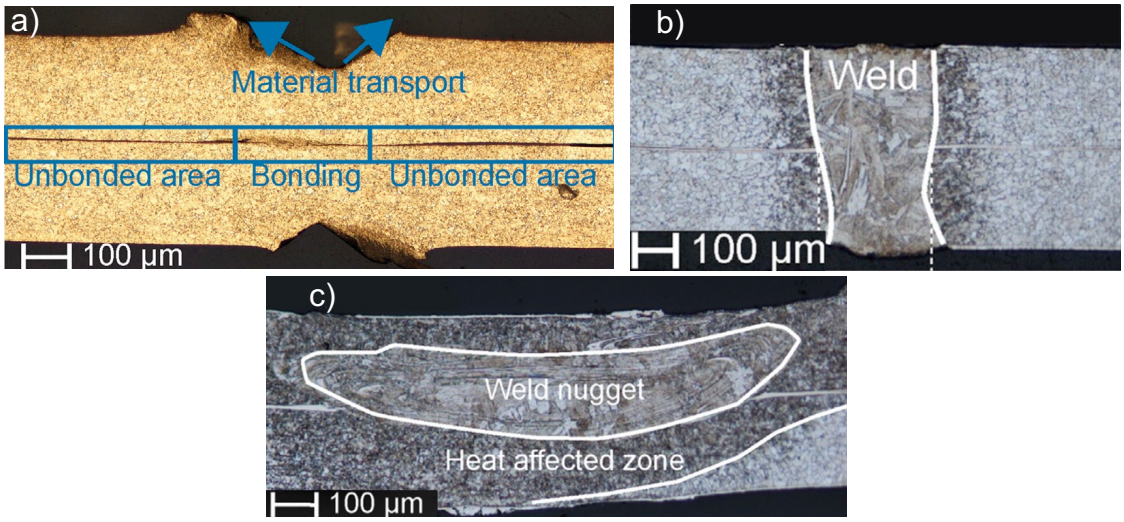

Figure 3.2 – Representative micrographs of welds produced by (a) ultrasonic welding, (b) laser welding, and (c) resistance spot welding setup [18].

Laser beam welding (LBW), Figure 3.1b, uses electromagnetic waves' absorption to heat the materials. This allows a speedy welding process in which it is possible to limit heat input and optimize the weld's geometry through process parameters. However, this technique melts the materials, creating a metallurgical system with different base material properties. This can be a problem depending on the solubility limit of the metals. If the limit is low, then intermetallic phases can be formed, compromising the weld's mechanical properties. Besides, this technique provides a more hazardous work environment since spatters can be expulsed from the keyhole, and the reflection of the laser beam can damage objects in close vicinity.

Resistance spot welding (RSW), Figure 3.1c, uses the heat generated from the material's resistance to the passage of electric current to join two metals. This technique's main characteristic is that only a small volume of the workpiece is melted and fused. Due to the welding mechanism, materials with high resistivity are more accessible to weld then those with low resistivity. This process is limited by the material's thickness and conductivity. So, although resistance spot welding can easily weld steel, it suffers to weld aluminum and copper alloys.

Table 3.1 – Mechanical, thermal, and electrical properties of welds performed by different techniques [18]

	Resistance Spot Welding	**Ultrasonic Welding**	**Laser Beam Welding**
Min. Electrical CR (mΩ)	0.167	0.169	0.130
Max. UTS (N)	316.78	661.32	876.80
Highest T at cell terminal (°C)	31.0	110.7	86.8
Highest T at cylinder barrel (°C)	25.0	55.2	32.5

Brand et al. [18] performed a quantitative analysis of welded test samples using the three techniques mentioned above to reveal the ultimate tensile strength, contact resistance, and heat input into a battery cell. A summary of his data is presented in Table 3.1. Because laser beam welding allows the optimization of weld geometry, this technique presented the highest UTS and lowest contact resistance (CR). Resistance spot welding showed the lowest tensile strength and high CR due to the generation of voids inside the weld nugget. Not only do the voids act as a barrier to the passage of electrical current but are also stress concentrators. Because of the principles of RSW, a good weld can only be achieved as long as the contact interface possesses a relatively high contact resistance. Lastly, ultrasonic welding showed intermediate UTS and the highest CR due to the connection of only small spots at the interface.

To measure the heat input and compare the process temperatures obtained through each technique, infra-red cameras were used (see Figure 3.3), in which the maximum temperature achieved during welding was determined as the output. Studies have found that laser beam, resistance, and ultrasonic welding reach, respectively, boiling temperature, melting temperature, and 30-60% of

melting temperature. However, the welding hot spot lies beneath the external conductor, therefore not visible to the camera. Nevertheless, the temperature at the cell terminal, where the weld is produced, is not of great concern since it does not contact the electrochemically active materials. Previous studies have shown that these materials start to decompose at 80ºC [19]. Therefore, the temperature at the cylinder barrel must be controlled.

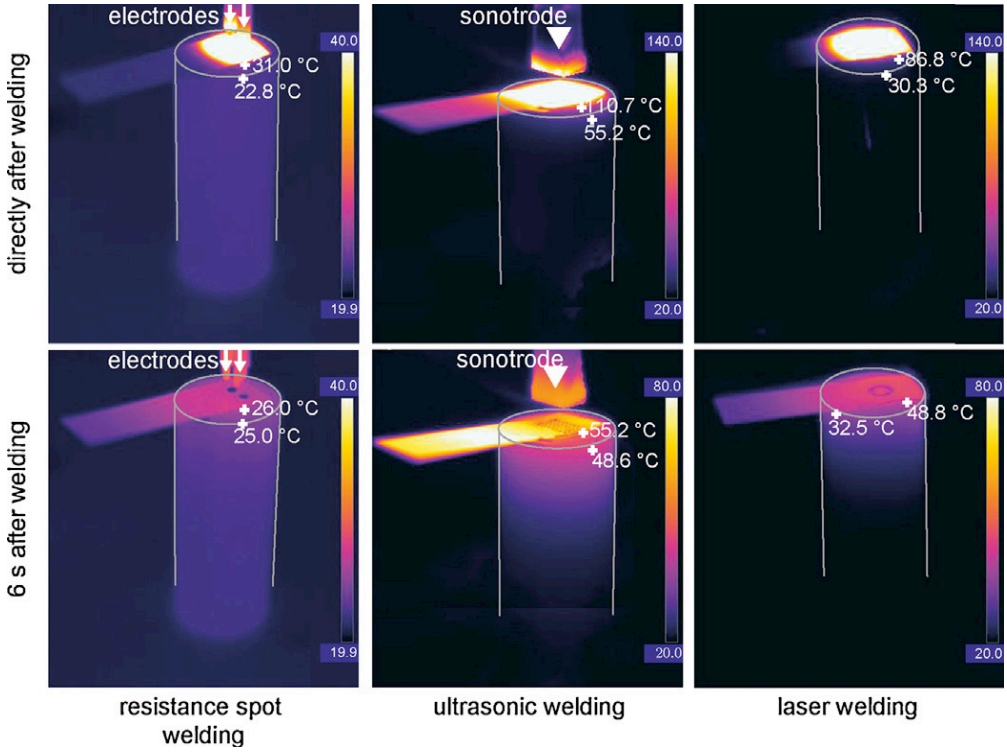

Figure 3.3 – Thermographic images of connected litihum-ion cells; highest temperatures at cell terminal and cylinder barrel marked. [18]

3.2 Electrical Resistance on Metal Contacts

Contact resistance is the resistance to the passage of electrical current between contacts. Since the electrical resistance is composed of bulk resistance and contact resistance, it is realized that contact resistance is an essential factor in heat generation [20]. The contact resistance is composed of two parts, constriction resistance, and film resistance, as seen in Figure 3.4. It has been found that constriction resistance occurs due to a single point of contact or to a number of points. Film resistance measures the resistance of thin films with nominally uniform thickness. Since the latter is invariable under the scaling of the

film contact, it can be used to compare the electrical properties of devices different in size.

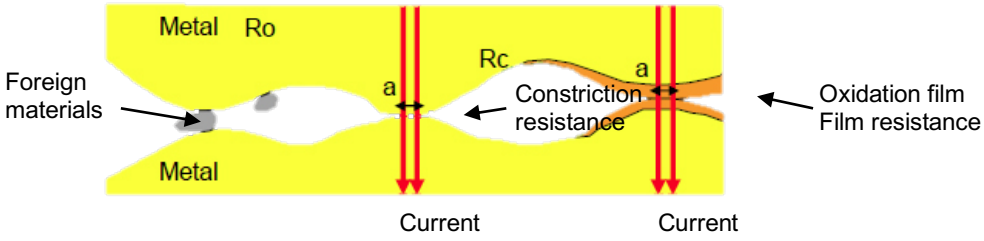

Figure 3.4 – Representation of constriction and film resistance in metal contacts. [21]

In welding, understanding the surface conditions, distribution of contacting asperities, material conductivities, and microscopic features is important to analyze contact resistance. When vacuum or air, for example, fills the void between the actual contact areas, most electrons flow through the metal-to-metal contact since it is the path of smaller electrical resistance [22].

Therefore, it is convenient for various welding applications to discover the effect of main parameters like pressure, temperature, and surface conditions on the contact resistance. Two methodologies have been used in the literature to investigate such effect, which can be called the static and dynamic.

The static contact resistance can be defined as initial interfacial resistance, which exists at room temperature before initiation of current flow. Through static contact resistance, it is possible to analyze if current passes through the contact. This is critical in battery applications, for example, in which welded electrodes must guarantee the passage of current. In the static method, the contact resistance across the interface is calculated under well-controlled situations, keeping parameters such as load and temperature stationary throughout the measurement. Dynamic resistance, in contrast, measures the contact resistance with progressing temperature. This is also of importance since the electrical resistivity of materials and electrodes are temperature-dependent [20].

3.3 Welding of Aluminum Alloys

Due to the vast areas of applications, welding of aluminum alloys has become an important research area. However, compared to other metals, aluminum welding presents many difficulties due to its intrinsic properties.

Regarding heat transfer, aluminum is an excellent heat conductor, so localized melting causes microstructure modifications even far from the weld due to high temperature. Also, since aluminum oxidizes very quickly, forming alumina, inclusions in the weld are often obtained. Gaseous inclusions can also be formed during welding due to high gas solubility in aluminum at high temperatures, for instance, hydrogen. The inclusions cause porosity to develop in response to the insufficient time for the gas to leave the metal's surface. Moreover, conventional techniques often lead to a significant deterioration of the weld's strength due to phase deformations and induced softening [23].

Perovic et al. [24] summarized that until the discovery of friction stir welding, strengthened aluminum alloys' weldability was a severe technological problem. Aluminum alloys of the series 2xxx and 7xxx are characterized by high strength, low toughness, and increased sensibility to cracking and were not weldable by fusion welding, as seen in Figure 3.5.

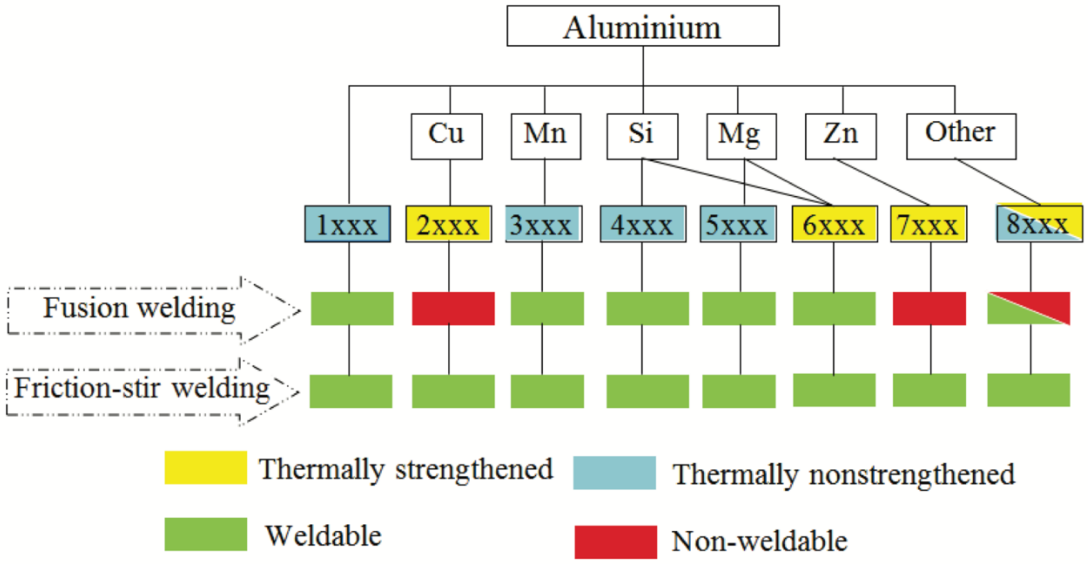

Figure 3.5 – Weldability of various aluminum alloys by fusion and friction stir welding [24].

This has led to the development and uprise in interest in solid-state joining processes, such as Friction Stir Welding (FSW), Friction Riveting (FR), and Refill Friction Stir Spot Welding. These solid-state welding techniques enable materials to be joined below their melting point, T_M, and cast structure modified because of grain refinement. Also, a fine dispersion of intermetallic compounds is possible,

and the formation of blowholes is avoided. Besides, studies have shown that FSW and refill FSSW can weld dissimilar joints with wrought alloys [11, 25, 26].

3.4 2xxx Series and AA2024 Alloy

Copper is the principal alloying element in the 2xxx series, with magnesium as a secondary element. Alloys in this series require solution heat treatment to attain optimum properties, often achieving higher mechanical properties than those presented by low-carbon steel. For further improvement in mechanical properties, these alloys can be subject to precipitation hardening. Although this treatment increases the strength of the alloy, it also causes a diminish in elongation. The alloys in the 2xxx series do not present such excellent corrosion resistance as other aluminum alloys, and under certain conditions, they may be subject to intergranular corrosion. Alloys in this series are usually used in applications where a high strength-to-weight ratio is required [27], such as in the aircraft and automotive industry.

One of the most used alloys in engineering is AA2024. It is used in applications requiring a high strength-to-weight ratio, as well as good fatigue resistance, therefore highly used in aircraft and automobile structures [28]. AA2024-T3 is a type of AA2024 aluminum tempered in T3. T3 temper is achieved by solution heat-treating the metal, strain hardening, and then naturally aging. Table 3.2 and Table 3.3 show the values of some of the AA2024-T3 aluminum alloy properties and its chemical composition, respectively.

Table 3.2 – Table of properties of the AA20204-T3 aluminum alloy.[29]

Property	**Density (g/cm^3)**	**Brinell H. (HB)**	**Elastic M. (GPa)**	**Fatigue S. (MPa)**	**Shear S. (MPa)**	**Shear M. (GPa)**	**UTS (MPa)**	**YS (MPa)**
Value	3.0	120	71	140	290	27	480	320

Table 3.3 – Nominal chemical composition of the AA2024-T3 aluminum alloy.[29]

Compos.	**Al**	**Cu**	**Mg**	**Mn**	**Si**	**Fe**	**Zn**	**Zr**	**Ti**	**Cr**	**Resid.**
(%)	90.7 to 94.7	3.8 to 4.9	1.2 to 1.8	0.3 to 0.9	0.5 max	0.5 max	0.25 max	0.2 max	0.15 max	0.1 max	0.15 max

3.5 Refill Friction Stir Spot Welding

3.5.1 Process Stages and State-of-the-Art

Refill Friction Stir Spot Welding is a solid-state joining process that produces an overlap connection between two or more sheets without melting the material, thus overcoming many of the existing challenges related to welding high strength aluminum alloys. The friction spot welding process is performed using a three-piece tool system consisting of a clamping ring, adjustable shoulder, and probe. While the clamping ring is fixed to the equipment, both the adjustable shoulder and the probe are contained in separate actuation systems, allowing them to move independently of each other.

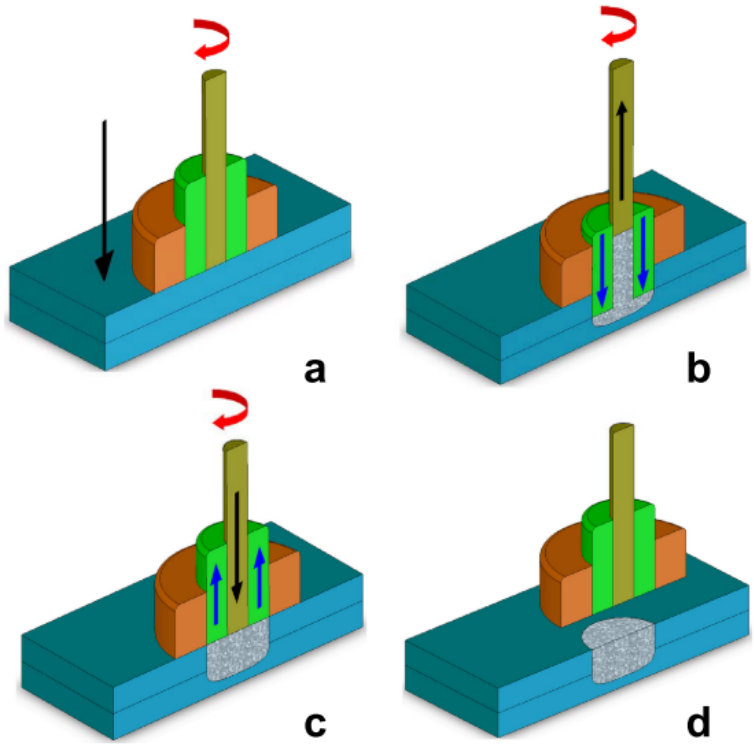

Figure 3.6 – Schematic representation of refill FSSW (adjustable shoulder-plunge variant) in four steps – (a) adjustable shoulder and probe rotation, (b) adjustable shoulder penetration and probe retraction, (c) adjustable shoulder and probe return to initial position, and (d) tool retraction [30].

The refill FSSW process, shown in Figure 3.6, has two variants – probe- and adjustable shoulder-plunge – and can be divided into four stages. Initially, the sheets are secured between a backing plate and the refill FSSW clamping ring. The probe and adjustable shoulder then begin to rotate, producing enough

frictional heat on the sheet's surface to plasticize it. The probe or the adjustable shoulder penetrates the material in the second stage, depending on the process variant. Figure 3.6 demonstrates the adjustable shoulder-plunge variant, in which the adjustable shoulder punctures the material to a predetermined depth while the probe retracts – the opposite occurs for the probe-plunge variant. After reaching the predetermined depth, the third stage initiates, and the adjustable shoulder begins to withdraw while the probe pushes the plasticized material that had initially been displaced. The probe and adjustable shoulder then return to the sheets' surface level, as in the initial position, and the entire tool retracts from the welded material. If a better mixing of material is required, a dwell time of both the probe and adjustable shoulder can be added [31, 32]. During this time, both components are rotating at a specific depth for a predetermined time.

Studies that investigated the optimization of refill FSSW for best mechanical properties used two to three process variables [32–35] to avoid too much complexity during statistical analysis. Thus, the parameters most studied consist of:

- rotational speed – the speed at which the tool components rotate;
- plunge depth - the maximum depth the tool will penetrate into the material;
- plunge speed - the velocity required for the tool to achieve the plunge depth; and
- dwell time - the time that the tool will rotate at the desired depth.

Preliminary studies investigate which parameters were most influential in microstructural features and mechanical properties of welds for a given material configuration. Rosendo et al. [9] studied the influence of welding time and rotational speed when welding AA6181-T4 by refill FSSW and concluded that welding time had greater control over the heat input required to promote good bonding between the plates. Junjun et al. [36], however, concluded that the depth of penetration plays a significant role in the mechanical properties of AA5083 copper welds.

Other studies that analyzed welds performed on dissimilar materials faced problems such as the formation of intermetallic compounds (IMCs) that

weakened the bonding interface between the sheets. Plaine et al. [32] welded AA5754 to Ti6Al4V and found that dwell time was one of the most influential parameters on joint mechanical properties. Short dwell time did not allow a proper mix between dissimilar materials as it did not provide sufficient time for the formation of a reaction layer. However, if dwell time were too long, many IMCs were formed, compromising the weld's mechanical strength. Thus, each configuration of welded materials (similar, dissimilar, thickness, oxidative layer) has characteristics that was affected differently by each parameter.

3.5.2 Microstructure in refill FSSW

Due to this process's nature, the heat generated by friction and the strain rates imposed on the material produce different metallurgical zones in the welded region. Figure 3.7 is a representation of a typical refill FSSW cross-section.

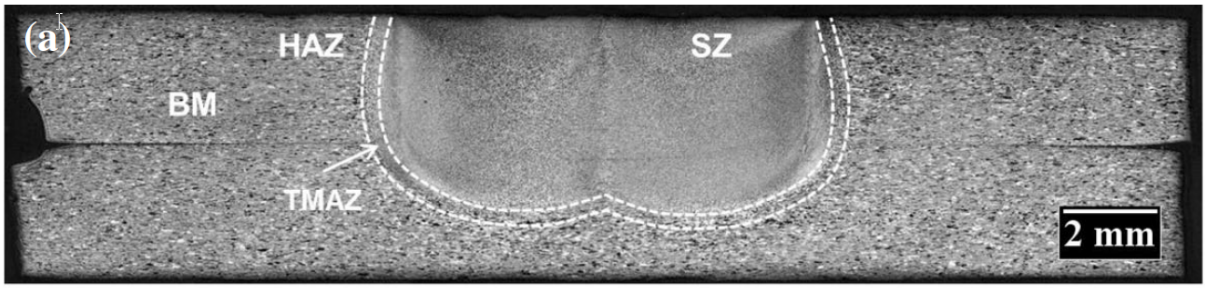

Figure 3.7 – Cross-section and metallurgical zones of a typical refill FSSW weld. [34]

Four different metallurgical zones can be observed: Base Material (BM), Heat Affected Zone (HAZ), Thermo-mechanically Affected Zone (TMAZ), and Stir Zone (SZ). BM is the region of the weld that was not affected by heat or process deformation rates. The grain and mechanical properties of this zone are identical to the material before welding. The HAZ corresponds to the region that is affected by the rise in temperature. This zone has not undergone plastic deformation caused by tool rotation and penetration, only subjected to thermal cycling by temperature rise. Therefore, annealing phenomena, such as recovery, and hardening mechanisms, such as over aging and reprecipitation, can occur in the HAZ. The material present in the TMAZ is close enough to the tool to be subjected to deformation rates and moderate temperatures. These conditions provide partial grain refinement, grain, and sub-grain formation due to the phenomenon of dynamic recovery and recrystallization and grain realignment in the plunge

direction. In the SZ, temperature and strain rates are at their highest, forcing the grains to recrystallize. Therefore, this region is characterized by a refined microstructure. Thus, in welds made on only two plates, the location of these zones is always the same: SZ is located in the center of the cross-section, and it is surrounded by TMAZ, HAZ, and BM, respectively.

Although the metallurgical zones described earlier are typical in all refill FSSW studies, the material flow and behavior during the welding is still not fully understood. Shen et al. [37] conducted a study to investigate the texture development and material flow behavior during refill FSSW of AlMgSc and used EBSD analysis to detail the metallurgical zones' transition areas – results shown in Figure 3.8. It was found that apart from region b, located in the TMAZ, all the other regions have recrystallized grain features. However, the center of the SZ is partially recrystallized due to the relatively low local shear strain. It was also concluded that the defined SZ has a concave bottom, unlike what is estimated in the literature from optical microscopy. Therefore, more studies need to be conducted to comprehend the formation of metallurgical zones further.

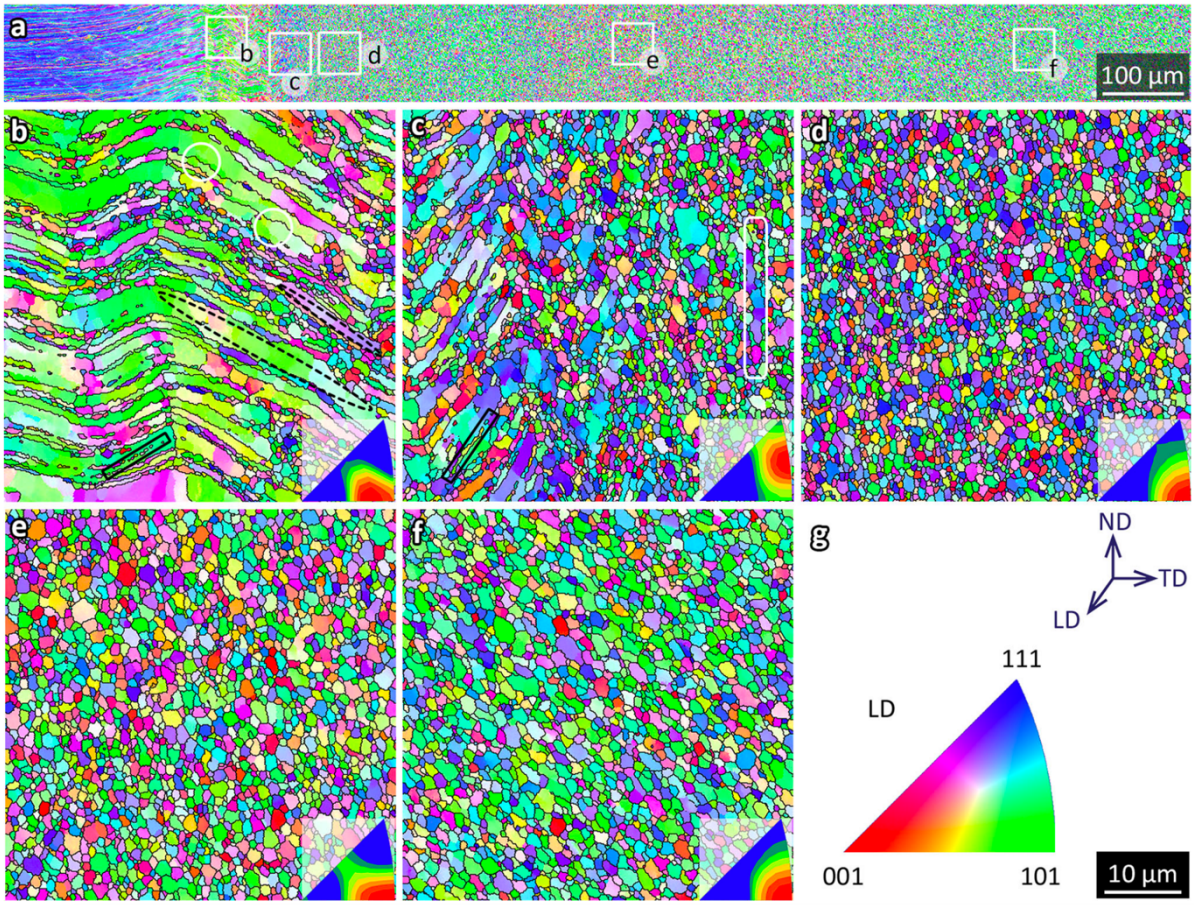

Figure 3.8 – Details of the transition area: (a) a composite EBSD map superimposed with white boxes b through f showing the locations of regions with different contrasts, (b) through (f) EBSD maps of each region with inserts showing the corresponding inverse pole figures, (g) the reference frame and a triangle showing the color code (an individual pixel is colored according to its crystallographic direction relative to the LD) for EBSD maps, and the scale bar for b through f [37].

Refill FSSW welds have great potential to replace current spot-welding techniques. Therefore, this technique is viable for structural component applications and has significant benefits in replacing mechanical fixation or fusion welding [8, 38]. Friction spot welding offers several advantages over conventional welding techniques, such as high energy efficiency, high welding speeds, high-quality post weld surface, and high environmental compatibility. Previous studies have shown that this technique also has mechanical properties above standard requirements when welding similar and dissimlar materials such as aluminum, steel, titanium, magnesium, and copper [11, 26, 31, 39–43].

However, as mentioned earlier, good mechanical properties are not sufficient characteristics for battery applications. Due to electrochemically active materials, the heat generated during the joining process is a significant concern.

High temperatures in the external conductor do not harm a battery cell, but temperatures within the enclosure, which is in direct contact with these electrochemical materials, influence their properties.

In short, refill FSSW has many advantages over conventional welding processes, such as mass reduction and, in some cases, better mechanical properties. However, there are no studies found in the literature investigating the use of this process in multilayer materials. Aiming for welds with features comparable to or better than those from today's techniques, the use of refill FSSW in lithium-ion batteries is a step forward in reducing weight and improving EV efficiency.

3.6 Response Surface Methodology

Response surface methodology (RSM) is a collection of mathematical and statistical techniques useful for modeling and analyzing problems in which several variables influence the response of interest, and the objective is to optimize the response. In general, such a relationship is unknown but can be approximated by a low-degree polynomial model of the form

$$y = f'(x)\beta + \epsilon \tag{3.1}$$

where x = (x_1, x_2,…, x_k), $f'(x)$ is a vector function, β is a vector, and ϵ is a random experimental error [44].

Response Surface Methodology has been commonly used in the optimization of refill FSSW studies [32–35]. Although several processing parameters are varied (such as Rotational Speed, Plunge Speed, Dwell Time, Plunge Depth, etc.), refill FSSW optimization studies were usually limited to two or three parameters to avoid too much complexity during analysis. Plaine et al. [32] conducted a study in which rotational speed (RS) and dwell time (DT) were varied to optimize the mechanical behavior of AA6181-T4 and Ti6Al4V dissimilar welds produced by FSSW. A response surface plot of Lap Shear Strength (LSS) in the function of RS and DT is presented in Figure 3.9.

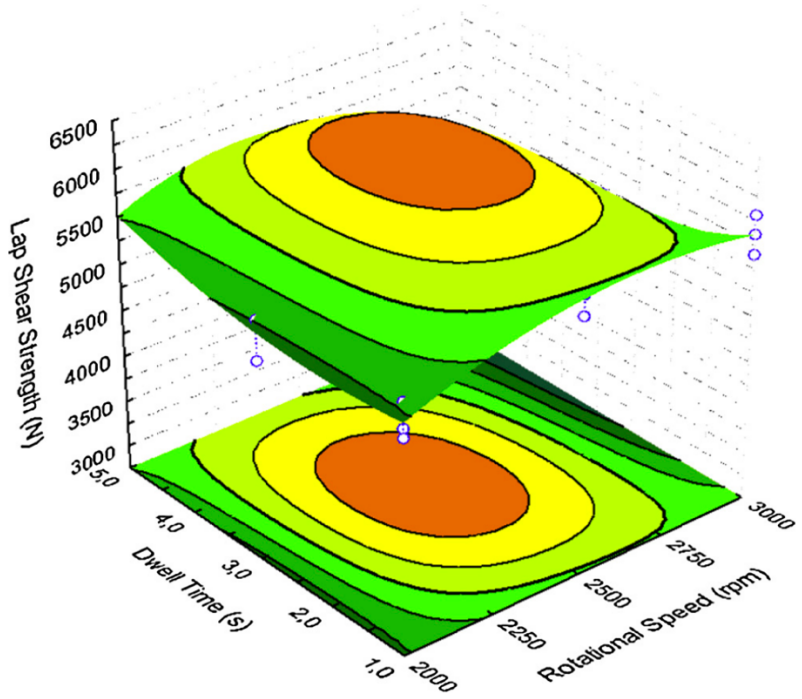

Figure 3.9 – Response Surface Plot for Lap Shear Strength (LSS) as a function of Rotational Speed (RS) and Dwell Time (DT) [32].

The proper choice of design is essential in any response surface methodology. Orthogonality and Rotatability are properties commonly desired in RSM. A design is orthogonal if each factor can be evaluated independently of all the other factors. This makes it easier to test the significance of the unknown parameters in the model. A design is said to be rotatable if the prediction variance is constant at all points equidistant from the design center. This makes it easier to compare the predicted response values on a given hypersphere, as all such values have the same variance. In studies that choose to analyze three parameters' influence on a given response, second-order designs are utilized. The most frequently used second-order designs are the 3k factorial, central composite, and the Box-Behnken Designs.

In the case of refill FSSW studies, a particular method, called Taguchi, is also occasionally used. The Taguchi method is a robust parameter design sought to make the product's quality insensitive to the uncontrollable process variations. To achieve this goal, Taguchi advocated using crossed arrays by crossing an orthogonal array of control variables with an orthogonal array of noise variables.

Despite generating significant contributions to the improvement of product quality, the Taguchi method has received some criticisms, such as:

1. Not estimating the interactions among the control factors;
2. requires many experimental runs; and
3. signal-to-noise ratios cannot be distinguished between inputs affecting process mean and those affecting the variance.

3.6.1 Box-Behnken Design

Second-order composite designs usually require five levels coded for each of the variables. However, circumstances occur where second-order arrangements are needed, which, for ease of performance, must employ the smallest number of different levels, namely three. One useful class of such designs, economical in the number of runs required, is due to Box and Behnken. The designs are formed by combining two-level factorial designs with incomplete block designs [45].

Box-Behnken Designs (BBD) are also advantageous for dispensing the need for experimental runs at boundaries and extreme treatment combinations. Therefore, in a cube where each axis depicts the parameter range, all corners and star points are not required for testing for experimental analysis. Conversely, BBDs are not indicated for studies in which the responses at the extremes are necessary. The geometry of this design suggests a sphere within a cube with processing parameters. The experimental points are depicted by the tangents of the sphere with the cube, that is, the edge midpoints, as seen in Figure 3.10.

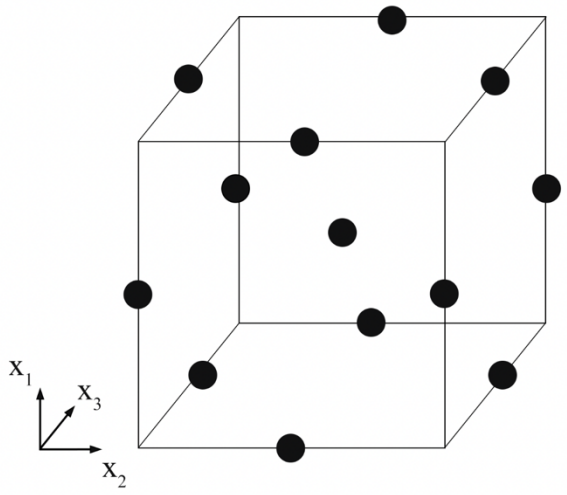

Figure 3.10 – A Box-Behnken experimental cube for three factors, 3^3. Credit to the author.

The number of experiments (N) required for the development of BBD is defined as $N = 2k(k-1) + C_0$, where k is the number of factors, and C_0 is the number of center points. For comparison, the number of experiments for a central composite design is $N = 2^k + 2k + C_0$ [46, 47]. With three factors, BBD will have thirteen points located in the center of the cube's lattices. Therefore, it will include zero for one of the elements and then a plus or minus combination for the other two factors and three center points, as seen in Table 3.4.

Table 3.4 – Coded factor levels for a Box-Behnken Design of a three-variable system.

Box Behnken Design			
Factors	3	**Replicates**	1
Base runs	15	**Total runs**	15
Base blocks	1	**Total blocks**	1
Center points	3		

Run	Block	A	B	C
1	1	-	-	0
2	1	+	-	0
3	1	-	+	0
4	1	+	+	0
5	1	-	0	-
6	1	+	0	-
7	1	-	0	+

8	1	+	0	+
9	1	0	-	-
10	1	0	+	-
11	1	0	-	+
12	1	0	+	+
13	1	0	0	0
14	1	0	0	0
15	1	0	0	0

Another advantage of BBD is its rotatability. As mentioned earlier, a second-order model needs to provide useful predictions throughout the region of interest. That is, the model should have a reasonably consistent and stable variance of the predicted response at the points of interest. In BBD, the variance is the same at all points that are at the same distance from the design center.[48]

A comparison between the BBD and other response surface designs (central composite and three-level full factorial) demonstrated that the BBD is slightly more efficient than Central Composite Design (CCD). Moreover, BBD is much more efficient than a three-level full factorial where the efficiency of one experimental design is defined as the number of coefficients in the estimated model divided by the number of experiments [47].

3.7 Analysis of Variance

Analysis of Variance (ANOVA) is a statistical technique for analyzing measurements depending on several effects operating simultaneously to decide which effects are significant and estimate the effects. The ANOVA method assesses the relative size of variance among group means (between-group variance) compared to the average variance within groups (within-group variances). This analysis becomes useful in situations where the analyst wishes to investigate if different treatments in a given experiment, that is, when the analyst varies a factor in two or more levels, produce different means or if the difference between the means is due to variance within groups.

For the simplest case, suppose there are ***a*** different levels of a single factor that the analyst wishes to compare. The observed response from each level is a random variable. The data would appear as in Table 3.5.

Table 3.5 – Typical data for a single-factor experiment.

Level	Observations				Totals	Averages
1	y_{11}	y_{12}	…	y_{1n}	$y_{1.}$	$\bar{Y}_{1.}$
2	y_{21}	y_{22}	…	y_{2n}	$y_{2.}$	$\bar{Y}_{2.}$
…	…	…	…		…	…
a	y_{a1}	y_{a2}	…	y_{an}	$y_{a.}/y_{..}$	$\bar{Y}_{a.}/\bar{Y}_{..}$

It is useful to describe the observations from an experiment with a model, as shown in Eq. 3.2.

$$y_{ij} = \mu_i + \tau_i + e_{ij} \begin{cases} i = 1, 2, \dots, a \\ j = 1, 2, \dots, n \end{cases} \tag{3.2}$$

where *yij* is the *ij*th observation, μ_i is the mean of the *i*th factor level, τ_i is a parameter unique to the *i*th treatment, and e_{ij} is a random error component that incorporates all other sources of variability in the experiment, including measurement, variability arising from uncontrolled factors, and general background noise in the process. By assuming the variance to be constant for all levels of the factor, the treatment equality hypothesis is tested so that the treatment effects are zero.

The total variability in the data, as measured by the total corrected sum of squares, Eq. 3.3, can be partitioned into a sum of squares of the differences between the treatment averages and the grand average plus a sum of squares of the differences of observations within treatments from the treatment average. Now, the difference between the observed treatment averages and the grand average is a measure of the differences between treatment means, whereas the differences of observations within a treatment from the treatment average can be due to only random error.

$$SS_T = SS_{Treatments} + SS_E \tag{3.3}$$

where $SS_{Treatments}$ is called the sum of squares due to treatments, and SS_E is called the sum of squares due to error. There are $an = N$ total observations; thus, SS_T has $N - 1$ degrees of freedom. There are a levels of a factor, so $SS_{Treatments}$ has $a - 1$ degrees of freedom. Finally, there are n replicates within any treatment providing $n - 1$ degrees of freedom with which to estimate the experimental error. Because there are a treatments, there are $a(n - 1) = N - a$ degrees of freedom for error. By dividing the sum of squares by the degrees of freedom, sample

variances are combined to give a single estimate of the common population variance, referred to as mean squares (MS).

Because the degrees of freedom for $SS_{Treatments}$ and SS_E add to $N - 1$, the total number of degrees of freedom, Cochran's theorem [49] implies that $SS_{Treatments}/\sigma^2$ and SS_E/σ^2 are independently distributed chi-square random variables. Therefore, if the null hypothesis of no difference in treatment means is true, then Eq. 3.4 applies. In that case, the null hypothesis H_0 is rejected, and it can be concluded that there are differences in the treatment means if $F_0 > F_{\alpha, a-1, N-a}$. The test procedure is summarized in Table 3.6.

$$F_0 = \frac{\frac{SS_{Treatments}}{a-1}}{\frac{SS_E}{N-1}} = \frac{MS_{Treatments}}{MS_E} \tag{3.4}$$

An analysis of variance can be used in many other statistical experiments. It is widely used, for example, in a 2^k design, that is, a design with k factors each at two levels. In this case, the analysis of variance is used to formally test for the significance of the main effects and interaction between the factors.

Table 3.6 – The analysis of variance table for a single-factor.

Source of Variation	Sum of Squares	Degrees of Freedom	Mean Square	F_0
Between treatments	$SS_{Treatments}$	$a - 1$	$MS_{Treatments}$	$MS_{treatments}/MS_E$
Error (within treatments)	$SS_E = SS_T - SS_{Treatments}$	$N - a$	MS_E	
Total	SS_T	$N - 1$		

4 MATERIALS AND METHODS

4.1 Materials

Rolled AA2024-T3 aluminum with a nominal thickness of 0.3 mm was used to simulate the welding tab and to provide the weld configuration with mechanical resistance during the welding process, that is, to avoid material twisting. The T3 heat treatment consisted of a solution heat treating, followed by cold working and natural aging to a substantially stable condition. The main alloying elements present in the alloy are copper and magnesium, which allow the mechanical properties to improve upon solution treating and precipitation hardening. Commercially pure aluminum (CP-Al) foil with a nominal thickness of 13 μm was also used. The specimens were cut from larger sheets to attain a 25.4 mm width and a 100 mm length. The nominal chemical compositions of both alloys used in this work are presented in Table 4.1. Figure 4.1 depicts the base material microstructure in three dimensions, indicating the transversal and longitudinal directions used for reference.

Table 4.1 – Nominal chemical composition of the materials used in this work [27].

Alloy	Al (%wt.)	Cu (%wt.)	Mg (%wt.)	Mn (%wt.)	Fe (%wt.)	Si (%wt.)
AA2024-T3	90.7 - 94.7	3.8 – 4.9	1.2 – 1.8	0.3 – 0.9	<0.5	<0.5
CP - Al	> 99.00	0.05 – 0.20	-	< 0.05	<0.95	<0.95

Figure 4.1 – 3D microstructure of the AA2024 base material. Credit to the author.

SEM images of the base materials of AA2024-T3 and commercially pure aluminum are depicted in Figure 4.2. EDS analysis showed that the AA2024-T3 (Figure 4.2a) microstructure is composed of an Al-matrix with Al_2Cu (θ) and Al_2CuMg (S-phase) particles with an average size of 1-2 μm. Boag et al. [50] investigated the microstructure of AA2024-T3 and found several phases in which Mg, Al, and Cu were the main constituents (40% of all particles), although particles with Mn, Fe, Si were also found. The commercially pure Al (Figure 4.2b) microstructure presents an Al-matrix with α-AlFeSi particles of 1-2 μm.

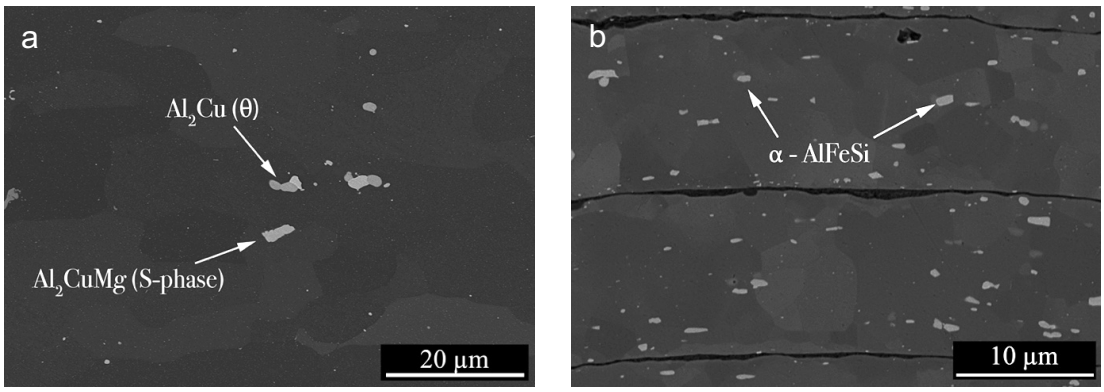

Figure 4.2 – SEM images of the base material of the (a) AA2024 sheet and (b) commercially pure Al foil.

4.2 Production of Welds

All friction spot welds were conducted using a Harms&Wende RPS100® welding machine. The welds were performed with the adjustable shoulder plunge variant with a fixed welding force of 14.8 kN without cooling air. A Uddeholm Hotvar hot-work-steel tool was used since it is suitable in applications of hot-wear and plastic deformation. The tool consisted of a clamping ring, adjustable shoulder, and probe of 17 mm, 9 mm, and 6 mm diameters, respectively. The RPS100® software interface allows the user to set rotational speed (RS), plunge depth (PD), plunge speed (PS), dwell time (DT), and clamping pressure values.

Welds were performed using two configurations, in which 50 foils of CP-Al were positioned between two AA2024-T3 sheets. For metallographic preparation and process temperature, the aluminum sheets were welded between two completely overlapping plates. For lap shear testing, the AA2024-T3 plates overlap by only 1 square inch, as shown in Figure 4.3.

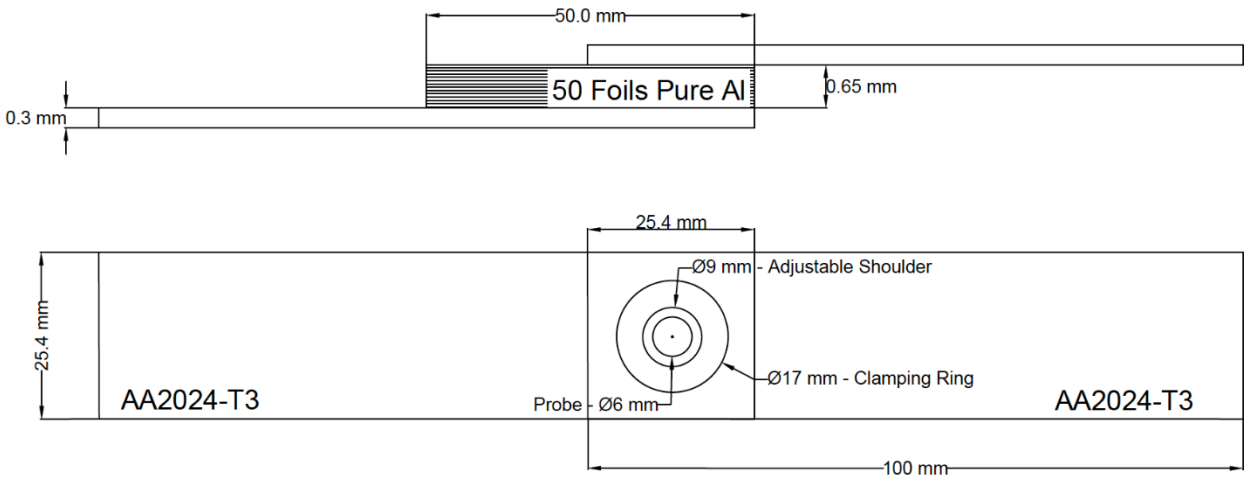

Figure 4.3 – Sheet and foil configuration for lap shear testing. Credit to the author.

4.3 Chemical Analysis and Phase Transformation Characterization

X-ray Dispersive Spectroscopy (EDS) analysis was performed to characterize the elements present in commercial aluminum, in the equilibrium phases formed after welding, and to map the diffusion of elements along with the interfaces.

Thus, using such technique, it was possible to investigate which phases were formed after the material was subjected to high temperatures with severe strain rates, and to locate the regions in which these transformations occur.

4.4 Mechanical Property Determination and Fracture Analysis

Lap shear testing was conducted to assess the global mechanical properties of the weld. The equipment used was a screw-driven Zwick/Roell® testing machine with a load capacity of 200 kN at 25 ºC with a displacement rate of 2 mm/s. Three samples were tested for every welding condition in order to obtain a mean lap shear resistance with a reliable standard deviation. Moreover, due to the AA2024 alloy being susceptible to natural aging, all tests were conducted within 24 hours after welding. To compensate for the different plate heights, when welded in the overlap configuration, Figure 4.3, a displacement between the clamping jaws was required. The sample's fixation area was 25.4 mm x 25.4 mm.

Since the weld presents metallurgical zones that have suffered different deformation levels and temperatures (ZTA and ZTMA, for example), it was of interest to map the location of these regions by hardness tests. This mapping was performed through micro-indentations following ASTM E384-17 [25].

Finally, the fracture surface was analyzed by optical microscopy and a photographic analysis to characterize the fracture mode and investigate the crack's propagation path.

4.5 Process Temperature Analysis

An InfraTec ImageIR® 8300 infrared camera with the aid of IRBIS3 Professional® software was used to analyze the temperature distribution throughout the sheet during and after welding. Dupli-Color Lackspray Tuning Supertherm Black, a high-temperature resistance spray, was used to paint the entire sheet and eliminate the influence of the sheet's reflectivity on the temperature measurement of the camera. Measurements of three samples for every welding condition were taken to obtain an average temperature of the sheets' surface.

Thermal measurements were performed with thermocouples located inside the plates during the welding process to identify the regions that suffer the highest or lowest temperature increases. These measurements were analyzed to investigate the transformation temperatures of the present phases and corroborate the EDS data to understand the weld's microstructural characteristics.

4.6 Contact Resistance Analysis

The contact resistance of the welds was analyzed to assess the quality of the weld regarding conductivity while varying process parameters. However, since a standard for measuring contact resistance for a spot like joints does not exist, an arbitrary configuration was adopted to measure the resistance of a current when passing from the upper to the lower sheet, therefore through the weld.

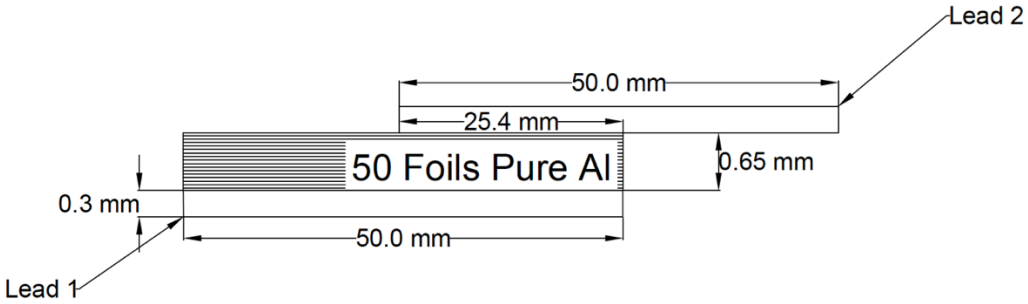

Figure 4.4 – Weld configuration for contact resistance measurements. Credit to the author.

As shown in Figure 4.4, welds were produced in the center of sheets with 50 mm length and 25.4 mm width. The current resistance was then measured by clamping one resistance lead on the edge of the upper sheet and the other resistance lead the lower sheet's edge. This configuration would, consequently, allow the current to pass through the weld. Three measures were taken for every sample, and the average was used for statistical analysis.

4.7 Metallographic Characterization

For metallographic preparation, the welds were cut using a Struers Secotom-50 with a 10S20 cut-off wheel at 2000 rpm and linear displacement of 0.200 mm/s near the weld's centerline, allowing a margin of material to be ground without losing the center of the weld. Later, the welds were embedded with Demotec-20® resin in polyethylene mounting cups with a pressure of 2 bar for twenty minutes. Lastly, the embedded sample was polished using a Struers Tegramin® equipment.

The cross-section was then analyzed with the use of a Leica SM IRM® optical microscope and a FEI Quanta 650 scanning electron microscope fitted with an EDAX energy dispersive X-ray spectrometer (EDS) detector.

4.8 Stop Action Procedure

Stop Action is a procedure that consists of manually stopping the welding process while the tool components are plunging or retracting from the material, followed by quenching the sample. This experiment allows the investigation of material behavior during each step of the process.

In this work, the welding machine was stopped when the adjustable shoulder achieved 0.3 mm, 0.5 mm, and 0.7 mm depths during plunging and then 0.5 and 0.3 during retracting.

5 RESULTS AND DISCUSSIONS

5.1 Process Optimization

5.1.1 Screening

Before parameter optimization could be carried out, it was necessary to define a process window in which no superficial nor internal volumetric defects would appear, allowing the optimization process to consider only metallurgical aspects of the weld. Therefore, a screening process was carried out, in which commonly studied process parameters (RS, PD, PS, and WF) were varied to assess the resulting microstructure and superficial quality of the weld.

Table 5.1 – Initial range of parameters for screening of resulting microstructure and superficial quality.

Parameter	Min	Max
Rotational Speed (rpm)	1000	2000
Plunge Speed (mm/s)	0.6	2.2
Plunge Depth (mm)	0.2	0.8
Welding Force (kN)	6.0	8.0

The initial range of parameters used for screening is presented in Table 5.1, in which the parameters were varied using the One-Factor-At-A-Time method. Regarding rotational speed, a minimum of 1000 rpm and a maximum of 2000 rpm was established. Lower than 1000 rpm would not produce enough heat input for a stable joint, and a rotational speed above 2000 rpm might produce heat inputs too high, which, as mentioned in section 3.1, is a concern due to the electrochemically active material inside the lithium-ion-battery. Plunge depths below 0.2 mm did not penetrate the material enough to produce joining between sheets and depths greater than 0.8 mm would lead to the lower sheet bonding to the backing. Plunge speed limits were set between 0.6 mm/s and 2.2 mm/s according to the machine’s limit when plunging 0.2 mm depths. Dwell time was kept at 0 s and not investigated in this study because a better material mixing was initially found to be unnecessary given the weld's microstructure with good

material mixing, and because a faster weld is convenient for the application. Welding force was chosen arbitrarily.

Table 5.2 demonstrates a representative assessment of specific combinations of parameters. A table with more welding conditions and observations is presented in Appendix A. It was found that higher rotational speeds and plunge speeds provided welds with good surface quality and that the lower sheet bonding to the backing and twisted material were related to plunging depth and welding force, respectively. Figure 5.1 depicts welds that bonded to the backing and that presented twisted materials.

Table 5.2 – Representative assessment of parameter combination for screening procedure.

Weld No.	RS (rpm)	PD (mm)	PS (mm/s)	WF (kN)	Note
1	1500	0.8	0.8	6.2	Good Surface, Lower sheet bonded to the backing
2	1500	0.7	0.8	6.2	Bad surface, no bonding to the backing
3	1750	0.8	1.6	6.2	Good Surface, Lower sheet bonded to the backing
4	1500	0.5	0.6	6.2	Bad surface, no bonding to the backing, materials twisted

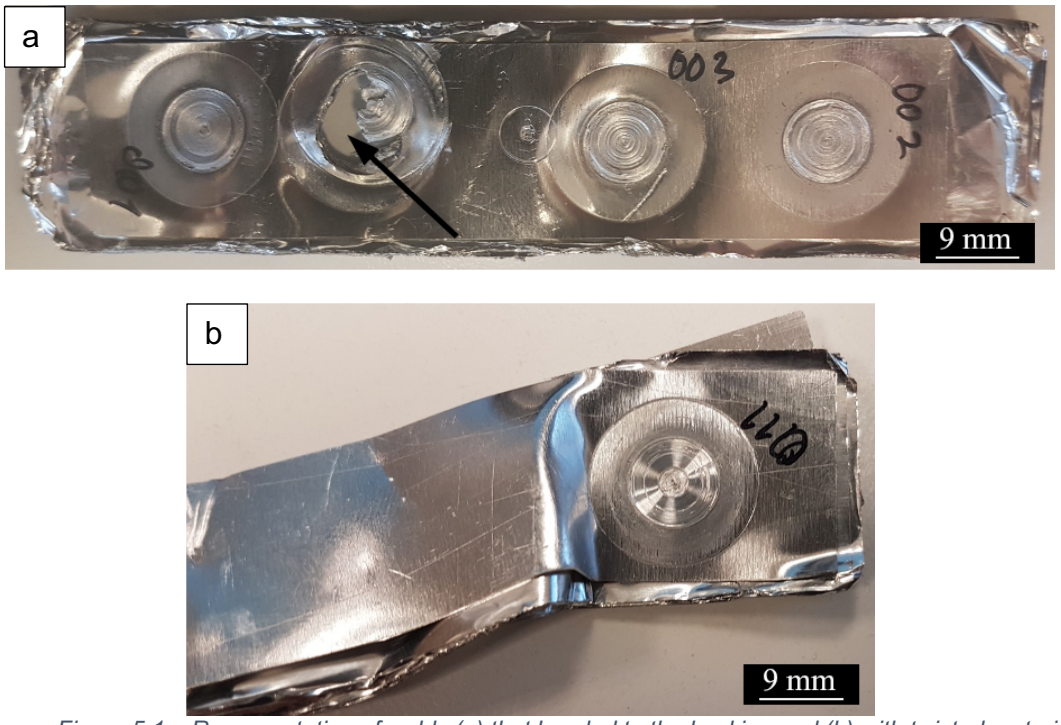

Figure 5.1 – Representation of welds (a) that bonded to the backing and (b) with twisted materials.

To avoid high complexity of the analysis, only three parameters were chosen to study process optimization. Moreover, the screening procedure demonstrated that the three most influential parameters, regarding surface quality, are plunge depth, rotational speed, and plunge speed.

Twisting of the sheets was avoided by increasing the welding force to 7.2 kN, later kept constant at this value throughout the study. While varying rotational speed inside the preliminary process window, it was observed that rotational speeds below 1400 rpm would produce welds with low superficial quality and that this quality would be improved by increasing the RS. Similar observations were made when varying plunge speed with values below 1.0 mm/s – surface quality improved with increasing PS. When varying plunge depth, it was not possible to identify a trend regarding the analyzed criteria. All depths within the determined range produced welds with good surface quality. However, setting plunge depths below 0.3 mm did not guarantee bonding of sheets, and plunge depths above 0.7 mm would cause the lower sheet to bond to the backing bar. These observations are summarized in Table 5.3.

Table 5.3 – Preliminary Process Window

Parameters	Minimum	Maximum	Note
Rotational Speed (rpm)	1400	2000	Surface Quality Increases with Increasing RS.
Plunge Speed (mm/s)	1.0	2.2	Surface Quality Increases with Increasing RS.
Plunge Depth (mm)	0.3	0.7	Below 0.3 mm the weld is easily detached; Above 0.7 mm the sheet attaches to the backing.

Figure 5.2 is representative of the weld's good surface quality. No superficial defects, such as lack of refill and detached material, nor twisting of the sheets and foils were found. Initially, only the weld's superficial quality was to be assessed, later following a microstructural analysis to observe the presence or absence of defects.

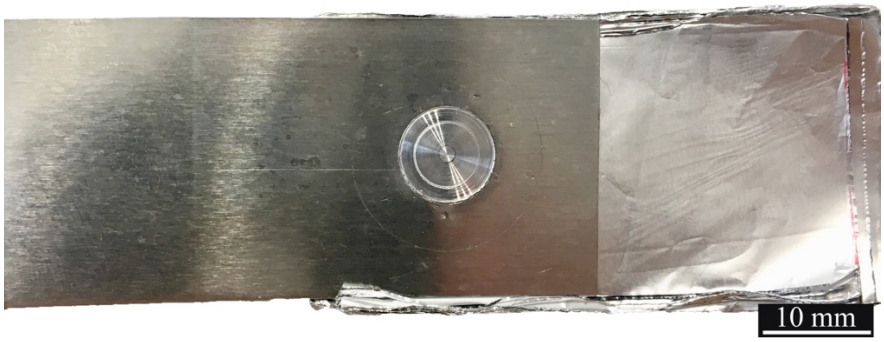

Figure 5.2 – Representation of a weld with good surface quality. Parameter combinations – (1700 rpm, 1.6 mm/s, 0.5 mm).

It was necessary to find a process window in which no metallurgical defects would appear to avoid their influence on process optimization. For this, many samples were produced varying one-factor-at-a-time and analyzed microscopically without etching. Each factor was varied in two levels, one on the upper and the other on the lower limit. This would examine each factor's full range and detect the presence of defects if there were any. Therefore, this study assumed that no defects would appear within the parameters' entire range if there are no defects in the factor intervals' extremities.

The first parameter that was analyzed was the rotational speed. Beforehand, this parameter was believed to be the most influential regarding heat input, as discussed in the work of Reimann et al. [25]. Moreover, it was believed that intermediate rounds per minute would allow for better material mixing, producing a better weld overall, as concluded by Amancio et al. [10] and Tier et al. [51].

Two samples were welded at 1400 rpm (Figure 5.3a) and 2000 rpm (Figure 5.3b). Both had fixed plunge speed and plunge depth values of 1.6 mm/s, and 0.5 mm, respectively. The values of the fixed parameters were mainly based on the center point of each parameter range inside the process window (Table 5.3) but were also varied to analyze more parameter combinations.

From Figure 5.3, it is possible to infer that high and low rotational speeds do not vary the weld’s macrostructure significantly. It was also observed that no defects were shown on the adjustable shoulder’s path, nor the bonding surfaces. Therefore, through the analysis of the unetched samples, it was concluded that

the rotational speed could be varied within a range of 1400 rpm to 2000 rpm while presenting good surface quality and no microstructural defects.

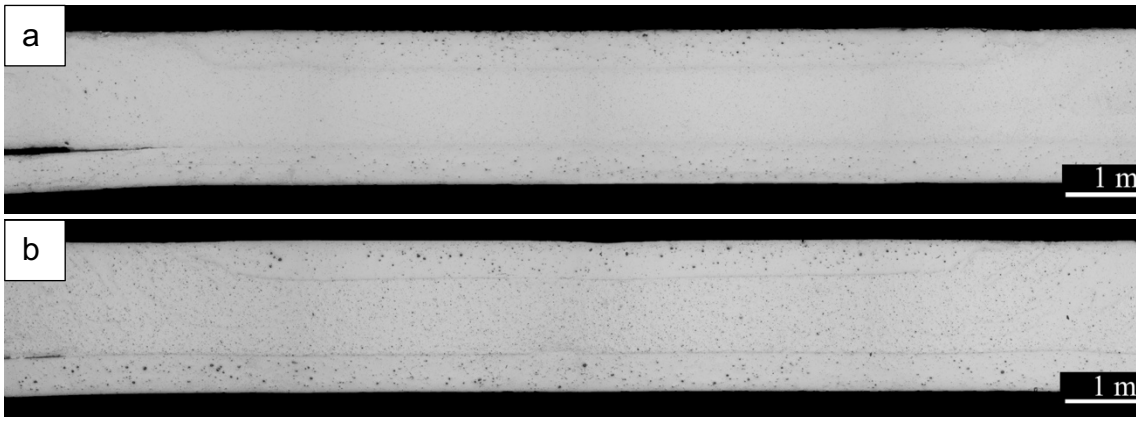

Figure 5.3 – Welds produced with fixed plunge speed and plunge depth while varying rotational speed to (a) 1400 rpm and (b) 2000 rpm.

Secondly, the plunge speed was varied and analyzed. It has been reported that low joining times (high plunge speeds) could lead to high strain rates on the material surrounding the refill FSSW tool, generating weld defects [10]. Macrographs of the welds produced with 1.0 mm/s and 2.2 mm/s plunge speed are depicted in Figure 5.4a and Figure 5.4b, respectively. Plunge depth and rotational speed were maintained at 0.5 mm and 2000 rpm, respectively. It was observed that the unetched samples did not show significant differences when varying PS in such interval. Moreover, no apparent defects, such as unbonded interfaces and voids, were found. Therefore, the proposed range for PS is appropriate for optimization analysis.

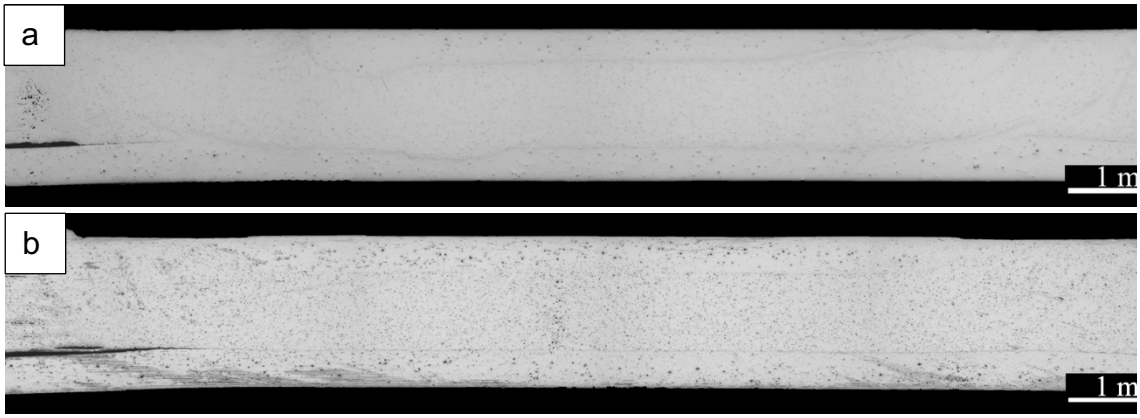

Figure 5.4 – Welds produced with fixed plunge depth and rotational speed while varying plunge speed to (a) 1.0 mm/s and (b) 2.2 mm/s.

Lastly, plunge depth was varied between 0.3 mm and 0.7 mm. Da Silva et al. [30] have reported that higher plunge depths increase the weld's overall lap

shear strength resistance, and Tier et al. [52] have concluded that plunge depth is the most critical process variable. Figure 5.5a-b depict macrographs of welds produced with plunge depths of 0.3 mm and 0.7 mm with rotational speed and plunge speed of 2000 rpm and 1.6 mm/s, respectively. It was observed that no defects were encountered inside this plunge depth interval and that no significant differences were found in the unetched samples. Therefore, approving such a range for further design of experiment analysis.

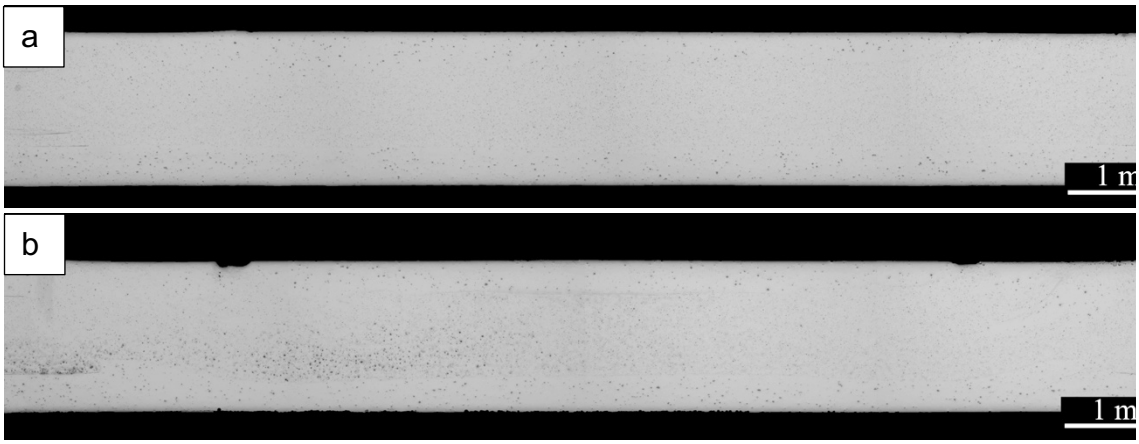

Figure 5.5 – Welds produced with fixed rotational speed and plunge speed, while varying plunge depth to (a) 0.3 mm and (b) 0.7 mm.

This study demonstrated that no defects were present when ranging the parameters at the full extent of the determined interval. Therefore, validating Table 5.4 as the process window for statistical analysis.

Table 5.4 – Process Window

Parameters	Minimum	Maximum
Rotational Speed (rpm)	1400	2000
Plunge Speed (mm/s)	1.0	2.2
Plunge Depth (mm)	0.3	0.7

5.1.2 Box-Behnken Design

As seen in section 3.6.1, the Box-Behnken model uses a design in which each variable is scaled such that it has a range of [-1, 0, +1], corresponding to the low, medium, and high levels, respectively. With the aid of Minitab® Software, a table of fifteen runs was determined based on the process window presented in Table 5.4. Table 5.5 demonstrates all the runs necessary for the full three-variable Box-Behnken design used in this study. This table was used for all three-

response analysis, that is: lap shear testing, heat input, and contact resistance analysis, producing a multi-response surface analysis. The Minitab® software also randomizes the runs; this allows every experimental sample to have an equal probability of receiving treatment.

Table 5.5 – Box-Behnken Design for three-variables – rotational speed, plunge depth, and plunge speed.

Box Behnken Design				
Run	Block	RS [rpm]	PS [mm/s]	PD [mm]
11	1	1700	1	0.7
5	1	1400	1.6	0.3
7	1	1400	1.6	0.7
10	1	1700	2.2	0.3
13	1	1700	1.6	0.5
12	1	1700	2.2	0.7
9	1	1700	1	0.3
2	1	2000	1	0.5
4	1	2000	2.2	0.5
1	1	1400	1	0.5
15	1	1700	1.6	0.5
14	1	1700	1.6	0.5
6	1	2000	1.6	0.3
8	1	2000	1.6	0.7
3	1	1400	2.2	0.5

5.1.3 Lap Shear Strength

Given the Box-Behnken design, lap shear tests were conducted in the Minitab® software order, Table 5.5. Thirteen runs with different parameters were tested, and then two more at the center points. An analysis of variance study was employed to investigate if the difference between the runs is significant. However, to allow a valid interpretation of the statistical data, it was also necessary to check the model adequacy, which consisted of analyzing the residual plots for an unpatterned scatter of residuals versus fitted value and observation order. The referred graphs and other statistical analyses are presented in Appendix B.

The Lap Shear Strength results are given in Table 5.6. Overall, the spot-welded samples presented good mechanical properties regarding the standard AWS D17.2 [53], used for reference. This standard establishes a minimum load requirement of 425 N for resistance spot welds in which the thinner welded sheet has a nominal thickness of 0.3 mm, and the material used has an ultimate strength above 386 MPa. However, a large variability inside the process window can be observed, ranging roughly from 710 N to 1891 N.

Table 5.6 – Lap Shear Strength Test Results

Run	LSS [N]
11	710.8
5	1134.9
7	1672.0
10	1456.0
13	1682.1
12	1898.7
9	1184.9
2	1174.9
4	1571.7
1	1747.3
15	1344.1
14	1487.0
6	1237.7
8	1612.4
3	1891.8

The Minitab® Software generated the ANOVA table presented in Table 5.7. As mentioned in section 3.7, for the factor to be considered significant in producing different means, that is, to neglect the null hypothesis that the means between treatments are equal, its p-value has to be smaller than the significance level, α. Since the alpha used in this analysis is 0.05 (α = 0.05), it is possible to infer from the table that none of the parameters, nor do their combinations, influence the treatments enough to produce significant differences in the means. However, this type of analysis also contradicts with the significance of the model,

since the p-value of the model stated on the table is also well above 0.05 (0.318). Therefore, the model is inconclusive.

Moreover, the regression equation of this ANOVA analysis showed and R^2 and adjusted R^2 of 74% and 27%, respectively. R^2, the coefficient of determination, shows how well the terms fit the response curve, assuming that every single variable explains the variation in the dependent variable. The adjusted R^2 indicates the percentage of variation explained by only the independent variables that affect the dependent variable. Therefore, an R^2 and adjusted R^2 of 74% and 27%, respectively, suggest that although the terms fit the response curve at a medium-to-high performance, there are many insignificant variables in the equation that do not describe the model.

To rectify this issue, a stepwise regression tool, available in the Minitab® Software, was used to eliminate all the less significant factors with the aim of refining the model.

Table 5.7 – Lap Shear Strength ANOVA table.

Source	DF	Adj SS	Adj MS	F-Value	P-Value
Model	9	1094896	121655	1.59	0.318
Linear	3	687140	229047	2.99	0.135
RS	1	90159	90159	1.18	0.328
PS	1	500095	500095	6.52	0.051
PD	1	96887	96887	1.26	0.312
Square	3	175087	58362	0.76	0.562
RS*RS	1	34627	34627	0.45	0.531
PS*PS	1	86	86	0.00	0.975
PD*PD	1	129128	129128	1.68	0.251
2-Way Interaction	3	232668	77556	1.01	0.461
RS*PS	1	15906	15906	0.21	0.668
RS*PD	1	6594	6594	0.09	0.781
PS*PD	1	210168	210168	2.74	0.159
Error	5	383509	76702		
Lack-of-Fit	3	325958	108653	3.78	0.216

Pure Error	2	57551	28775
Total	14	1478405	

The stepwise regression is a method of fitting regression modes in which the choice of predictive variables is carried out by an automatic procedure. The approach used in this study was the backward elimination method. This technique involves starting with all candidate variables, testing the deletion of each variable using a chosen model fit criterion, deleting the variable whose loss gives the most statistically insignificant deterioration of the model fit, and repeating this process until no further variables can be deleted without a statistically significant loss of fit.

In this study, arbitrary values of alpha to remove (α_r) were depicted to consider exclusively the most significant factors in the experiment, creating a new analysis of variance and regression model. However, it was also necessary to keep in mind that by removing factors, however insignificant, the coefficient of determination, R^2, is diminished. This happens because the more factors present in the regression model, the easier it is to fit all the experimental values inside the regression equation. However, if the terms are insignificant, then the adjusted R^2, which compares the explanatory power of regression models that contain a different number of predictors, is also diminished. Hence, a compromise between neglecting insignificant factors without obtaining a low R^2 was made.

After testing various alphas to remove, it was found that $\alpha_r = 0.21$ was the best considering p-values and determination coefficients. Minitab then generated a new ANOVA table, presented in Table 5.8. It appears that two squared (RS^2, PS^2) and two interaction factors (RS*PS, RS*PD) were considered negligible. After recalculating the p-values, it becomes clear that the linear relationships ($p = 0.031$) are the most dominant in modeling the response, and that plunge speed is the only significant factor with an $\alpha = 0.05$. Moreover, the resulting model presents an R^2 and adjusted R^2 of 70.2% and 53.7%, respectively. This suggests that the backwards elimination of terms was efficient in eliminating the insignificant terms of the response equation – by increasing the adjusted R^2 from 27% to 54% – without significantly compromising the determination coefficient. Higher α_r would lower R^2 crucially and weaken the regression model further. The

regression model given by the Minitab® Software, after the backwards elimination of terms, is presented in Eq. 5.

Table 5.8 – Lap Shear Strength ANOVA table after backwards elimination with $\alpha_r = 0.21$

Source	DF	Seq SS	Contrib.	Adj SS	Adj MS	F-Value	P-Value
Model	5	1037208	70.16%	1037208	207442	4.23	0.030
Linear	3	687140	46.48%	687140	229047	4.67	0.031
RS	1	90159	6.10%	90159	90159	1.84	0.208
PS	1	500095	33.83%	500095	500095	10.20	0.011
PD	1	96887	6.55%	96887	96887	1.98	0.193
Square	1	139900	9.46%	139900	139900	2.85	0.125
PD*PD	1	139900	9.46%	139900	139900	8.85	0.125
2-Way Interaction	1	210168	14.22%	210168	210168	4.29	0.068
PS*PD	1	210168	14.22%	210168	210168	4.29	0.068
Error	9	441197	29.84%	441197	49022		
Lack-of-Fit	7	383646	25.95%	383646	54807	1.90	0.387
Pure Error	2	57551	3.89%	57551	28775		
Total	14	1478405	100%				

$$LSS\ (N) = 1535 - 0.354\ RS - 538\ PS + 2333\ PD - 4839\ PD^2 + 1910\ PS * PD \quad (5.5)$$

Eq. 5.5 demonstrates the relationship of each parameter to the lap shear strength response. It was found that RS and PS are linearly proportional to LSS and that PD has a linear and squared coefficient in the equation. Moreover, inside the studied process window, RS is inversely linear to LSS. Hence low RS provided the highest lap shear strength, contrary to what was found by Amancio et al. [10] and Tier et al. [51].

Response surface graphs of each parameter are depicted in Figure 5.6. Figure 5.6a, which indicates the effects of plunge depth and plunge speed on LSS, shows that the highest lap shear strength is obtained using high plunging speeds with medium-to-high plunge depths. The curve demonstrates a quadratic behavior to plunge depth, as was analyzed in the regression equation (Eq. 5). Figure 5.6b, which indicates the effects of plunge depth and rotational speed on

LSS, shows that the highest values of LSS are found in welds produced with low rotational speeds and high plunge depths. Lastly, Figure 5.6c, which indicates the effects of plunge speed and rotational speed on LSS, demonstrates the linear correlation between these two parameters and the LSS response. It appears that the highest lap shear strength values are found in welds produced with high plunge speeds and low rotational speeds.

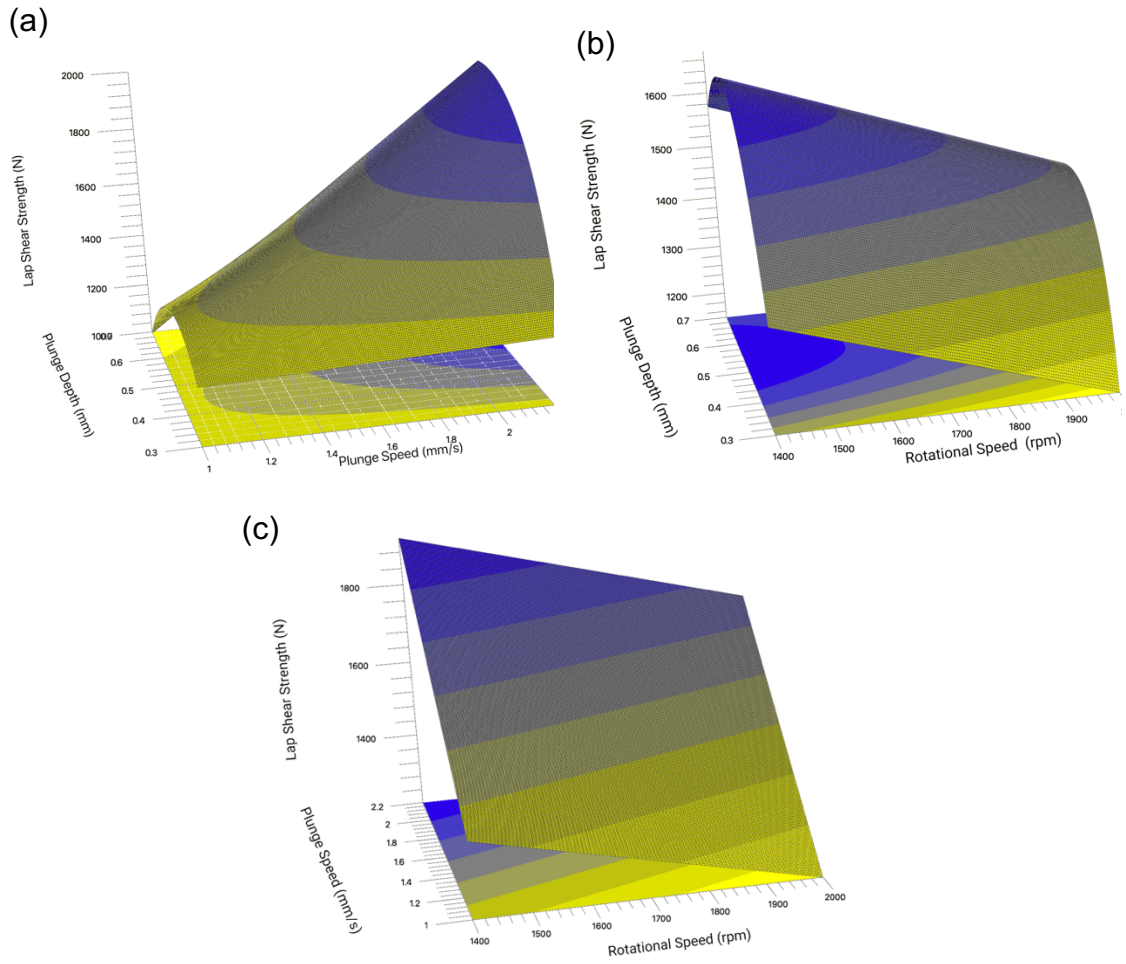

Figure 5.6 – Response surface curve for the effects (a) plunge depth (mm) and plunge speed (mm/s), (b) plunge depth (mm) and rotational speed (rpm), and (c) plunge speed (mm/s) and rotational speed (rpm) on the value of lap shear strength (N).

Subsequently, Minitab® Software was used to obtain the optimized parameters, that is, the combination of all three parameters that would maximize the lap shear strength. It was found that the highest lap shear strength would be provided by a weld produced with a rotational speed, plunge speed, and plunge depth of 1400 rpm, 2.2 mm/s, and 0.67 mm, respectively. Figure 5.7 depicts each parameter's optimization curves regarding LSS and the response behavior when varying all parameters separately, in which the constant values were taken from

the optimized combination (1400 rpm, 2.2 mm/s, 0.67 mm). This study found that LSS is inversely linear to RS, linear to PS, and presents a quadratic relationship to PD.

Moreover, the Minitab® Software predicted that the optimized combination of parameters would produce a weld with a lap shear strength of 2062 N. Welds produced with such parameter combination were tested for lap shear strength to confirm the predicted values. The obtained LSS was 1724.9 $\pm$ 213 N.

Table 5.8 also shows the contribution of each process parameter regarding their influence on the studied response. It was found that the plunge speed is the most influential parameter, with a contribution of 33.83%. This was the only parameter that presented a p-value lesser than 0.05, indicating that it is the only parameter that significantly influences the response with a confidence interval of 0.95. However, the interaction between plunge depth and plunge speed also showed a p-value close to 0.05 (0.068), indicating that the combination of PD and PS parameters was potentially significant to the LSS response inside the studied process window.

Since the plunge speed is the distance the tool penetrates the material per minute, it can also easily be related to joining (welding) time, which is another parameter commonly studied in refill FSSW optimization. In this regard, joining time has been previously indicated as strongly influential to the weld's mechanical properties by other authors [9, 33, 35]. This is mainly correlated to the elevation in thermal energy generated by increasing joining time, which causes the enlargement of the welded area and, therefore, the section of material resistant to mechanical load.

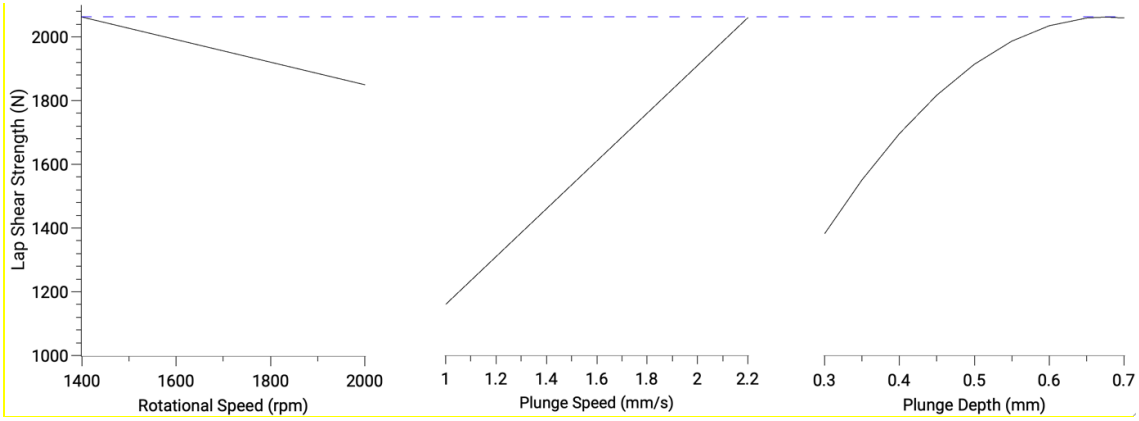

Figure 5.7 – Effect of RS, PS, and PD on LSS and the optimized parameters for maximization of LSS.

Plunge depth and rotational speed, however, demonstrated a contribution of approximately 6% to the lap shear strength response, as seen in Table 5.8. Regarding rotational speed, low contribution to process temperature was expected since many published works [10, 42, 54] have shown that the RS is mostly influential when its interaction with other parameters, such as welding time and dwell time, are analyzed. This is because although an increase in RS increases the heat input, high RS also depreciates the frictional regime of the plasticized material due to tool slippage. Therefore, less thermal energy is produced resulting in smaller welded areas and a reduction in LSS. But, in the analysis of variance presented in Table 5.8, no parameter interactions with rotational speed showed significant influence, as they were removed from the analysis by backward elimination.

Regarding plunge depth, a higher contribution from this parameter to the LSS response was originally expected due to the weld's multilayer characteristic. It was hypothesized that higher plunge depths would provide better bonding between all commercially pure aluminum foils. However, it was found that the interaction between plunge depth and plunge speed was more influential in the weld's global mechanical properties than the linear plunge speed factor. Nonetheless, Figure 5.7 shows that an increase in PD from 0.3 mm to 0.5 mm, while maintaining PS and RS constant, increases LSS by approximately 35% and that increasing PD further would only increase LSS by nearly 10%. This suggests that PD has a significant effect on LSS in the lower range of the PD process window and that this effect decreases as PD values above 0.5 mm are used.

5.1.4 Process Temperature

As mentioned in section 5.1.2, the design of experiments was planned so that the same Box-Behnken model would be used for LSS, heat input and contact resistance. After analyzing the LSS results and refining the ANOVA table, heat input experiments were carried out. As mentioned in section 4.5, an infrared (IR) camera was used to measure the maximum temperature achieved on the upper sheet's surface during the welding process. Figure 5.8 shows the maximum temperature measurements of all parameter combinations using the IR camera.

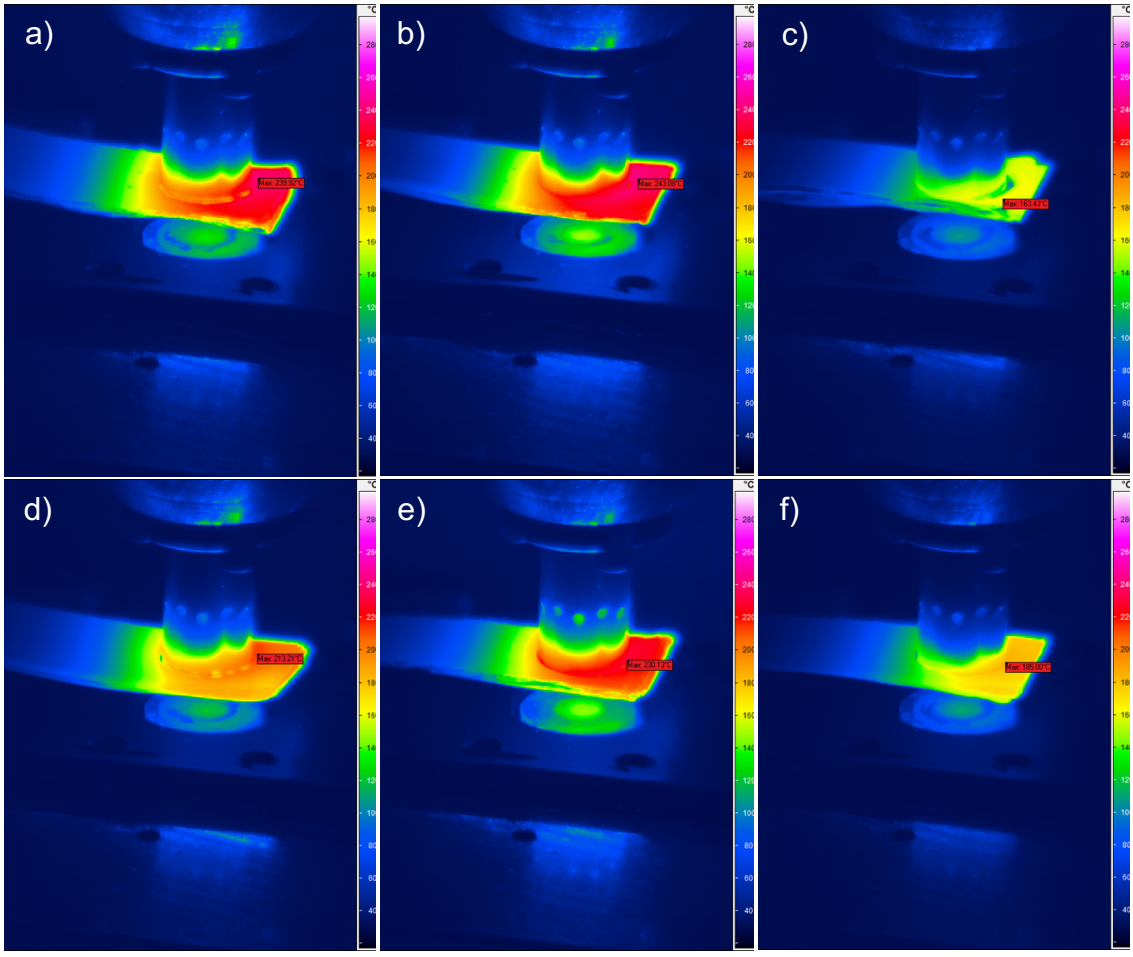

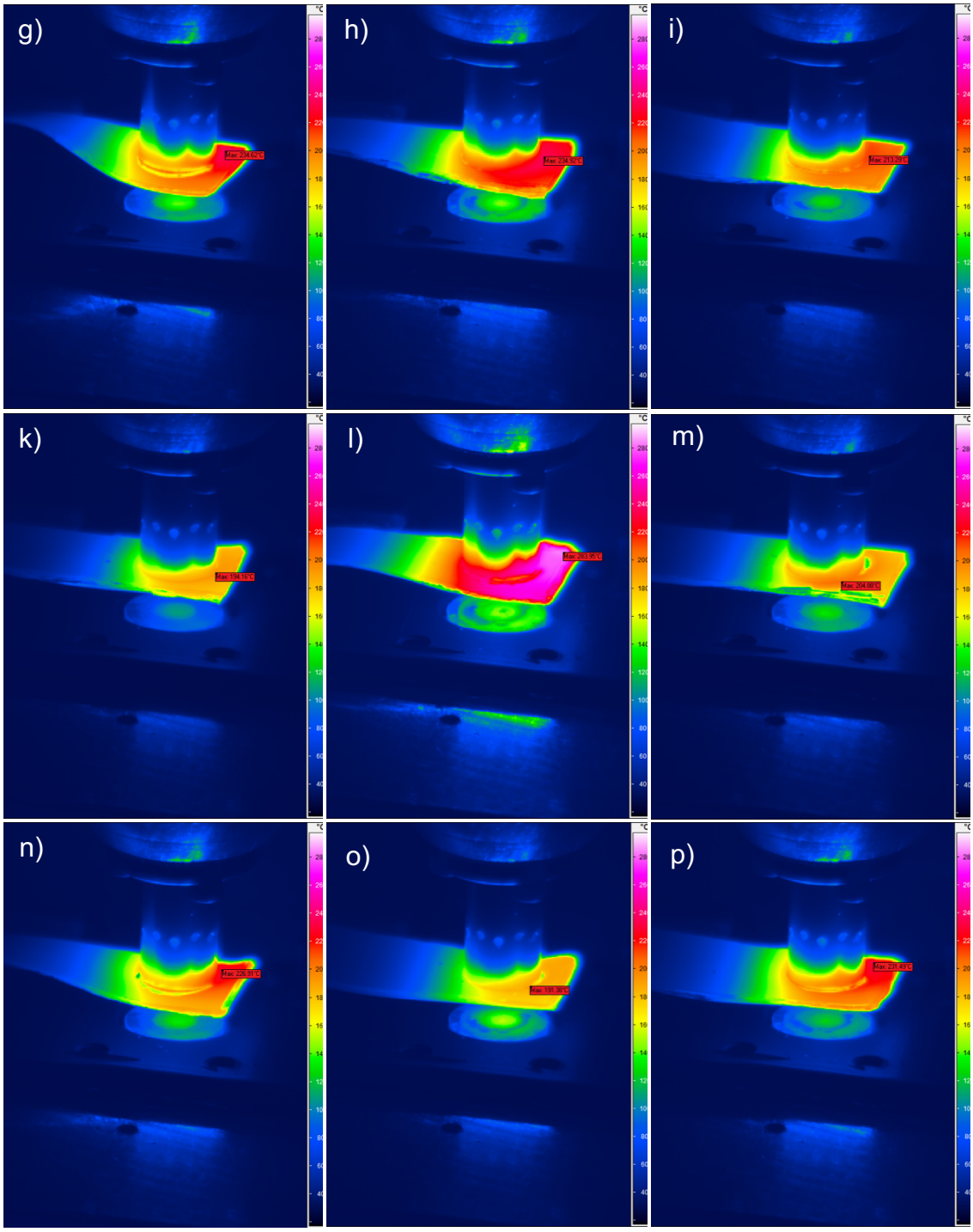

Figure 5.8 – Infrared images of maximum temperature measurements during welding of specimens produced with parameter combinations 1-15, indicated by images (a)-(p) in respective order. Parameter combinations are detailed in Table 5.5.

Through IR analysis, it was possible to obtain crucial information regarding the temperatures achieved on the sheet and the safety of using refill FSSW for welding battery pouches. In this regard, it was possible to measure and identify the

1. Maximum temperature of the sheet during welding;
2. the location of the maximum temperature;
3. the distance from the point of maximum temperature to a point which temperature never achieves 80ºC; and
4. the time it takes for the maximum temperature to cool down below 80ºC.

However, for statistical analysis, only the value of the maximum temperature achieved was used as a response in the Box-Behnken design to avoid complexity. Moreover, since the heat is transferred through conduction, high temperatures are correlated to more considerable distances from points of high to low temperatures. Hence, the analysis of the behavior of (1) and its correlation to processing parameters can be analogous to analyzing (3) and (4).

Table 5.9 indicates the values of the measurements made. It was found that maximum temperatures ranged from 163 °C to 283 °C; the distance from the center of the weld to the location on the sheet which temperature never achieved values above 80ºC ranged from 32 mm to 89 mm, and the time it takes for the maximum temperature takes to reduce to 80ºC varied from 10s to 22s. Regarding the location of the hotspot, the maximum temperature was always achieved immediately outside the clamping ring.

Table 5.9 – Infrared Camera Measurements

Run	T_{max} (°C)	Time for T_{max} to reach 80ºC (s)	Distance from T_{max} to T < 80ºC (mm)
11	283.9	22	89
5	230.1	18	71
7	234.6	13	72
10	194.2	11	42
13	226.9	14	58
12	204.9	14	50
9	213.3	13	52
2	243.1	17	71
4	213.2	14	60
1	239.9	15	71
15	231.5	17	62
14	192.0	12	47
6	185.0	10	37

8	234.9	17	66
3	163.4	10	32

Although it appears that all combinations of parameters inside the chosen process window produced welds that achieved temperatures above the 80 °C limit, short distances were obtained from the hotspot to 80ºC. This suggests that refill FSSW can be used to weld multilayered materials in batteries if the distance between the spot weld and the electrochemically active materials is accounted. Therefore, a statistical analysis of each processing parameter's influence on the maximum temperature and obtaining the combination of optimized parameters is convenient for the application.

The analysis of variance study conducted to evaluate each parameter's influence on the maximum temperature of the spot-welding process is shown in Table 5.10. As was done for the LSS analysis, an adequacy check of the model was carried out to confirm that the residual scatter did not present any pattern. Graphs for such analysis and others are presented in Appendix C.

Table 5.10 – Heat Input ANOVA table

Source	DF	Adj SS	Adj MS	F-Value	P-Value
Model	9	9677.1	1075.24	2.42	0.172
Linear	3	7528.2	2509.39	5.65	0.046
RS	1	7.7	7.70	0.02	0.900
PS	1	5216.3	5216.29	11.74	0.019
PD	1	2304.2	2304.19	5.19	0.072
Square	3	198.4	66.13	0.15	0.926
RS*RS	1	20.5	20.46	0.05	0.839
PS*PS	1	1.1	1.09	0.00	0.962
PD*PD	1	167.5	167.55	0.38	0.566
2-Way Interaction	3	1950.6	650.19	1.46	0.330
RS*PS	1	536.8	536.85	1.21	0.322
RS*PD	1	515.5	515.52	1.16	0.331
PS*PD	1	898.2	898.20	2.02	0.214
Error	5	2220.9	444.18		

Lack-of-Fit	3	1286.4	428.79	0.92	0.559
Pure Error	2	934.5	467.27		
Total	14	11898.0			

The ANOVA table (Table 5.10) indicates that the model's p-value is 0.172, and, therefore, above the significance level (0.05). Also, the R^2 and R^2 adjusted values, which demonstrate how well the regression equation describes the model's response, were 81% and 48%, respectively. This suggests that the model is not appropriate to analyze the response. To rectify this issue, a stepwise regression measure was conducted using the backward elimination tool. The explanation of this tool and how it is used is elaborated in detail in section 5.1.3. In this case, $\alpha_r = 0.23$ was used. The new ANOVA table generated is shown in Table 5.11, in which the model has a p-value of 0.018 (below the significance level), and the regression equation is shown in Eq. 6.

Table 5.11 – Heat Input ANOVA table after backward elimination with $\alpha_r = 0.23$

Source	DF	Seq SS	Contrib.	Adj. SS	Adj. MS	F-Value	P-Value
Model	6	9478.7	79.67%	9478.75	1579.79	5.22	0.018
Linear	3	7528.2	63.27%	7528.18	2509.39	8.3	0.008
RS	1	7.7	0.06%	7.7	7.7	0.03	0.877
PS	1	5216.3	43.84%	5216.29	5216.29	17.25	0.003
PD	1	2304.2	19.37%	2304.19	650.19	7.62	0.025
2-Way Interaction	3	1950.6	16.39%	1950.57	536.85	2.15	0.172
RS*PS	1	536.8	4.51%	536.85	515.52	1.78	0.219
RS*PD	1	515.5	4.33%	515.52	898.2	1.7	0.228
PS*PD	1	898.2	7.55%	898.2	302.41	2.97	0.123
Error	8	2419.3	20.33%	2419.29	247.46		
Lack-of-Fit	6	1484.7	12.48%	1484.75	467.27	0.53	0.769
Pure Er.	2	934.5	7.85%	934.54			
Total	14	11898	100%				

$$T_{max}\ (°C) = 476 - 0.194\ RS - 89.5\ PS - 37\ PD + 0.06444\ RS * PS + 0.189\ RS * PD - 124.9\ PS * PD \quad (5.6)$$

Eq. 5.6 demonstrates that T_{max} is best described as a function of all linear factors – RS, PS, and PD – and the 2-way interactions between the three parameters. The backwards regression method eliminated the equation's squared variables to improve R^2 and R^2 adjusted to 80% and 64%, respectively. That is, the squared variables (RS^2, PS^2, PD^2) were removed without compromising the fit of the regression equation.

Table 5.11 indicates that PS (p-value = 0.003) and PD (p-value = 0.025) are influential factors to the T_{max} response and that the means of combinations with different RS are not significantly different. Moreover, the ANOVA table shows that RS has a contribution of only 0.06% to the measured T_{max}. This is contrary to the initial assumption, based on the findings of Su et al.[55], that rotational speed is highly responsible for the process temperature. Su et al.[55] introduced Eq. 5.7 to describe the energy input in friction stir spot welding, which states that energy is determined by axial force, penetration depth, rotational speed, and torque. Then,

$$Q_{applied} = \sum_{n=1}^{n=N} Force(n)(x_n - x_{n-1}) + \sum_{n=1}^{n=N} Torque(n)\omega(n)\Delta t \qquad (5.7)$$

where x_n is the penetration depth at sample (n), ω is the angular velocity (rad s^{-1}), n in the sample number, N is the final sample, and Δt is the sampling time. Moreover, it was found that the energy contribution resulting from tool rotation is 160 times higher than that due to tool penetration.

Response surface graphs of each parameter are depicted in Figure 5.9. Figure 5.9a, which indicates the effects of plunge depth and plunge speed on T_{max}, shows that the highest temperature is obtained using low plunging speeds with high plunge depths. This can be interpreted as the temperature being strongly correlated to the amount of time the tool rotates inside the material. Moreover, it was found that at high plunge speeds, the variation of plunge depth did not significantly affect the measured process temperature. Therefore, in summary, lower process temperatures are achieved with faster welds for a constant rotational speed. Figure 5.9b, which indicates the effects of plunge depth and rotational speed on T_{max}, shows that, at low rotational speeds, the temperature does not vary considerably with plunge depth. However, at high

rotational speeds, the process temperature varies significantly with plunge depth, indicating temperatures as high as 250ºC for high PD and 190ºC for low PD. Lastly, Figure 5.9c, which indicates the effects of plunge speed and rotational speed on T_{max}, demonstrates that low temperatures are achieved using high plunge speeds and that varying rotational speeds do not significantly influence the process temperature.

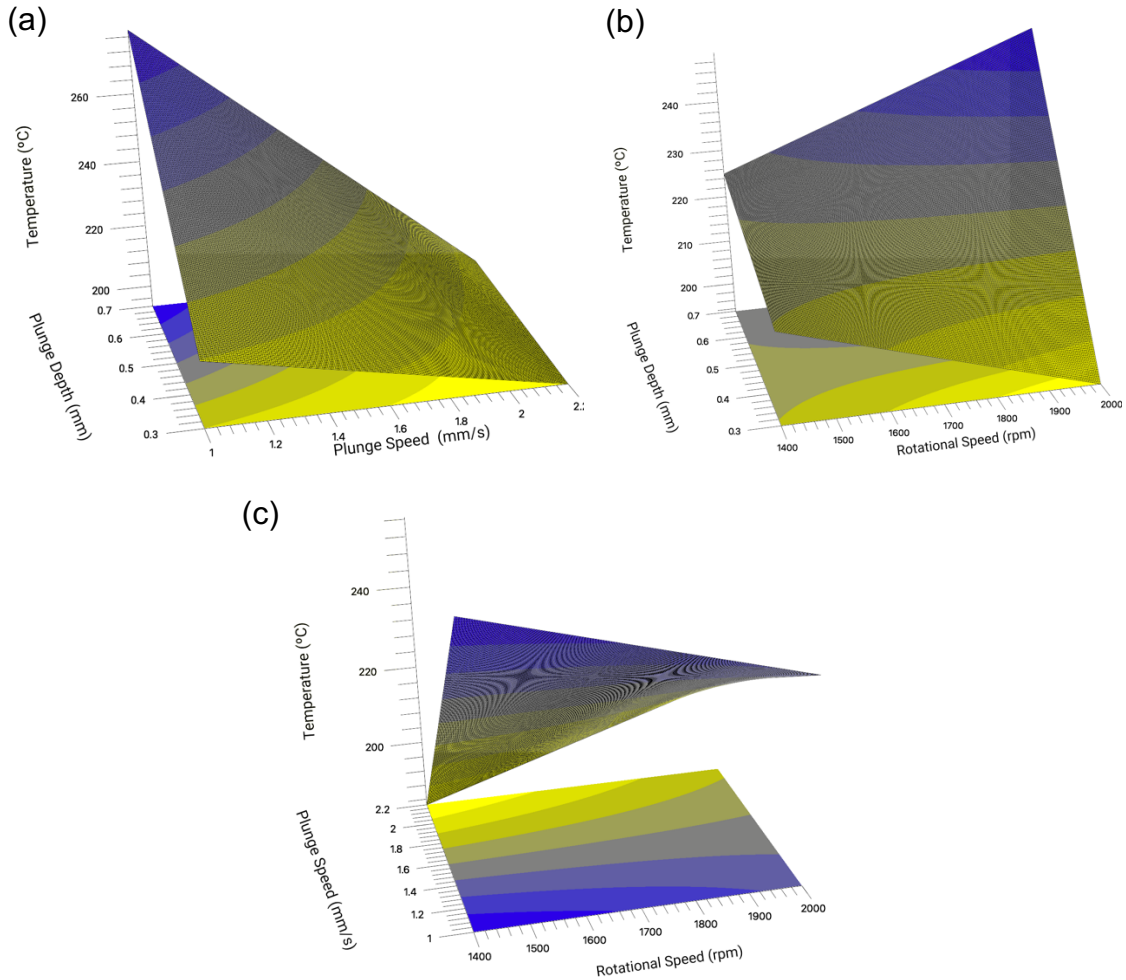

Figure 5.9 – Response surface curve for the effects (a) plunge depth (mm) and plunge speed (mm/s), (b) plunge depth (mm) and rotational speed (rpm), and (c) plunge speed (mm/s) and rotational speed (rpm) on the value of temperature (ºC).

The Minitab® Software was used to optimize the parameters with the aim of minimizing the maximum temperature achieved during welding. Figure 5.10 shows the parameter combination that gives the minimum heat input during welding. According to the regression model, a weld produced with 1400 rpm, a plunge speed of 2.2 mm/s, and plunge depth of 0.7 mm produces a weld with the lowest possible process temperature, predicting a T_{max} of 172ºC.

Figure 5.10 also demonstrates the response behavior when varying all parameters separately, in which the constant values were taken from the optimized combination (1400 rpm, 2.2 mm/s, 0.7 mm). It appears that when high PS and PD are used, increasing RS from 1400 rpm to 2000 rpm increases T_{max} by approximately 50ºC, indicating that low RS is optimal for low process temperatures in refill FSSW of multilayered welds. When low RS and high PS are used, varying plunge depth does not significantly influence process temperature. Nonetheless, it is evident that with RS and PD constant at 1400 rpm and 0.7 mm, respectively, plunge speed strongly affects T_{max}, indicating that low temperatures are correlated to high welding speeds.

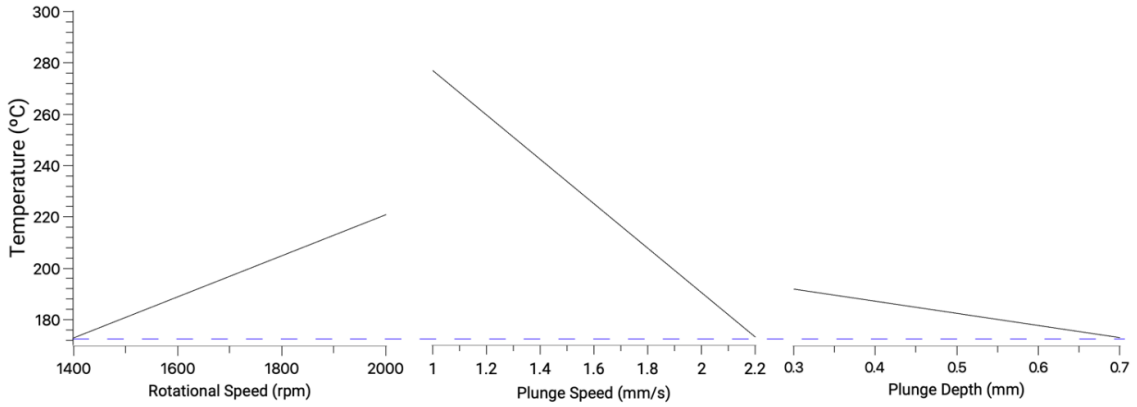

Figure 5.10 – Effect of RS, PS, and PD on LSS and the optimized parameters for minimization of process temperature.

5.1.5 Contact Resistance

Contact resistance measurements were also analyzed using the Box-Behnken model presented in section 5.1.2. However, due to the nature of the test, the values given in milliohms varied significantly from one measurement to another. Therefore, three measurements were taken for every weld, and the average between the values was considered for statistical analysis. Table 5.12 presents the contact resistance values for each weld. Standard deviation was also added, but not used in the response surface analysis.

Table 5.12 – Contact resistance measurements

Run	CR (mΩ)	Std. Dev. (mΩ)
11	0.328	0.002
5	0.250	0.021
7	0.145	0.001

10	0.382	0.003
13	0.307	0.006
12	0.295	0.001
9	0.382	0.002
2	0.148	0.007
4	0.366	0.004
1	0.328	0.001
15	0.191	0.002
14	0.224	0.016
6	0.188	0.004
8	0.245	0.001
3	0.275	0.018

An analysis of variance was also carried out based on the results obtained, which varied from 0.145 mΩ to 0.382 mΩ. As in previous sections, an adequacy check of the model was made to analyze the residual behavior and check if any patterns would invalidate the model. The graphs used for this study and other statistical analyses are presented in Appendix D. After concluding that the model is adequate through the residual analysis, the ANOVA table (Table 5.13) generated by the Minitab® Software was studied.

Table 5.13 – ANOVA table for Contact Resistance.

Source	DF	Adj. SS	Adj. MS	F-Value	P-Value
Model	9	33.9044	3.7672	0.89	0.586
Linear	3	9.8963	3.2988	0.78	0.553
RS	1	0.5000	0.5000	0.12	0.745
PS	1	9.2450	9.2450	2.19	0.199
PD	1	0.1512	0.1512	0.04	0.857
Square	3	21.3757	7.1252	1.69	0.284
RS*RS	1	12.7510	12.7510	3.02	0.143
PS*PS	1	3.0464	3.0464	0.72	0.434
PD*PD	1	4.6041	4.6041	1.09	0.344
2-Way Interaction	3	2.6325	0.8775	0.21	0.887
RS*PS	1	0.4225	0.4225	0.10	0.764
RS*PD	1	1.9600	1.9600	0.46	0.526

PS*PD	1	0.2500	0.2500	0.06	0.817
Error	5	21.1029	4.2206		
Lack-of-Fit	3	9.5013	3.1671	0.55	0.698
Pure Error	2	11.6017	5.8008		
Total	14	55.0073			

The ANOVA table presented showed that the model's p-value is 0.586, well above the significance level, which contradicts the conclusions from the table. This issue was also reported for lap shear strength and process temperature in sections 5.1.4 and 5.1.5, respectively. Therefore, a stepwise regression method was used to improve the statistical analysis, in which the insignificant terms to the model were eliminated. Therefore, α_r = 0.14 was used for backward elimination and a new ANOVA table, Table 5.14, was obtained.

Table 5.14 – Contact Resistance ANOVA table after backward elimination with α_r = 0.14.

Source	DF	Adj SS	Contrib.	Adj SS	Adj MS	F-Value	P-Value
Model	7	0.073291	81.66%	0.073291	0.010470	4.45	0.034
Linear	3	0.007065	7.87%	0.007065	0.002355	1.00	0.446
RS	1	0.000321	0.36%	0.000321	0.000321	0.14	0.723
PS	1	0.002200	2.45%	0.002200	0.002200	0.94	0.366
PD	1	0.004544	5.06%	0.004544	0.004544	1.93	0.207
Square	2	0.041440	46.17%	0.041440	0.020720	8.81	0.012
RS*RS	1	0.012693	14.14%	0.010053	0.010053	4.28	0.077
PS*PS	1	0.028747	32.03%	0.028747	0.028747	12.23	0.010
2-Way Interaction	2	0.024786	27.62%	0.024786	0.012393	5.27	0.040
RS*PS	1	0.018225	20.31%	0.018225	0.018225	7.75	0.027
RS*PD	1	0.006561	7.31%	0.006561	0.006561	2.79	0.139
Error	7	0.016458	18.34%	0.016458	0.002351		
Lack-of-Fit	5	0.009291	10.35%	0.009291	0.001858	0.52	0.761
Pure Error	2	0.007167	7.99%	0.007167	0.003584		
Total	14	0.089749	100%				

$$CR\ (m\Omega) = 0.851 + 0.001007 * RS - 1.392 * PS - 1.267 * PD - 0.000001 * RS^2 + 0.2444 * PS^2 + 0.000375 * RS * PS + 0.000675 * RS * PD \quad (5.8)$$

Although the model's p-value is below the significance level, all linear factors present p-values above 0.05, suggesting that no single parameter influences the contact resistance enough to neglect the null hypothesis. However, the square and 2-way interactions showed p-values of 0.012 and 0.040, respectively. This indicates that the contribution from the squared parameters and their interactions are significant to the contact resistance. Specifically, the terms with plunge and rotational speed (PS^2, RS*PS) demonstrated p-values lower than 0.05.

Therefore, although the linear terms did not neglect the null hypothesis, plunge speed was significantly influential to the contact resistance response due to its interactions with other parameters and its square component. Analogously, the rotational speed is also influential, as its interaction with plunge speed account for a p-value of 0.027. Moreover, it was found that plunge depth does not contribute significantly to the weld's contact resistance. This is unlikely since this parameter influences the number of unbonded interfaces in the CP-Al foils located at the weld's center, as shown in section 5.2.2.2, impacting the electrical current's path through the weld.

Response surface graphs of each parameter are depicted in Figure 5.11. Figure 5.11a, which indicates the effects of plunge depth and plunge speed on contact resistance, shows that the lowest resistance is obtained using intermediate plunging speeds with high plunge depths. This corroborates the hypothesis that higher PD increases the number of bonded CP-AL foils and, therefore, diminishes the number of barriers to the passage of current. Moreover, lower CR with intermediate welding speeds suggests that this parameter provides better paths for electrical current – improved mixing, more bonded CP-Al foils – when medium-to-high values are used. Also, Figure 5.11a shows that when low and high plunge speeds are used, varying plunge depth does not significantly affect the contact resistance, indicating the predominant influence of PS on CR, seen in Table 5.14.

Figure 5.11b indicates the effects of plunge depth and rotational speed on contact resistance. It was found that minimum resistances are achieved either with high PD and low RS or with low PD and high RS. Welds produced with

intermediate values of PS and RS present high resistances to the passage of electrical current. This is indicative that the interaction of these parameters is more influential than their linear components, also demonstrated in Table 5.14 through p-value analysis.

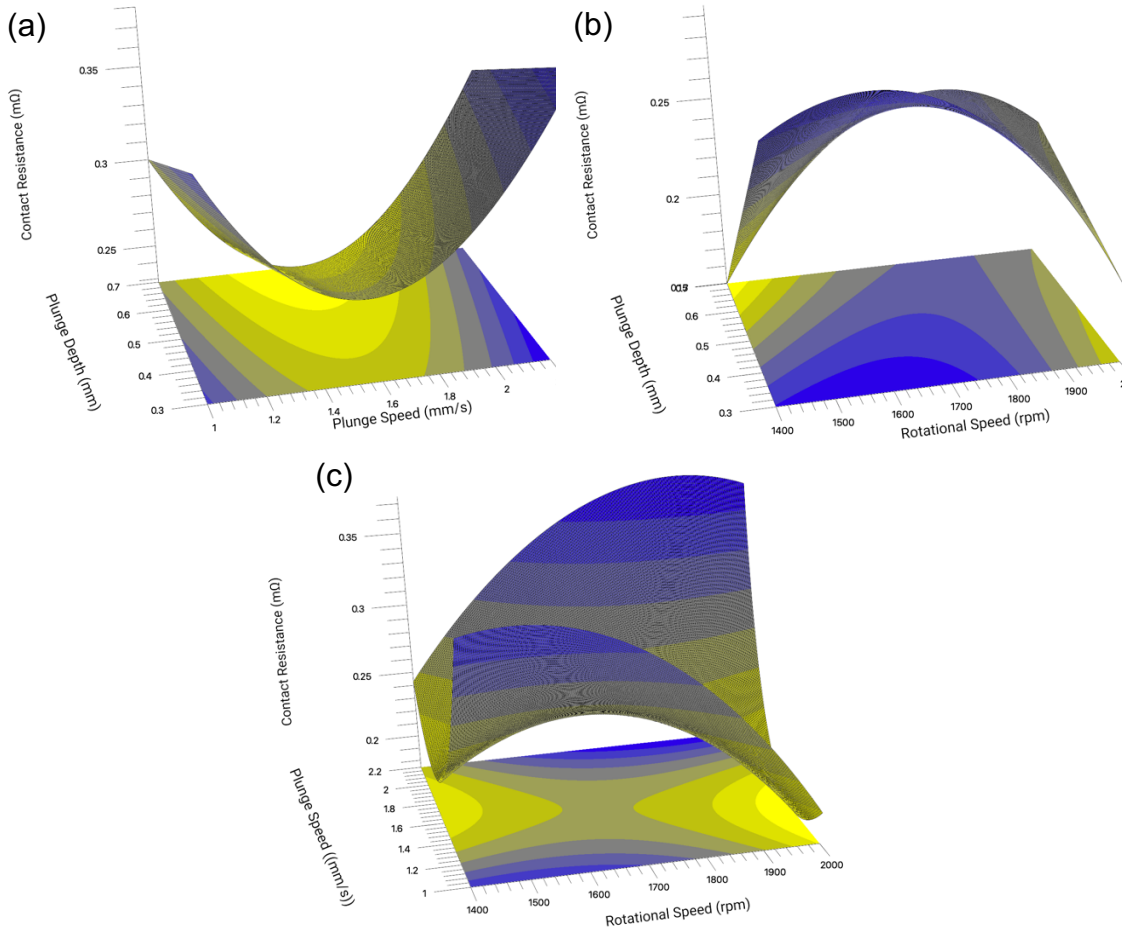

Figure 5.11:Response surface curve for the effects (a) plunge depth (mm) and plunge speed (mm/s), (b) plunge depth (mm) and rotational speed (rpm), and (c) plunge speed (mm/s) and rotational speed (rpm) on the value of contact resistance (mΩ).

Lastly, Figure 5.11c indicates the effects of plunge speed and rotational speed on contact resistance. The response curve indicates that minimum contact resistances are obtained when intermediate plunge speeds are used, combining either high or low rotational speeds. This also demonstrates that the interaction between these parameters is more influential than their linear components.

Minitab® Software was used to obtain the optimization curves, presented in Figure 5.12, to minimize the contact resistance. It was found that, based on the proposed analysis, the combination of parameters that produces the weld with the lowest contact resistance is with an RS, PS, and PD of 1400 rpm, 1.77 mm/s,

and 0.7 mm, respectively. This combination is projected to produce a weld with a resistance of 0.134 mΩ.

Therefore, the optimization curves depict the response behavior when varying all parameters separately, in which the constant values were taken from the optimized combination (1400 rpm, 1.77 mm/s, 0.7 mm). It was found that rotational speed and plunge speed have a negative and positive quadratic behavior, respectively. In contrast, plunge depth has a linear behavior to CR.

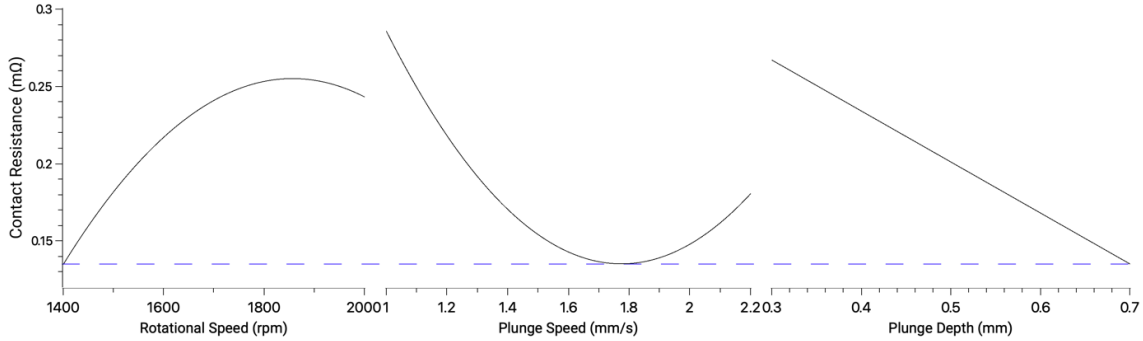

Figure 5.12 – Effect of RS, PS, and PD on LSS and the optimized parameters for minimization of contact resistance.

Nonetheless, it is noteworthy to mention that the method used to measure contact resistance is subject to error. Also, the high standard deviations suggest that other factors influence the electrical resistance, such as plate roughness, impurities, heterogeneity, and the pressure applied by the leads. Therefore, it is likely that this analysis can be improved with more appropriate methods for electrical resistance measurements.

5.1.6 Multiple response

After analyzing the influence of each parameter on the properties of the weld and obtaining an optimized combination of parameters for each individual response, a multiple-response optimization was carried out. Through multiple-response analysis, it was possible to obtain a combination of parameters that would attain the desired overall properties of the weld, that is, minimal process temperature and contact resistance with high lap shear strength. As mentioned in section 3.1, these properties are desired for the electrical vehicle battery application because: high temperature can damage the electrochemically active materials inside the cell casing; the weld has to provide low resistance to the

passage of current to avoid compromising the effectiveness of the battery; and high mechanical properties are required to resist the mechanical solicitations originated from constant vibrations and potential accidents.

This optimization was carried out using the Box-Behnken model presented in section 5.1.2. From the optimization curves presented in Figure 5.13, the software developed a desirability function where all three responses were given equal weight. Given that the properties behave differently regarding each individual process parameter, the desirability function for each property was not always 1.0; however, the Minitab® Software chose a combination of parameters that would give the highest composite desirability (D: 0.9307).

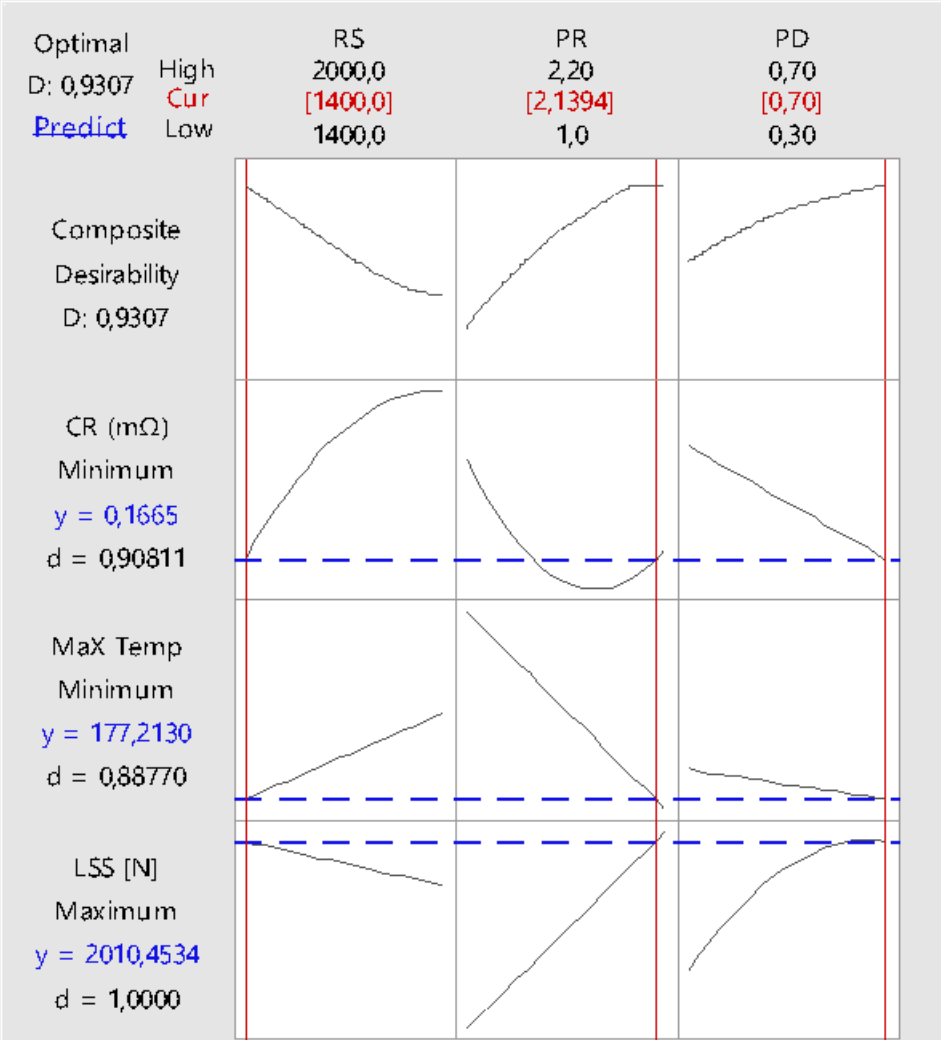

Figure 5.13 – Multiple-response Optimization

Therefore, the combination of parameters that produced the weld with the best-desired properties consists of a rotational speed of 1400 rpm, a plunge depth of 0.7 mm, and a plunge speed of 2.2 mm/s.

5.2 One-Factor-At-A-Time

After the optimization branch of this project was performed through ANOVA and Minitab Software® analysis, it was decided to adopt a second methodological approach for analyzing the influence of the process parameters on the properties of the joint and its microstructure. This would allow a comprehensive study of the *Processing – Properties – Microstructure* relationship. Although the optimization curves depicted in sections 5.1.3, 5.1.4, 5.1.5, and 5.1.6 already present trend lines that suggest how each property behaves regarding process parameters, a second statistical method was desired to experimentally study and measure these properties and correlate them with their corresponding microstructure. Therefore, the one-factor-at-a-time (OFAT) methodology was used, where all three process parameters were varied in three levels, as shown in Table 5.15. The baseline condition, indicated in bold, used in this study consists of the combination of parameters presented in section 5.1.6 since this combination produced the optimal weld for the desired properties.

Table 5.15 – Parameters used in OFAT study, indicating the baseline condition.

Rotational Speed (rpm)	Plunge Speed (mm/s)	Plunge Depth (mm)
1100	1.7	0.3
1400 (Baseline)	**2.1 (Baseline)**	0.5
1700	2.5	**0.7 (Baseline)**

The combinations of parameters used are depicted in Table 5.16. Three samples were produced with each parameter's combination to be tested for each response: mechanical properties, process temperature, and contact resistance. A fourth sample was produced for metallographic analysis.

Table 5.16 – Welding parameter combinations.

Weld Param.	RS (rpm)	PS (mm/s)	PD (mm)	PT (s)
1	1100	2.1	0.7	0.333
2	1700	2.1	0.7	0.333
3	1400	1.7	0.7	0.412

4	1400	2.5	0.7	0.280
5	1400	2.1	0.3	0.143
6	1400	2.1	0.5	0.238
7	1400	2.1	0.7	0.333

5.2.1 Property Measurement

Figure 5.14 contains the lap shear strength, process temperature, time required for the weld's hotspot to reach below 80ºC, and the welds' contact resistance with the combination of parameters presented in Table 5.16. To better understand the influence of process parameters in the weld's properties, each parameter will be analyzed separately in Figure 5.15 - Figure 5.17. Moreover, the weld's fracture mode when subjected to a lap shear test is explained in greater detail in section 5.4.

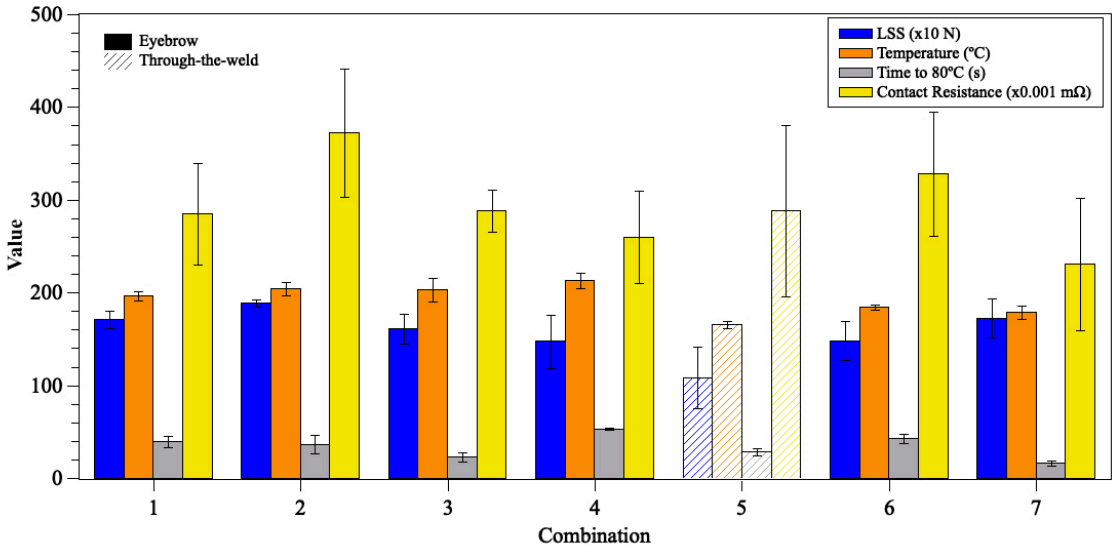

Figure 5.14 – Lap shear strength (N), process temperature (ºC), time to 80ºC (s), and contact resistance (mΩ) of welds produced with process parameters referenced in Table 5.16.

Figure 5.15 indicates the weld's mechanical and electrical properties, as well as heat input, when varying plunge depth. It is clear that the weld's lap shear strength increases with increasing plunge depth. This behavior was also reported in section 5.1.3, in which the Minitab Software® optimization analysis indicated that LSS was higher in welds produced with higher plunge depths. In the OFAT analysis, the average LSS increased from 1084 N to 1725 N by increasing PD from 0.3 mm to 0.7 mm, respectively.

The process temperature study showed that very low plunge depths (0.3 mm) lead to low temperatures (165 ºC), which can be correlated to less material being plasticized due to the adjustable shoulder's shorter reach to the material during plunging. However, the temperature curve shows that high plunge depths (0.7 mm) indicate low process temperatures (179 ºC), as well. This behavior suggests that there is a limit to temperature increase with increasing plunge depth. In comparison, the optimization curve originated from Minitab Software® indicated that plunge depth did not influence the process temperature significantly when low RS and high PS are used. Hence, it is possible that the effect of plunge depth on temperature, in this OFAT analysis, is influenced by the interaction of the parameters.

Lastly, contact resistance did not show a clear trendline due to the experiment's high standard deviation, discussed in section 5.1.5. This made the property behavior challenging to analyze and did not lead to any conclusions. Nonetheless, optimization curves depicted in section 5.1.5 indicated that contact resistance is lower in welds produced with higher plunge depth.

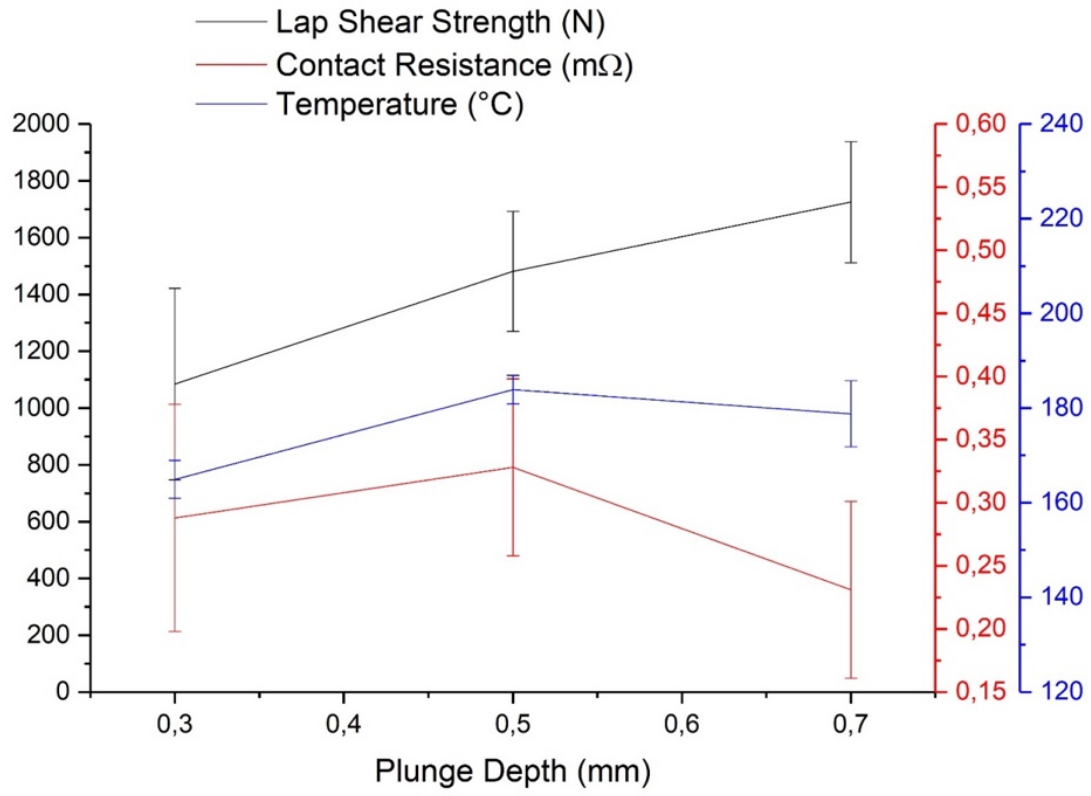

Figure 5.15 – OFAT – Plunge Depth

In Figure 5.16, it is possible to observe the properties' behavior when varying plunge speed. Differently from plunge depth, lap shear strength does not increase linearly with increasing plunge speed. Instead, the average LSS presents a peak behavior (1725 N) at 2.1 mm/s, with lower average values at higher (1474 N) or lower (1609 N) plunge speeds. This analysis suggests that if higher plunge speed values were used in the ANOVA analysis (5.1.3), it is likely that lower lap shear strength values would have been achieved with increasing PS beyond the initial process window (Table 5.4).

Regarding process temperature, the lowest temperatures (179 ºC) were achieved with 2.1 mm/s rates, while higher and lower values led to an increase of roughly 30º C. It is likely that at low plunge speeds, the material is in contact with the rotating tool for a more extended period, thus leading to high strain rates and heat input. When high plunge speeds are used, however, the material is welded in less time, which could avoid tool slippage and, therefore, increase friction and heat input. Lower process temperatures are found, hence, at intermediate plunging speeds inside the current process window. Contact resistance, however, did not vary significantly with plunge speed while presenting a high standard deviation.

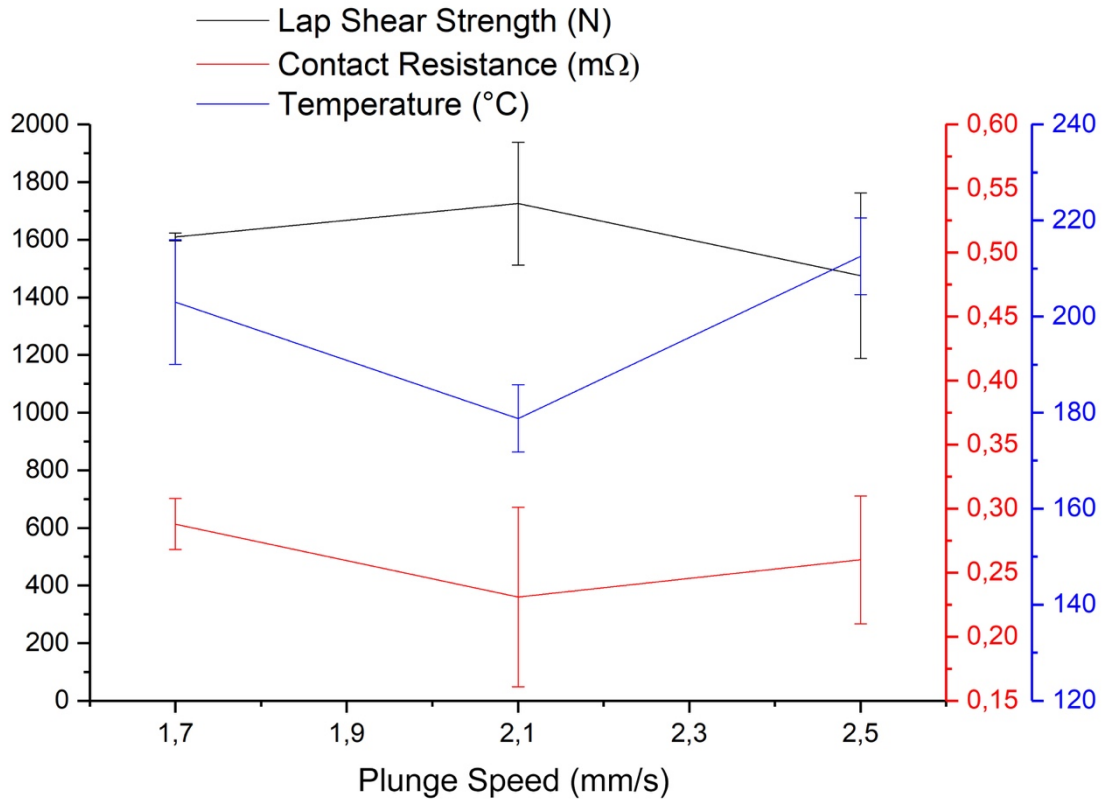

Figure 5.16 – OFAT – Plunge Speed

Figure 5.17 shows the curves regarding property measurements when varying rotational speed. Contrary to what was found in the Minitab Software® optimization analysis (section 5.1.3), lap shear strength showed to increase linearly with increasing rotational speed. However, the measured increase was from 1707 N (1100 rpm) to 1887 N (1700 rpm), indicating that rotational speed does not significantly influence the weld's mechanical properties.

Process temperature measurements indicated a behavior similar to what was found for plunge speed. Minimum temperatures occurred at the intermediate level, while higher and lower rotational speeds presented temperatures 20ºC to 25ºC higher, approximately. Since rotational speed influences the amount of material being plasticized and the occurrence of tool slippage, it appears that intermediate RS values, inside the current process window, are optimal to obtain minimum temperatures.

Regarding contact resistance, despite very high standard deviations, resistance values were significantly higher at 1700 rpm (0.372 mΩ) than at 1400

rpm (0.231 mΩ). This behavior was also found in the Minitab Software® analysis and can be attributed to metallurgical aspects that increase the electrical current's resistance through the weld. However, a secondary method for measuring CR should be used to confirm such a hypothesis.

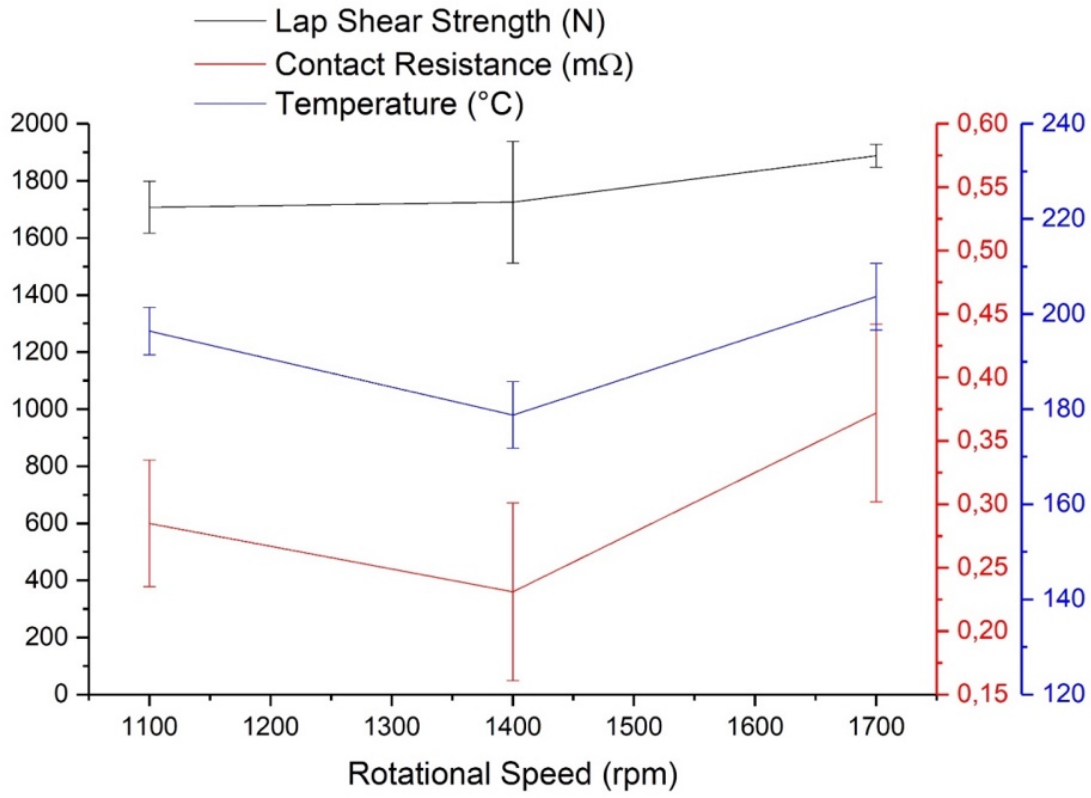

Figure 5.17 – OFAT – Rotational Speed

5.2.2 Microstructural Features

5.2.2.1 Baseline (Optimized Parameters)

Figure 5.18 represents a cross-section of a specimen welded with the baseline condition, presented in Table 5.15. The cross-section indicates three regions of interest, indexed in Figure 5.18a. Region-I is the adjustable shoulder's path; region-II is the top AA2024 sheet, and region-III is the center of the weld's cross-section. These regions will be described, followed by each process parameters' influence on the weld's microstructural features. Nonetheless, in-depth metallurgical characterization is presented in section 5.3.

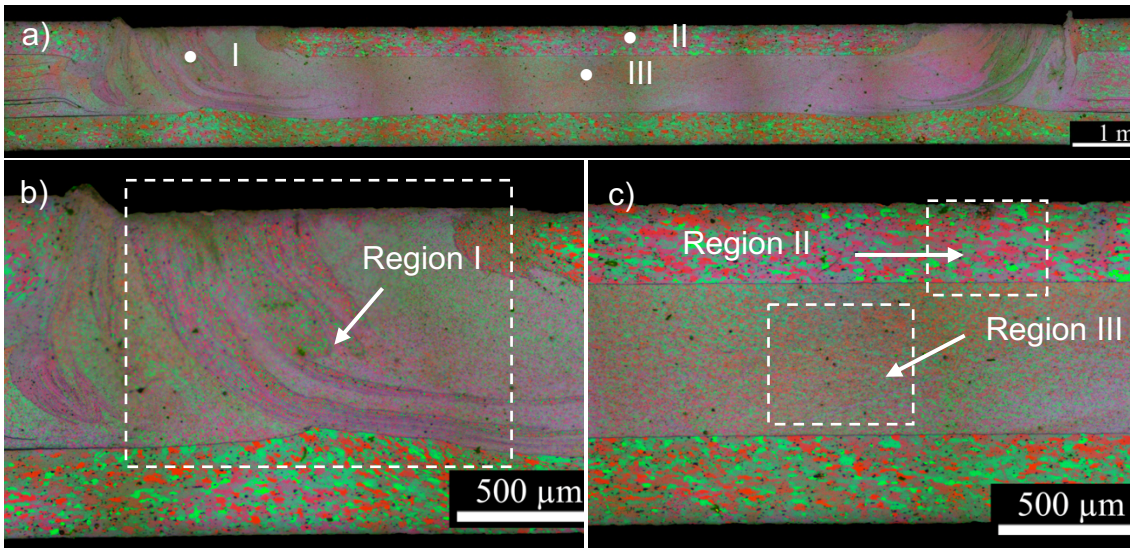

Figure 5.18 – (a) cross-section of multilayered weld processed with the baseline condition: RS=1400 rpm, PS=2.1 mm/s, and PD=0.7 mm. (b) and (c) represent higher magnifications of the cross-section at the region penetrated by the adjustable shoulder and at the center of the weld, respectively.

Region-I, delimited in Figure 5.18b, indicates the material located beneath the adjustable shoulder before welding. There are two main features in this region: a) the island of AA2024 and b) bottom sheet deformation. Regarding (a), it appears that there is AA2024 material which has been deformed during welding by the adjustable shoulder. Moreover, the material exhibits an elongated-island morphology developed due to the adjustable shoulder pushing material towards the center of the weld, followed by tool (and material) retraction. This phenomenon is further explained in section 5.3.3. Furthermore, it was found that the grains located in this region (except for the bottom AA2024 sheet) have been recrystallized and present a finer size compared to the base material (this comparison is presented in detail in section 5.3.1). Regarding (b), the bottom AA2024 sheet's deformation occurred in most welds, and its formation can be correlated to the specimen's fracture mode (section 5.4).

Region-II describes the AA2024 top sheet grains and the interface between AA2024 and CP-Al foils. It was found that in all welding conditions, the grains located in this region were similar to the grains found in the base material. This feature is explained in detail in section 5.3.3. Also, there is a clear interface between the AA2024 and CP-Al foils, indicating that diffusion bonding did not occur thoroughly in this region.

Region-III depicts the CP-Al grains in the center of the weld's cross-section and the foils' interfaces. It was also found that in all welding conditions, the CP-Al grains in this region had undergone dynamic recrystallization. In this case, since no interfaces between the CP-Al foils are visible through optical microscopic analysis, it appears that the foils have bonded properly in this weld.

5.2.2.2 Plunge Depth

Figure 5.19 is a representative cross-section of the weld produced with PD, PS, and RS of 0.3 mm, 2.1 mm/s, and 1400 rpm, respectively. In this case, region-I (Figure 5.19b) was composed of a less elongated AA2024 island. Moreover, it appears that a significant portion of this material was pushed towards outside the weld nugget, instead of towards the center of the weld (Figure 5.18b). This is due to the adjustable shoulder penetrating shorter lengths and, therefore, not forcing the AA2024 in the weld's center's direction. In addition, since the adjustable shoulder penetrated 0.3 mm, equal to the AA2024 sheet's height, part of the AA2024 top sheet material adjacent to the adjustable shoulder suffered high strain rates and was detached from the sheet.

Regarding the bottom AA2024 sheet, it appears that no significant deformation occurred due to the penetration of the adjustable shoulder. Also, gaps are found in between the bottom AA2024 and the CP-Al foils, indicating that poor mixing occurred between these materials. This feature can be correlated to the low LSS obtained in welds performed with 0.3 mm plunge depths (see 5.2.1).

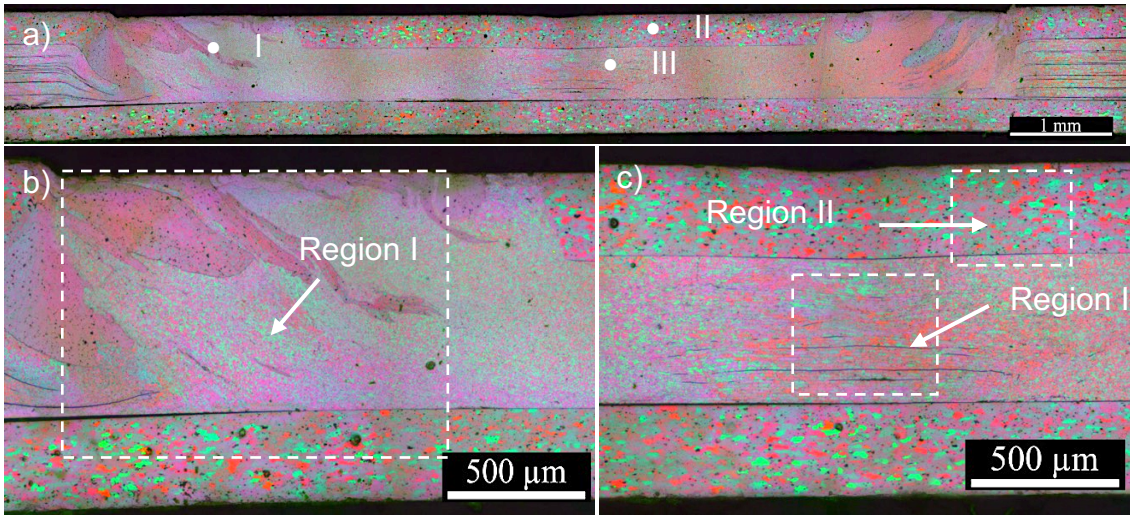

Figure 5.19 – (a) cross-section of multilayered weld processed with the baseline condition: RS=1400 rpm, PS=2.1 mm/s, and PD=0.3 mm. (b) and (c) represent higher magnifications of the cross-section at the region penetrated by the adjustable shoulder and at the center of the weld, respectively.

Regarding region-II (Figure 5.19c), it appears that insufficient material intermixing occurred between the top AA2024 sheet and the CP-Al foils, as a gap between these materials is visible. This is likely due to the low strain rates and mixing imposed by the short plunge depth.

In region-III (Figure 5.19c), it is possible to see unbonded CP-Al foils, indicating that the mixture did not occur properly amongst the CP-Al foils in the weld's center. This can also be attributed to the low strain rates imposed by using 0.3 mm plunge depth during welding. Although Figure 5.15 shows that contact resistance measurements had high standard deviations at welds with 0.3 mm plunge depths, the ANOVA and Minitab Software® optimization analysis (see Figure 5.12) indicate that low plunge depths are correlated to higher contact resistance. This is explained microstructurally with the presence of interfaces that act as barriers to the passage of electrical current.

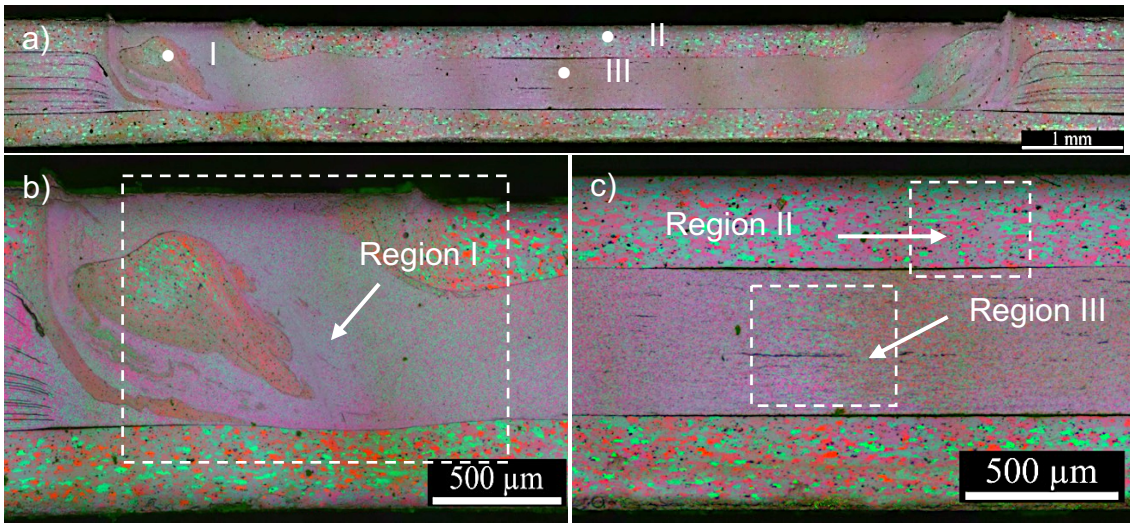

Figure 5.20 – (a) cross-section of multilayered weld processed with the baseline condition: RS=1400 rpm, PS=2.1 mm/s, and PD=0.5 mm. (b) and (c) represent higher magnifications of the cross-section at the region penetrated by the adjustable shoulder and at the center of the weld, respectively.

Figure 5.20 is a representative cross-section of the weld produced with PD, PS, and RS of 0.5 mm, 2.1 mm/s, and 1400 rpm, respectively. In this case, region-I (Figure 5.20b) demonstrated that the AA2024 material, located beneath the adjustable shoulder's path, did not return to the weld's surface upon tool retraction. It is also discernible that the AA2024 island is not as elongated as in the specimen welded with PD = 0.7 mm (see Figure 5.18) due to the adjustable

shoulder penetrating a shorter length. Regarding the bottom AA2024 sheet, it appears that penetrating 0.5 mm was sufficient to cause slight deformation (compared to the specimen welded with PD = 0.3 mm) and that such deformation increases as higher penetration depths are used. Also, gaps are still found in between the bottom AA2024 and the CP-Al foils, indicating that welding with 0.5 mm plunge depth was insufficient to produce adequate mixing between these materials. This suggests that a plunge depth minimum of 0.7 mm is required to ensure proper mixing and avoid gaps between materials that can compromise the weld's mechanical properties and contact resistance.

Regarding region-II (Figure 5.20c), it appears that a similar configuration to the specimen welded with 0.3 mm plunge depth was observed. It was found that insufficient material intermixing occurred between the top AA2024 sheet and the CP-Al foils, as a gap between these materials is visible. This is likely due to the low strain rates and mixing imposed by plunge depths lower than 0.7 mm.

In region-III (Figure 5.20c), it is possible to see unbonded CP-Al foils. This indicates that the mixture amongst CP-Al foils only occurs properly in the weld's center when 0.7 mm plunge depths are used. Therefore, the strain rates imposed by using plunge depths under 0.7 mm are insufficient to provide proper material mixing.

5.2.2.3 Plunge Speed

Figure 5.21 is a representative cross-section of the weld produced with PD, PS, and RS of 0.7 mm, 1.7 mm/s, and 1400 rpm, respectively. Regarding region-I (Figure 5.21a), it was found that at welds produced with 1.7 mm/s plunge speeds, the island of AA2024 material presented a more elongated and ramified morphology. This suggests that the mixture in this region was intensified using low plunge speeds due to the more extended period in which the tool rotated inside the weld. Moreover, the bottom AA2024 sheet also presented a more pronounced deformation than Figure 5.18, because of the more extended period under high strain rates.

In Region-II (Figure 5.21c), a gap between the top AA2024 and CP-Al foils is present, indicating insufficient material intermixing between these materials.

This suggests that although material mixing was improved in the adjustable shoulder's path, low plunge speeds do not provide a high degree of mixing homogeneously throughout the weld's cross-section.

The same analysis can be attributed to the CP-Al foils present in region-III (Figure 5.21c). It was found that the CP-Al foils in this region presented unbonded interfaces in the center of the weld. Moreover, the concentration of unbonded interfaces is higher near the top of region-III. This is likely due to material vacancies created during tool penetration, which were not filled during tool retraction due to long welding time.

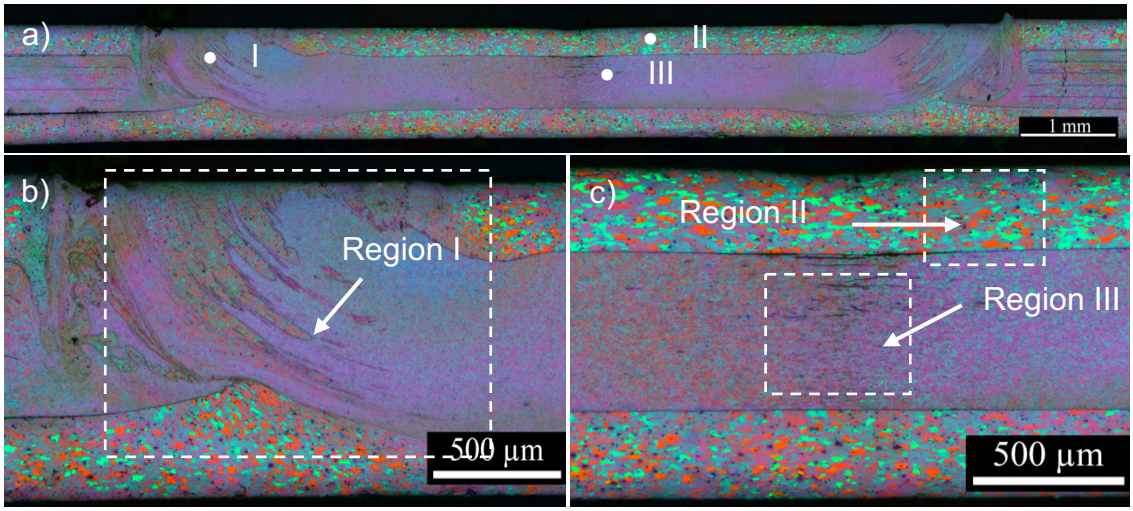

Figure 5.21 – (a) cross-section of multilayered weld processed with the baseline condition: RS=1400 rpm, PS=1.7 mm/s, and PD=0.7 mm. (b) and (c) represent higher magnifications of the cross-section at the region penetrated by the adjustable shoulder and at the center of the weld, respectively.

Figure 5.22 is a representative cross-section of the weld produced with PD, PS, and RS of 0.7 mm, 2.5 mm/s, and 1400 rpm, respectively. In region-I (Figure 5.22a), it was found that the island of AA2024 material was also ramified and elongated, suggesting that significant mixing occurred in the adjustable shoulder's path with high plunge speeds. Regarding the bottom AA2024 sheet, a significant protrusion of this material did not occur. This is indicative that high plunge speeds do not generate significant deformations in the bottom sheet due to the short welding time.

Region-II (Figure 5.22c) does not present a visible gap between the CP-Al foil and the top AA2024 sheet. Therefore, plunge speed was found to be influential in providing a bonded interface between these materials.

However, region-III (Figure 5.22c) showed that unbonded interfaces amongst the CP-Al foils are still present in welds with high plunge speeds. This suggests that the material flow provided by high plunge speeds is efficient in filling the material vacancies originated in the weld's center during tool penetration and retraction. Although, this condition's heat input is not sufficient to provide complete diffusion bonding in the CP-Al foils.

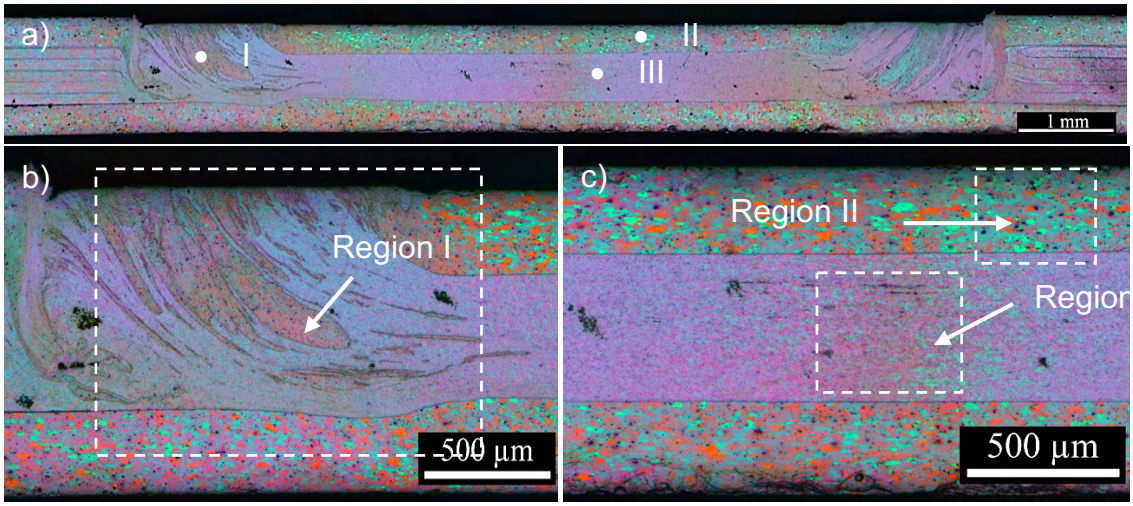

Figure 5.22 – (a) cross-section of multilayered weld processed with the baseline condition: RS=1400 rpm, PS=2.5 mm/s, and PD=0.7 mm. (b) and (c) represent higher magnifications of the cross-section at the region penetrated by the adjustable shoulder and at the center of the weld, respectively.

5.2.2.4 Rotational Speed

Figure 5.23 is a representative cross-section of the weld produced with PD, PS, and RS of 0.7 mm, 2.1 mm/s, and 1100 rpm, respectively. Regarding region-I (Figure 5.23a), it was found that mixture occurred between the AA2024 and CP-Al materials and that the island of AA2024 presents a similar morphology to the island depicted in the specimen welded with the baseline condition (see Figure 5.18). Moreover, the bottom AA2024 sheet was not significantly deformed, as it did not present a protrusion into the CP-Al foils. This indicated that low rotational speeds provide lower deformation rates in the bottom AA2024 than the baseline specimen.

Region-II (Figure 5.23c) shows that material intermixing between the top AA2024 and CP-Al foils occurred, as a gap between these materials was not visible. This suggests that low rotational speeds do not incur less material bonding at the AA2024/CP-Al interface in the center of the weld's cross-section.

Regarding region-III (Figure 5.23c), it was found that the CP-Al foils in this region presented unbonded interfaces in the center of the weld. The lack of material bonding in this region can be attributed to the low rotational speeds not providing enough mixing to fill the material vacancies at the weld's center created during tool penetration.

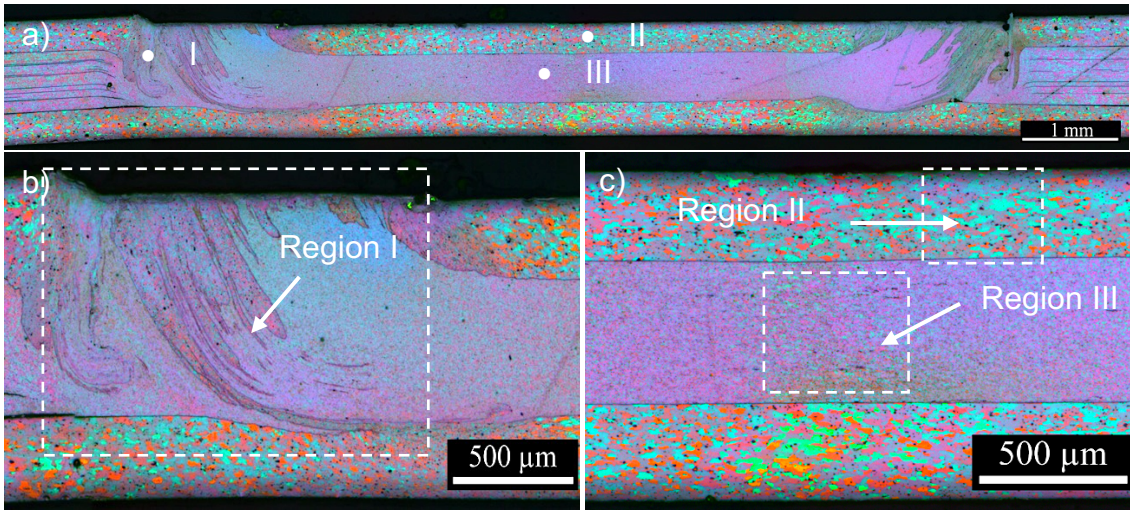

Figure 5.23 – (a) cross-section of multilayered weld processed with the baseline condition: RS=1100 rpm, PS=2.1 mm/s, and PD=0.7 mm. (b) and (c) represent higher magnifications of the cross-section at the region penetrated by the adjustable shoulder and at the center of the weld, respectively.

Figure 5.24 is a representative cross-section of the weld produced with PD, PS, and RS of 0.7 mm, 2.1 mm/s, and 1700 rpm, respectively. Regarding region-I (Figure 5.24a), it was found that mixture occurred between the AA2024 and CP-Al materials. Moreover, the use of high rotational speeds caused a significant ramification of the AA2024 material in the adjustable shoulder's path compared to samples welded with low RS (1100 rpm, Figure 5.23c) and the baseline condition (1400 rpm, Figure 5.18). The bottom AA2024 sheet was also significantly deformed, as it presented a protrusion into the CP-Al foils. This indicated that high rotational speeds provide greater strain rates in the bottom AA2024 than the baseline specimen and welds produced with low RS.

Material mixing also occurred in Region-II (Figure 5.24c), since a gap between these materials was not visible. This suggests that high rotational speeds also provide good material bonding at the AA2024/CP-Al interface in the weld's center.

Regarding region-III (Figure 5.24c), it was found that the CP-Al foils in this region did not present unbonded interfaces in the center of the weld. Therefore,

good material mixing was obtained amongst the CP-Al foils. This suggests that rotational speed is influential to such microstructural features and that higher rotational speeds provide enough material mixing to fill the material vacancies at the center of the weld created during tool penetration.

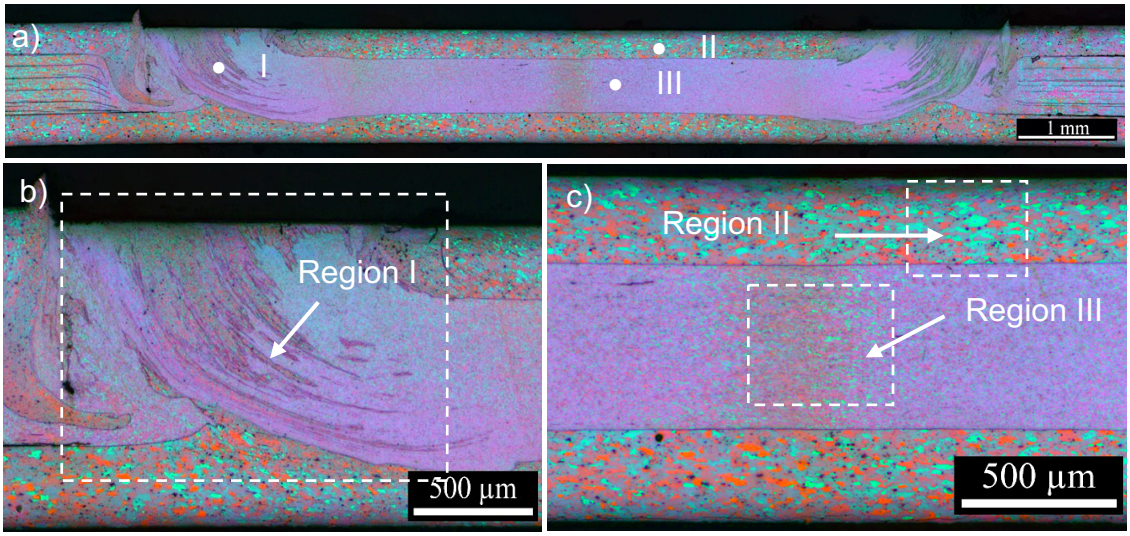

Figure 5.24 – (a) cross-section of multilayered weld processed with the baseline condition: RS=1700 rpm, PS=2.1 mm/s, and PD=0.7 mm. (b) and (c) represent higher magnifications of the cross-section at the region penetrated by the adjustable shoulder and at the center of the weld, respectively.

5.3 Metallurgical Characterization

5.3.1 Microscopy

Figure 5.25 is representative of a typical cross-section of the test specimen after joining. The weld was produced using the optimal combination of parameters and displayed a defect-free microstructure, with no lack of refill or voids present. Also, Figure 5.25 contains indications of where each tool component acts upon the material during welding.

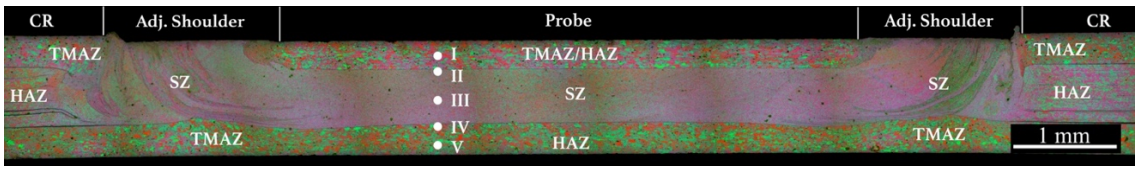

Figure 5.25 – Cross-Section of the multilayered refill FSSW weld indicating tool component placement, metallurgical zones, and the height of positions I-V.

A typical refill FSSW microstructure presents three metallurgical zones, also called regions: heat-affected zone (HAZ), thermo-mechanically affected zone (TMAZ), and stir zone (SZ). Figure 5.26 indicates the average grain size measured in the described metallurgical zones, regarding the AA2024 and

commercially pure aluminum foil. Different measurements were made for transversal and longitudinal directions, which are shown in Figure 4.1.

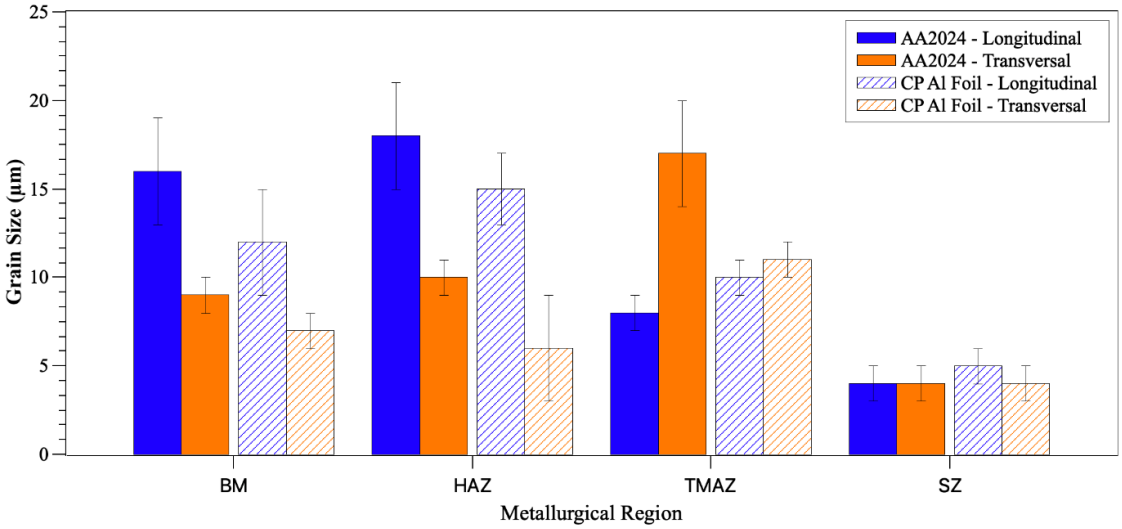

Figure 5.26 – Average grain size of the AA2024 and commercial Al foil, regarding metallurgical zones.

Regarding the base material (BM) (Figure 5.27a), the AA2024-T3 sheet and the commercial Al foils showed grain orientation due to the lamination processing route, with longitudinal and transversal average grain sizes of 16 µm ± 3 µm and 12 µm ± 3 µm, respectively. The HAZ (Figure 5.27c) is the region that experienced only high temperatures without plastic deformation; therefore, the grains in this zone suffered only dynamic recovery and, consequently, are of similar size as those encountered in the base material, as seen in Figure 5.26. The TMAZ (Figure 5.27b) undergoes moderate temperatures and strain rates and is generally located immediately outside the adjustable shoulder's path. Due to the nature of the process, which plunges the adjustable shoulder into the material, and subsequently retracts, the TMAZ grains appear bent upwards towards the adjustable shoulder's retraction. That is, having an angle of approximately 90º to the SZ equiaxed grains and the BM elongated grains. Therefore, the TMAZ is a transition region characterized by elongated grains, explaining the change in longitudinal and transversal grain sizes.

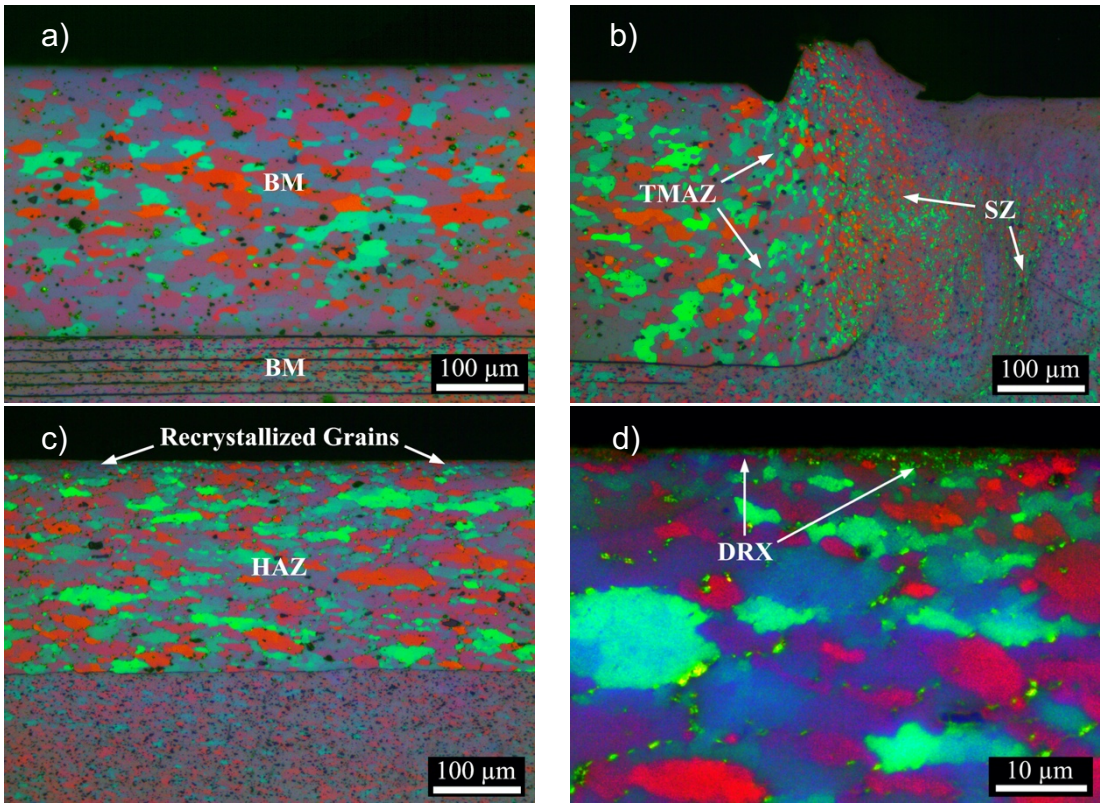

Figure 5.27 – Micrographs and metallurgical zones of the: (a) base material, (b) adjustable shoulder's path, and (c, d) center of the weld.

Lastly, the SZ (Figure 5.27b) is the weld region that suffered high strain rates and high temperatures. This combination forces the grains to dynamically recrystallize and, in doing so, obtaining equiaxed grains. Regarding the AA2024, recrystallized grains (GS = 4 µm ± 1 µm) were mainly encountered in areas penetrated by the adjustable shoulder. However, equiaxed recrystallized grains were also found in the most superficial area of the sheet in contact with the probe, as seen in Figure 5.27d. The high strain rates and the temperature obtained at this location produced a layer of recrystallized grains, approximately 10 µm thick. This behavior has already been reported in the literature, in which adiabatic heat arising from sub-interfacial (below tool material interface) contributes to the weld zone temperatures reaching 0.8 T_M, where T_M is the material's melting temperature. Consequently, DRX occurs to accommodate the high strain rates near such interface [30].

Regarding the commercial Al, the SZ was also characterized by grains with an average size of 4 μm ± 1 μm. This region was mainly encountered in areas penetrated by the adjustable shoulder, and close to the weld's center.

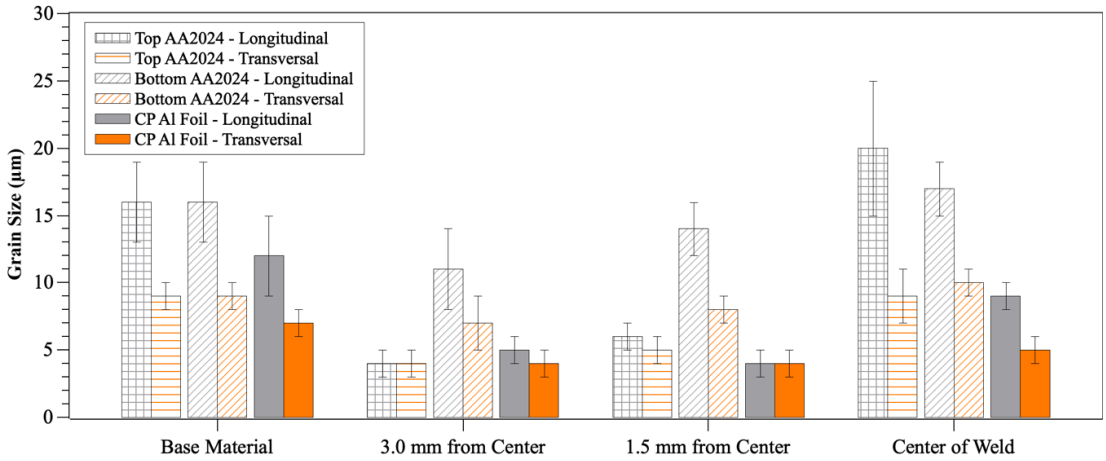

Figure 5.28 – Average grain size of the AA2024 and commercial Al foil, regarding weld locations.

Figure 5.28 refers to the average grain size of the AA2024 and commercially pure Al foil material regarding different regions of the weld. Refined equiaxed grains were not found in the AA2024 bottom sheet, and only TMAZ grains were encountered 3.0 mm from the center of the weld. Grain sizes similar to those identified in the base material were found at 1.5 mm from the weld's center, as well as in the center of the weld. Therefore, the bottom AA2024 sheet did not undergo high temperatures and strain rates to deform the grains plastically and force recrystallization.

It was found that dynamic recrystallization occurred in both materials (AA2024 top sheet, and CP-Al) at a distance of 3.0 mm and 1.5 mm from the center of the weld. Figure 5.28 shows that at precisely the weld's center, recrystallized grains were only found in the CP-Al material, while the AA2024 material was characterized by HAZ and TMAZ grains. Thermocouple

measurements were made to correlate the temperatures obtained in the weld with the grain sizes.

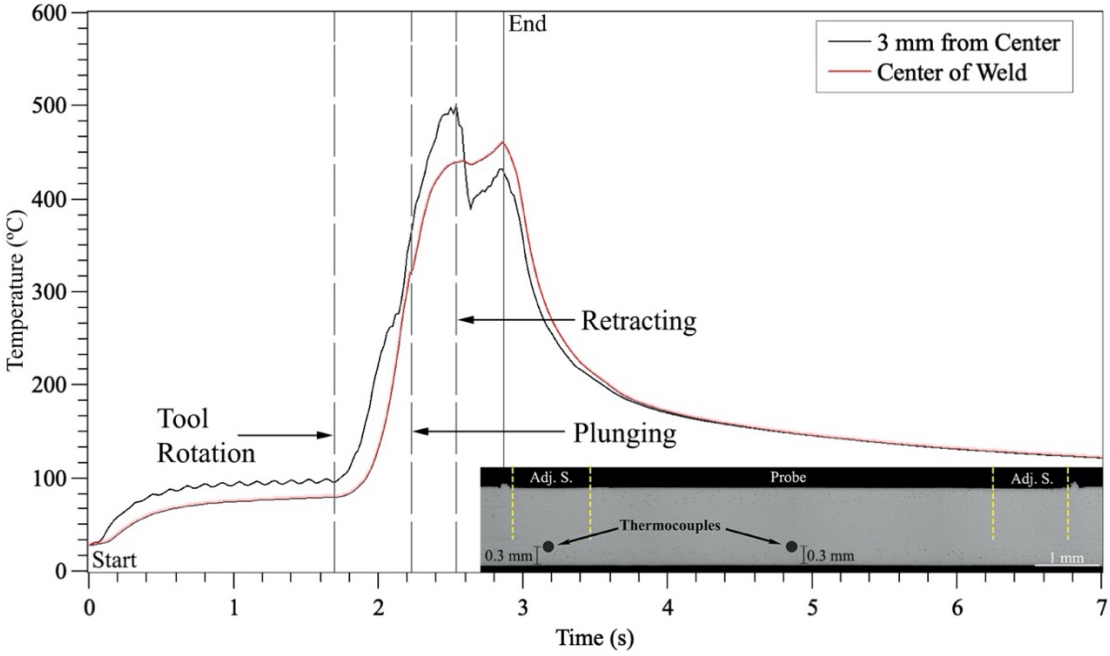

Figure 5.29 – Temperature measurements during welding at 3 mm from the center and at the center of the weld. (a) Tool initiates rotation, (b) adjustable shoulder plunges sheets, (c) adjustable shoulder retracts to initial position.

Figure 5.29 shows the temperatures measured during welding. Each step of the process is indicated, and a cross-section is attached, demonstrating the thermocouple's position. Temperatures were measured at locations distanced 3 mm from the weld's center and at precisely the weld's center. The maximum temperatures observed in the former and latter are 500ºC and 457ºC, respectively. Previous studies found that friction welded AA2024 starts experiencing dynamic recrystallization at temperatures of about 50% melting point [56]. Besides, commercially pure aluminum can dynamically recrystallize with high strain rates at temperatures below 350 ºC [57, 58]. Therefore, the temperatures reached at the adjustable shoulder trace and at the weld's center were high enough to allow dynamic recrystallization to take place in both AA2024 and commercial Al grains. This confirms that, although high temperatures were achieved, the weld's center's strain rates were insufficient to force the recrystallization of the AA2024 grains.

Scanning electron microscope (SEM) was used to analyze the microstructure in higher magnifications and to identify the phases present in each

region of the weld. Figure 5.30 contains images of the weld's center and of 1.5 mm from the center at positions I-V, indicated in Figure 5.25. Position I and V show that, in addition to the θ and S-phase particles, intergranular constituents were found at the top and bottom AA2024 sheets. This suggests that enough energy was provided to allow element segregation at the grain boundaries and phase formation. SEM and chemical analysis indicated a eutectic constituent composed of θ and S-phase. Junjun et al. [36] identified a eutectic constituent during the microstructural investigation of a refill FSSW dissimilar joint of AA5083 and copper. It was discussed that in Al-rich alloys of the Al-Cu-Mg ternary system, there are only two possibilities for a eutectic reaction [59]. At around 503 ºC, one ternary eutectic occurs in the form of Liquid ⇋ θ + (Al) + S. And at around 508 ºC, another ternary eutectic occurs in the form of Liquid ⇋ (Al) + S. However, the eutectic point of Liquid ⇋ θ + (Al) + S is higher than the measured maximum peak temperature in the center of the weld (457 ºC). This indicates that the eutectic point is lowered under the intensive plastic deformation compared to the equilibrium conditions.

Positions II and IV indicate that large intermetallic precipitates (around 10 μm) of $Al_3(Cu,Fe,Mn)$ and $Al_7Cu_2Fe_2$ were found in the top and bottom sheet at both analyzed distances. Figure 5.30b and Figure 5.30g show that the configuration of the IMCs usually consists of the $Al_7Cu_2Fe_2$ compound at the boundary of the $Al_3(Cu,Fe,Mn)$ precipitate. This is most likely due to the depletion of Mn in such region during precipitation. The formation of the IMCs found at these locations is due to the high temperatures achieved during welding, enabling atom mobility for solubilization – which, at low cooling rates, leads to the reprecipitation of the alloying elements into coarse intermetallic compounds. Positions II and IV also show that the interface between AA2024 and the commercially pure Al present better diffusion bonding further from the weld's center. This agrees with the thermal and stop-action analysis, which indicate that higher temperatures and strain rates, and, therefore, better material mixing, are found closer to the adjustable shoulder's path. Position III is also indicative of this phenomenon, as unbonded aluminum foils can be found at the center of the weld,

while at 1.5 mm from the center, no interfaces between the commercially pure Al is present.

Pos.	Center of Weld	1.5 mm from Center
I	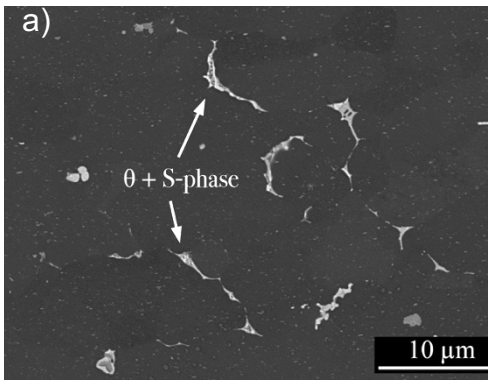	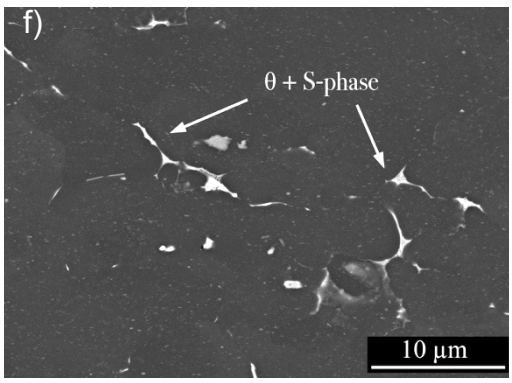
II	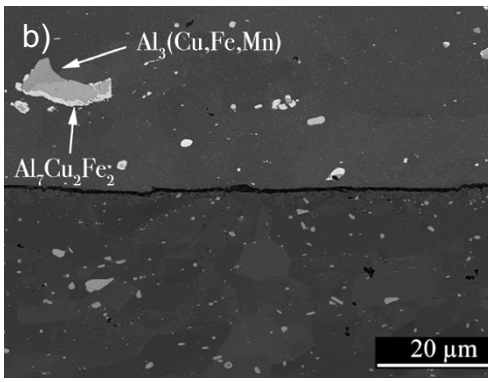	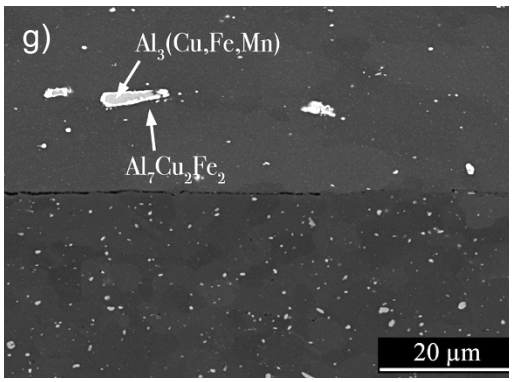
III	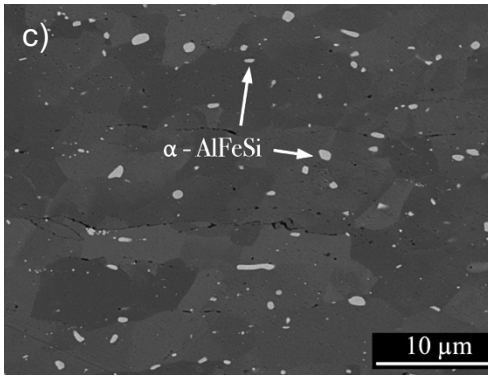	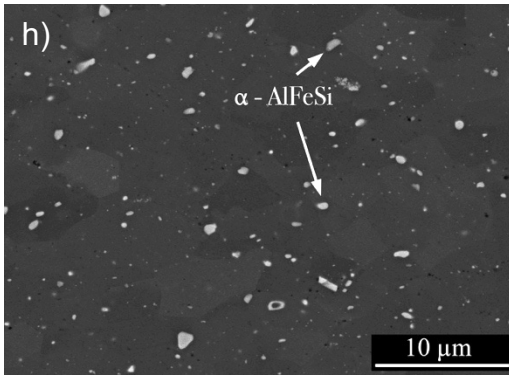
IV	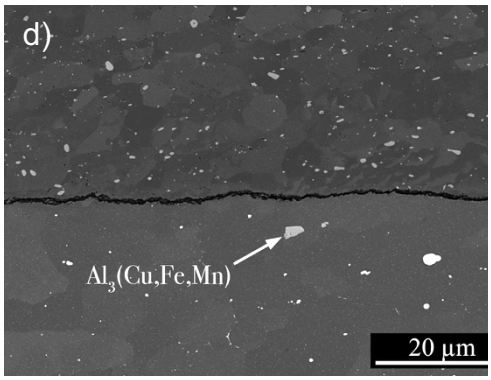	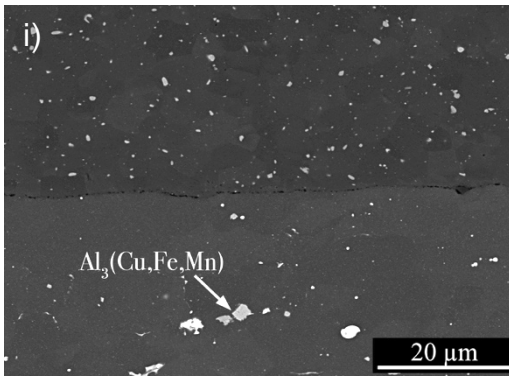

V

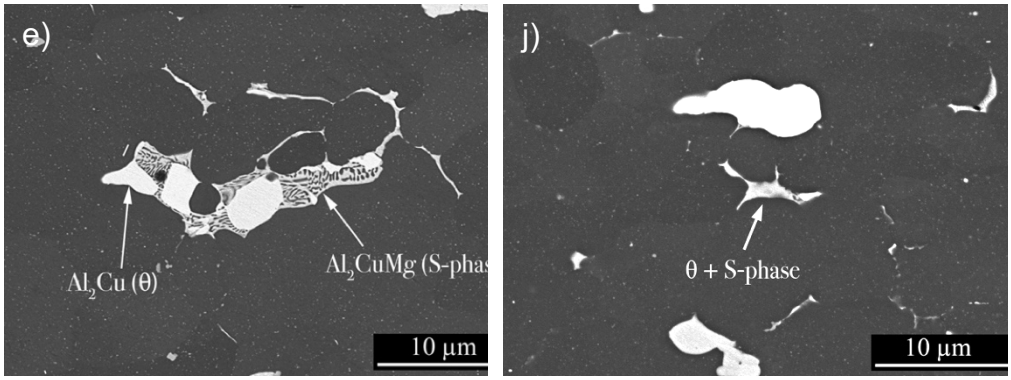

Figure 5.30 – SEM images of positions I-V of Figure 5.25 at (a – e) the weld's center and at (f – j) 1.5 mm from the center of the weld.

Figure 5.31 depicts SEM images of the adjustable shoulder's trace, that is, 3 mm from the center of the weld. Figure 5.31a indicates positions (1) – (8), observed with higher magnifications in Figure 5.31b - i, respectively. It was found that the IMCs and intergranular constituents were also present at the boundaries of recrystallized grains in the adjustable shoulder trace and, therefore, are not exclusive to the TMAZ and HAZ. This is seen in positions 1, 3, 4, 7, and 8, in which SZ grains are found.

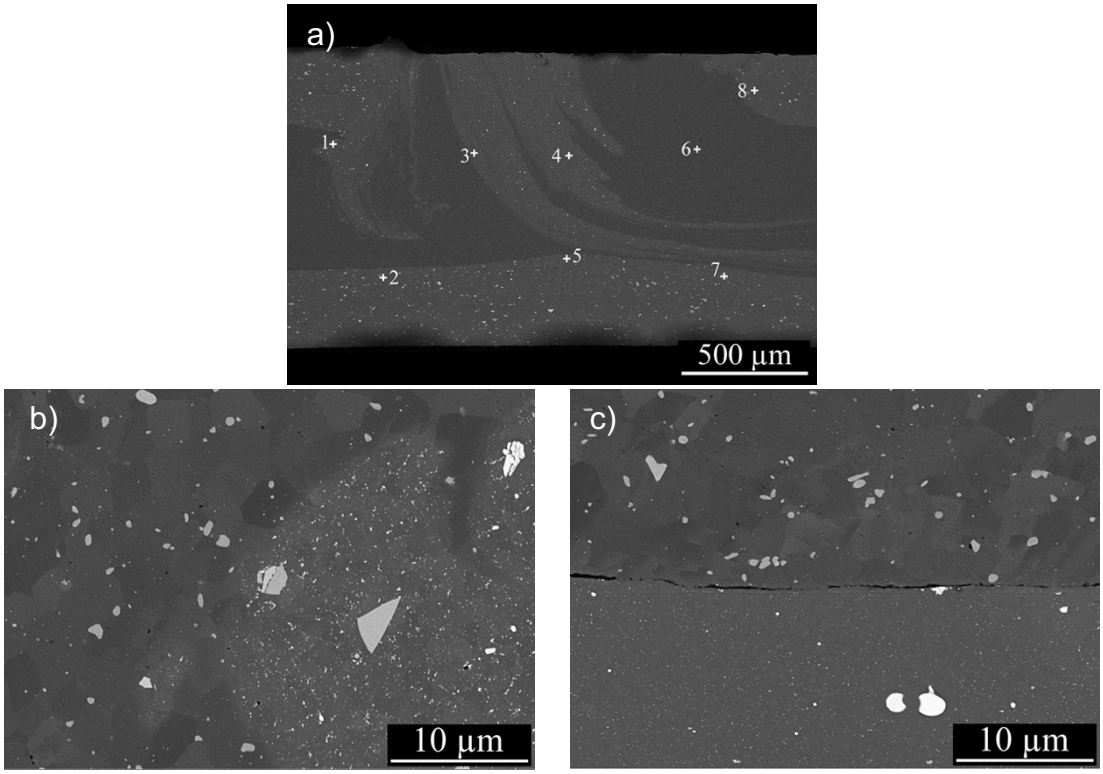

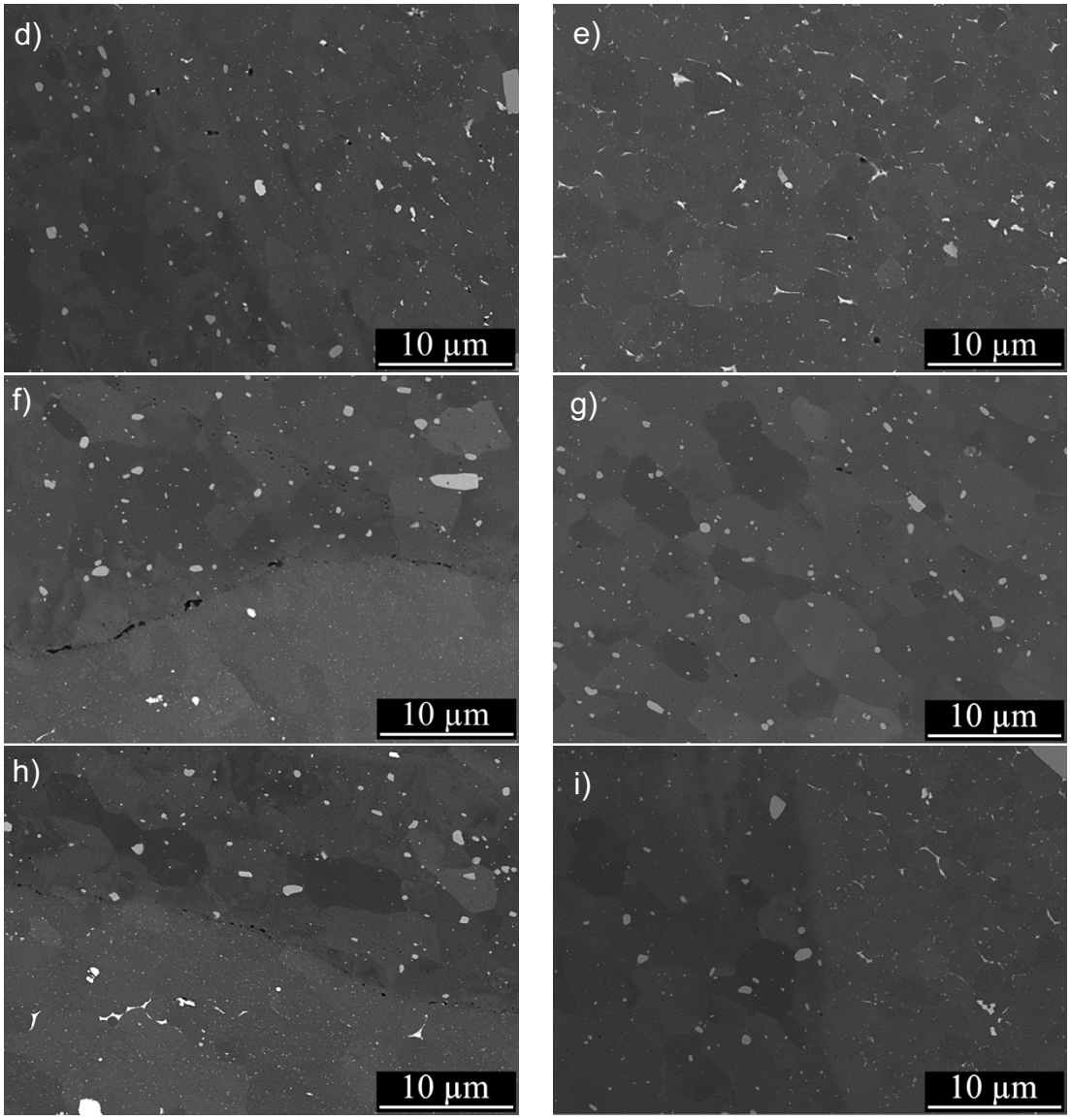

Figure 5.31 – SEM images of the adjustable shoulder's trace, that is, 3 mm from the center of the weld. Images (b) – (i) are correspondent of positions 1-8, respectively, indicated in (a).

Figure 5.32 depicts SEM images with EDS line scans at the adjustable shoulder's path. SEM and EDS analysis indicated that good material mixing occurred through atom diffusion, as the base materials showed similar concentrations of Al, Cu, and Mg. Therefore, although the weld's center presented distinct interfaces between the dissimilar materials and between the foils, good material bonding was achieved near the adjustable shoulder's path.

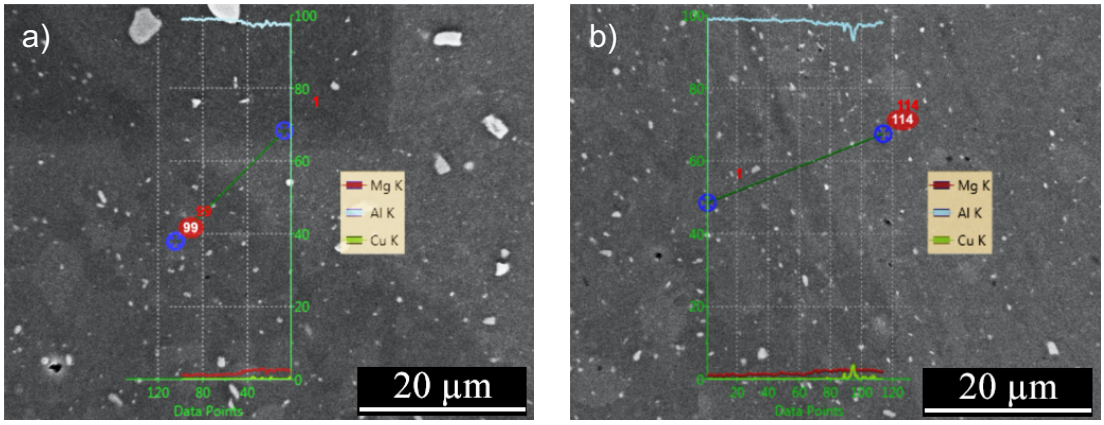

Figure 5.32 – SEM images and EDS line scans of position (a) II and (b) III at 3.0 mm from the center of the weld.

5.3.2 Microhardness

Given the metallurgical configuration presented in this study, a microhardness test was conducted to evaluate and assess each zone. Hardness profiles were conducted at different heights, specifically at the top, middle, and bottom of the weld, to fully characterize the weld's metallurgical configuration and create a complete hardness profile. A hardness profile of the optimal condition is presented in Figure 5.33 and is representative of a typical multilayered weld. It was found that the hardness of the bottom sheet does not vary significantly throughout the weld's cross-section, presenting constant hardness values close to the ones encountered in the base material (137 ± 3 $HV_{0.1}$). This is due to the similar grain sizes encountered at the bottom sheet throughout its cross-section. A slight increase was encountered in the TMAZ region below the adjustable shoulder trace, which suffered plastic deformation, as an average hardness of 146 ± 2 $HV_{0.1}$ was measured. Studies [42, 60] have shown that HAZ has a lower hardness because of grain recovery during heating, but this metallurgical region could not be discerned in the bottom sheet by such technique.

The measured base material hardness of the top AA2024 was 136 ± 3 $HV_{0.1}$. Before the adjustable shoulder trace, similar hardness measurements were found in the HAZ (135 ± 3 $HV_{0.1}$), TMAZ (139 ± 1 $HV_{0.1}$), and SZ (142 ± 3 $HV_{0.1}$). The top sheet located beneath the probe depicted hardness values with high standard deviations, showing variations of up to 18 $HV_{0.1}$. This variability is due to (1) regions that suffered hardening mechanisms, such as precipitation hardening [61], as the weld was subjected high solubility temperatures (Figure 5.29) and

low cooling rates, and the refined grains towards the sheet's surface; (2) coarser grains, IMCs and eutectic constituents that deplete the matrix of alloying elements, which reduce the average hardness [62] of the material.

The hardness profile of the middle of the weld, regarding the commercial aluminum, shows that there is an increase in the material's hardness at the center of the weld relative to the material outside the adjustable shoulder's path. This increase is due to the more refined aluminum grains obtained through recrystallization (see Figure 5.26) and to precipitation hardening by AlFeSi precipitates. A slight decrease in hardness is found at the center of the weld, which can be explained by a lower nucleation rate during recrystallization and unbonded foils (see Figure 5.30-III) due to a lack of thorough mixing. However, this cannot be confirmed since standard deviation of these measurements likely indicates hardness values of similar statistical significance.

Hardness values ranging from 40 $HV_{0.1}$ to 150 $HV_{0.1}$ were measured in the adjustable shoulder path, characterizing the transition of commercial Al to AA2024, referent to the island of copper-rich aluminum.

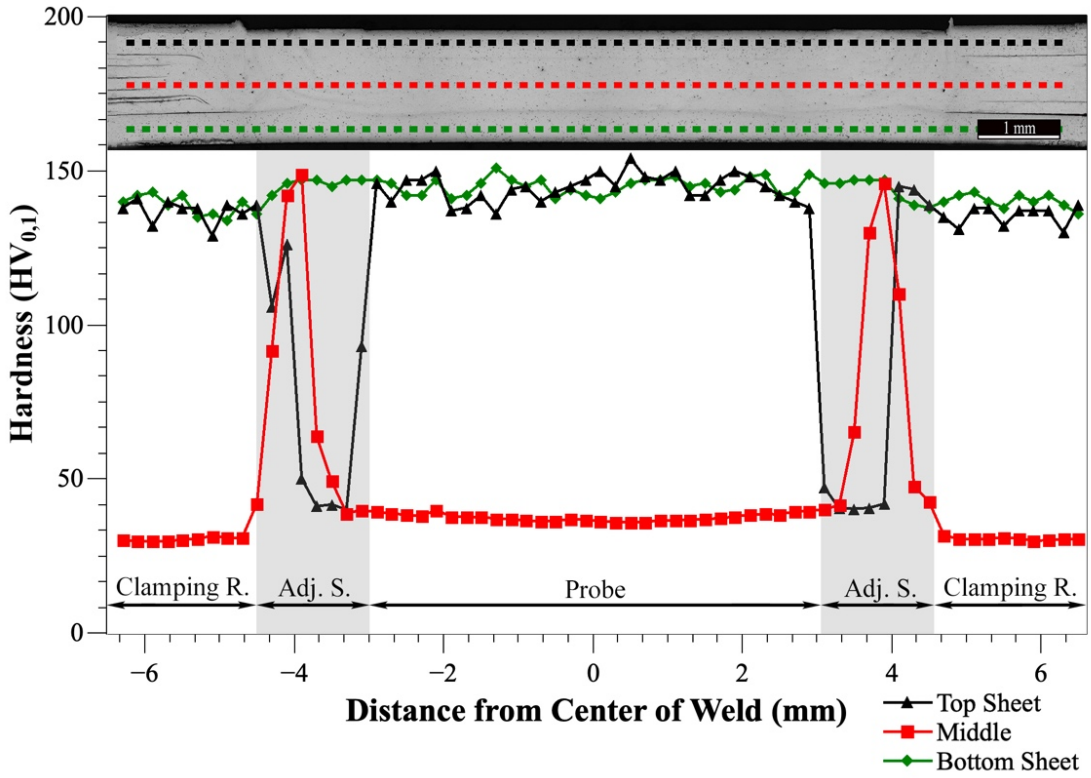

Figure 5.33 – Microhardness profile of the AA2024/Commercial Al multilayered refill FSSW weld.

5.3.3 Stop Action

The material's behavior during the process was studied through an experiment in which the welding process was stopped manually at certain moments, named *Stop Action*. In this technique, the machine was stopped when the adjustable shoulder achieved specific plunge depths, and the sample was quenched. Subsequent metallographic preparation allowed a comprehensive study of the material's flow at specific points during the process. It was decided to stop the machine when the adjustable shoulder achieved 0.3 mm, 0.5 mm, and 0.7 mm depths during plunging and then 0.5 mm and 0.3 mm during retracting. This allowed the mapping of the material's flow during all stages of the process. Since this experiment involves stopping the process manually, quenching the material, and then removing it forcibly from the machine, some samples were slightly deformed after welding.

In Figure 5.34, cross-sections of all stages of the welding process are presented. Not only is it possible to see the increase in plunge depth throughout the process, but the consequences of such action as well. Initially, when the adjustable shoulder first plunges into the material, the portion of AA2024 located beneath it is pushed downwards into the foils in the shape of an island. As the adjustable shoulder plunges more into the sheets, the island of AA2024 material distributes itself and moves more towards the weld's center. Also, the bottom sheet only starts to deform after the adjustable shoulder reaches 0.7 mm plunge depth, as was seen in the plunge depth OFAT study (see section 5.2.2.2). After the adjustable shoulder begins retracting, the island of AA2024 material is pushed back to the adjustable shoulder path due to the probe pushing downwards, returning to its initial position. This explains why the weld presents this AA2024 island with its stretched morphology in the final weld. Moreover, throughout the entire process, the top sheet remains almost intact, not mixing with the aluminum foils set beneath it. Therefore, the AA2024 top sheet shows mainly TMAZ and HAZ, with a SZ appearing only in the adjustable shoulder path.

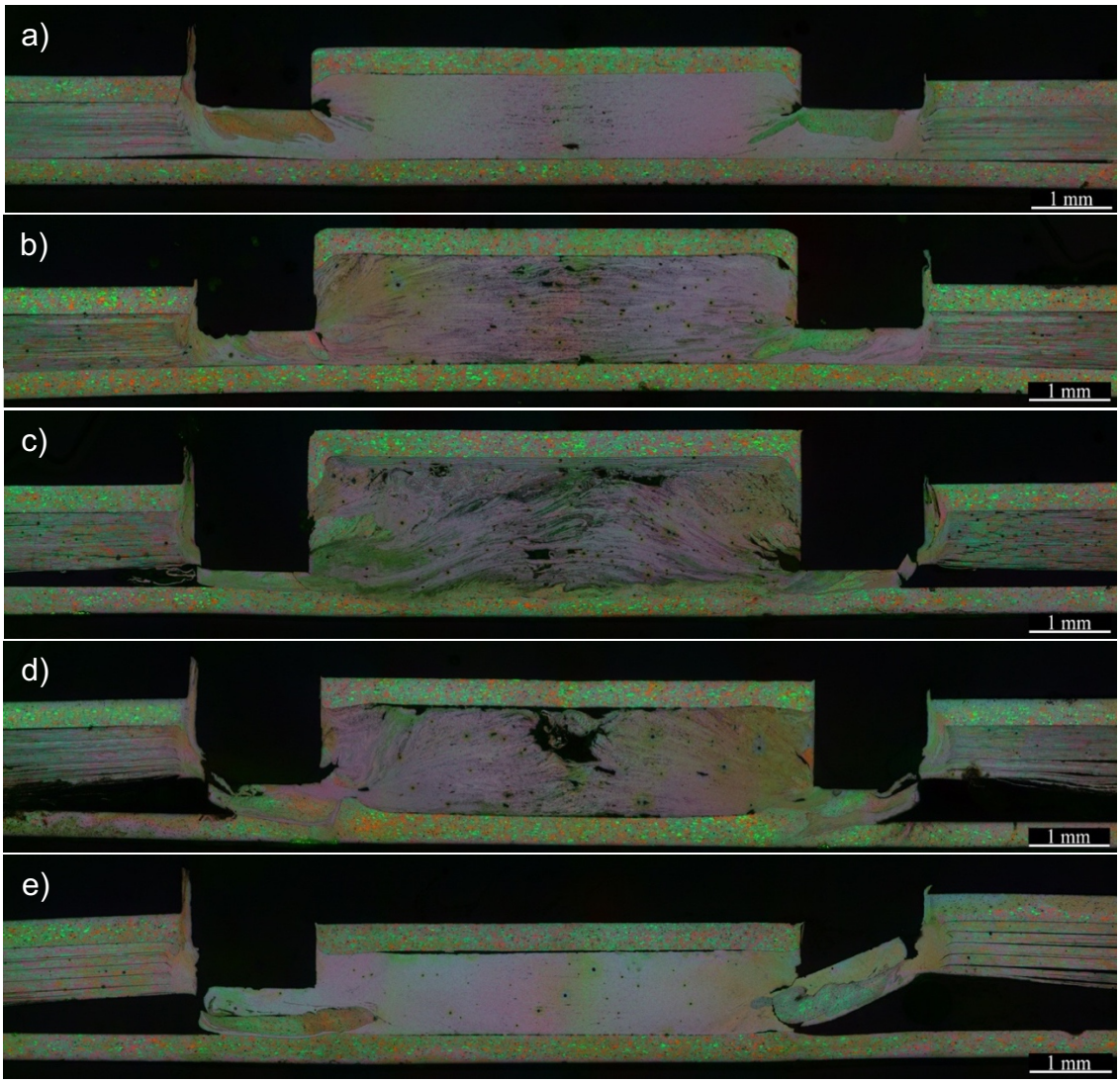

Figure 5.34 – Stop Action Cross-Sections. a) 0.3 mm plunging, b) 0.5 mm plunging, c) 0.7 mm, d) 0.5 mm retracting, e) 0.3 mm retracting

5.4 Fracture Analysis

From Figure 5.25, it can be seen that the multilayered joint possesses several transitions from unbonded interfaces to the stir zone due to the presence of many aluminum foils. This characteristic is similar to the hook feature in typical refill FSSW welds, which is generally influential in the joint's overall mechanical strength [39, 60, 63]. However, regarding the multilayered weld studied in this work, fracture analysis showed that the crack only propagated at two sites: either at the top or bottom sheet. In the top sheet, the crack initiates between the AA2024 and the first aluminum foil and propagates at the weld's outer rim, resembling an eyebrow (see Figure 5.35). In the bottom sheet, the crack initiates

at the interface between the AA2024 and the commercial aluminum and propagates through-the-weld (TTW) (see Figure 5.35b).

The eyebrow pull-out fracture mode occurred in 85% of all tested specimens in which processing parameters were varied. Figure 5.35 suggests that the crack opens outside the weld nugget and propagates through the AA2024 island in an upward and circumferential direction. This behavior is due to two effects: increased hardness at the stir zone and secondary bending (SB). Initially, the crack attempts to propagate through the weld, but as it encounters the AA2024 island, it follows the interface between the commercial aluminum and the AA2024 as it is the path of less resistance. Due to the nature of lap shear testing, secondary bending occurs to align the sheets and, therefore, potentially influences failure mode [64, 65]. Both mechanisms can be seen in Figure 5.35b, in which the top left of the weld shows a crack bending upwards (propagating through the Al/AA2024 interface), and the bottom sheet is plastically bent in the function of secondary bending.

The through-the-weld fracture mode was seen in 15% of all cases, specifically in samples welded with 0.3 mm plunging depths. The lower sheet's detachment is due to low diffusion bonding and lack of mechanical interlocking at the bottom region of the weld, as the adjustable shoulder did not plunge deep enough into the weld to promote atomic diffusion and plastically deform the bottom AA2024 sheet (see section 5.2.2.2). The TTW fracture mode does not appear in the test specimens welded with plunge depth greater than 0.3 mm, due to better diffusion bonding in the lower sheet in welds with higher plunge depths. This also explains why the specimens welded with 0.3 mm plunge depth have lower LSS, despite having similar metallurgical features to welds produced with other processing parameters. For such reason, the improved material mixing with 0.7 mm plunge depths granted a more significant resistive section to the propagation of the crack, as the CP-Al/AA2024 interface becomes more consolidated, resulting in lap shear strength up to 1900 N.

Moreover, Figure 5.14 indicates that lap shear strength does not vary significantly among test specimens fractured by eyebrow pull-out. This suggests that multilayered welds' mechanical strength is strongly correlated to the

mechanical interlocking of the bottom sheet with the commercial aluminum, which appeared in welds produced with high plunge depth. Besides, it was concluded that the unbonded interfaces encountered in the commercial aluminum at the center of the weld nugget in all specimens did not interfere in the joint's mechanical properties. The same is said for the IMCs and eutectic constituents in the AA2024 sheets, which either act as stress concentrators or fragilize the grain boundaries, thus lowering the material's mechanical properties. Since the crack propagates at the outer circumference, these compounds and constituents do not interfere with the fracture mode.

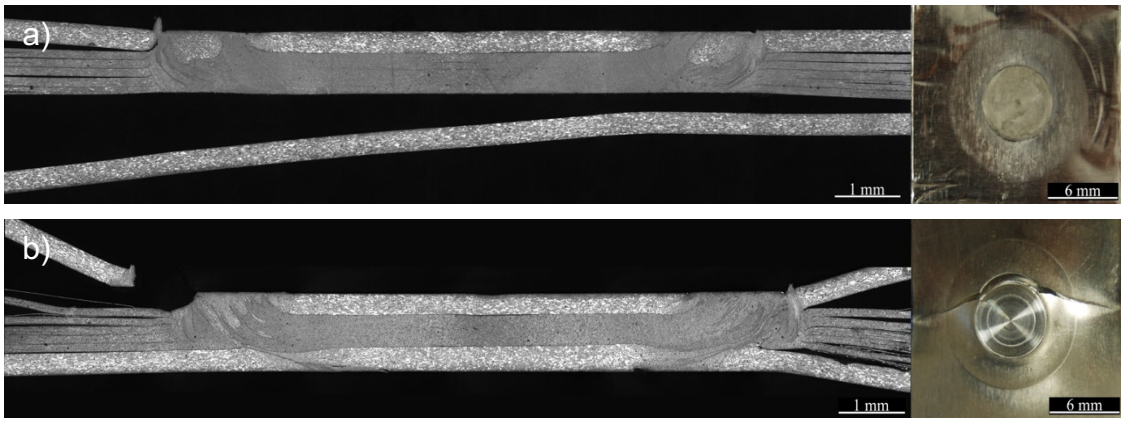

Figure 5.35 – Example of a tested lap shear specimen surfaces and cross-sections of the fractured welds showing (a, c) eyebrow pull-out and (b, d) bottom sheet through-the-weld fracture.

5.5 Process Comparison

Many other processes are currently being used for welding and joining multilayered aluminum and copper alloys to a conducting tab in battery pouches. The process differs from one car manufacturer to another, but, in general, ultrasonic, laser, and resistance spot welding are used. Other techniques such as bolting and wires are also used, but since these add mass to the pouch, they will not be considered for comparison.

The results of the work conducted by Brand et. al [18], explained in detail in section 3.1, are summarized in Figure 5.36 and compared to the lap shear strength, process temperature, and contact resistance results obtained in this work. However, an asterisk (*) was indicated in refill FSSW due to the differences in property measurement methods used by Brand et al. [18] and by the author of this work. An analysis of the differences in the properties of welds produced by LBW, USW, and RSW was made in section 3.1.

Regarding ultimate tensile strength, it is not possible to make a fair and direct comparison amongst the obtained values since the specimen used for lap shear testing in his work was not multi-layered and had a different thickness from the one used in this project. Also, it is not possible to directly compare the electrical resistances with RFSSW, since the techniques used for measuring such property were different.

Nonetheless, the process temperature measurements can be compared, for they were all taken using infra-red cameras where the output was the maximum temperature achieved during welding. Therefore, it was observed that the temperature reach during refill FSSW was much greater than ultrasonic welding, which presented the second-highest maximum temperature. However, the temperature at the cell terminal, where the weld is produced, is not of great concern since it does not contact the electrochemically active materials. In contrast to the cylinder barrel's temperature, which must maintain below 80ºC to avoid compromising such materials. It was impossible to obtain the temperature at the cylinder barrel in this project since no welds were produced in batteries. However, from the thermal images shown in Figure 5.8, it was noticed that high temperatures were limited to the area near the spot weld, and that, depending on the process parameters, at 30 mm from the weld, the temperatures were below 80ºC.

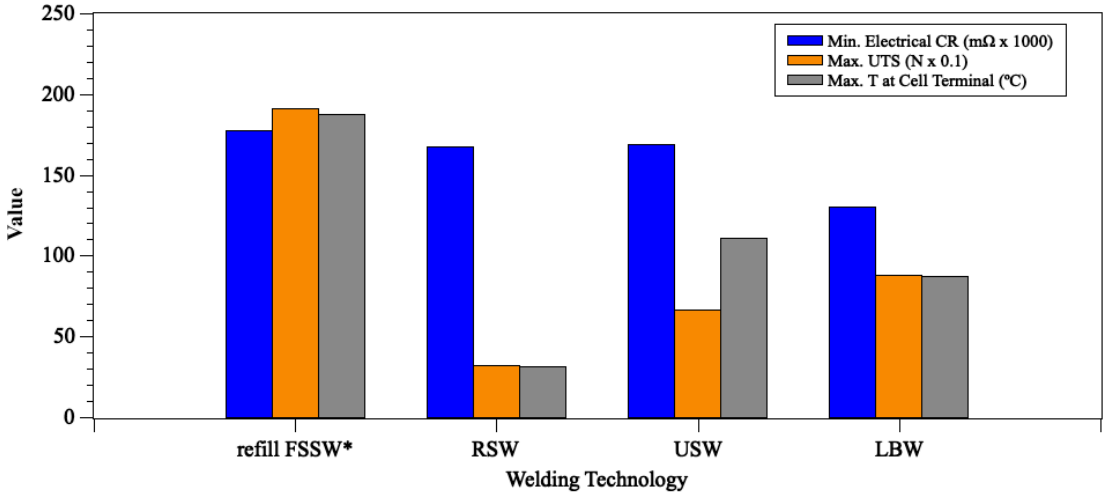

Figure 5.36 – Mechanical, thermal, and electrical properties from different welding techniques.

Regarding contact resistance, values similar to those obtained in ultrasonic, resistance, and laser welding were found for refill FSSW. Therefore, it was

demonstrated that refill FSSW is suitable for obtaining welds with contact resistance values acceptable to the battery manufacturing industry.

5.5.1 Cost analysis

Table 5.17 presents the main costs associated with the welding technologies generally used in battery manufacturing.

Table 5.17 – The main costs of resistance-, laser-, ultrasonic-, refill FSS welding.

Welding Technology	Main Costs
RSW	▪ Electricity ▪ Inert environment in the form of gas ▪ Connection bands (material) ▪ Welding Equipment
LBW	▪ Equipment generating laser beam ▪ Robotics operating the laser
USW	▪ Energy ▪ Welding Equipment ▪ Tool condition monitoring (TCM)
Refill FSSW	▪ Energy ▪ Welding Equipment ▪ Tool replacement

Regarding RSW, the most basic costs are the power source and welding equipment, making this technology advantageous to the alternative techniques currently used in battery manufacturing. Moreover, automation and semi-automation have shown to provide significant cost benefits through an overall reduction of energy consumption and less wear on the electrodes[66].

LBW can be cost-prohibitive for some manufacturers due to the high initial investment costs, such as obtaining equipment for generating the laser beam and the robotics needed for automation. Therefore, for this method to become profitable, a large production scale is required [67, 68]. A study comparing the assembly costs of LBW and RSW has found that, albeit the laser equipment's complexity has diminished, LBW is still very expensive. In part, this is due to the equipment's sensitivity, making transportation, before installation, more challenging than for RSW. Nonetheless, LBW is exceptionally efficient, and the

progress of technological development makes it possible for laser processes to compete economically in large scale industrial areas.

USW has shown two main economic advantages over the welding methods currently used for battery manufacturing: lower energy consumption and production cost. USW also provides major benefits to the welding process, such as good mechanical properties, surface quality, and reduced tool wear. In addition, USW can include a tool condition monitoring (TCM) system that can monitor equipment wear and further ensure battery weld quality and a reduction of production costs [13]. Therefore, the absence of this system may sacrifice useful tool lives and increase costs [69].

Refill FSSW presents a cost structure similar to USW, in which the main costs are the welding equipment, energy consumption, and the three-piece welding tool. This technique can also be automated by investing in a mechanical structure. Refill FSSW, therefore, presents many of the advantages of good mechanical properties, suitable contact resistance, low energy consumption, and relatively inexpensive equipment. However, studies have shown that the refill FSSW tool conditions alter significantly with an increasing number of welds. Specifically, the adjustable shoulder component was identified as the most stressed part of the tool, indicating significant wear with increasing welds, which influences the mechanical properties of the resulting weld [70]. This may be an issue if large scale welding is needed. However, further investigation is still required to assess the best tool material for welding to obtain prolonged tool life and consistent mechanical properties and surface quality throughout hundreds and thousands of welds.

Lastly, labor costs are also present in every welding technology and represent a significant percentage of the total production costs. Although labor costs vary due to each technology's different qualification requirements, they are also reduced with increasing automation and minimized stops during production. However, as a result of automation, weld quality suffers variation and can effectively harm production profits [71, 72].

6 CONCLUSIONS

In this work, mechanical properties, electrical resistance, heat input, and microstructural features of a multilayered AA2024-T3/CP-Al weld produced by refill FSSW were investigated for its applicability in battery manufacturing. The weld's microstructure was correlated to the process parameters and the evaluated properties. The analysis produced the following observations:

1. It was possible to optimize the process parameters, varying plunge depth, rotational speed, and plunge speed, through the Box-Behnken statistical methodology, to obtain the highest lap shear strength with lowest contact resistance and heat input. The optimized combination of parameters is PD = 0.7 mm, RS = 1400 rpm, and PS = 2.1 mm/s.
2. Through response surface methodology, it was found that PS significantly influences the mechanical properties of the weld, and that PS and PD are influential to the process temperature. No significant correlation was found between contact resistance and processing parameters for the process window used in this work.
3. OFAT analysis showed that PD, PS, and RS are influential to the morphology of the AA2024 island in the adjustable shoulder's path, the bottom sheet's deformation in the middle of the adjustable shoulder's path, and to the presence of unbonded interfaces in the center of the weld.
4. Microstructural analysis depicted intermetallic compounds, eutectic constituents, and unbonded foils in the center of the weld; however, fracture mode analysis showed that these features were not detrimental to mechanical properties since the crack propagates at the weld's outer circumference.
5. Lap shear strength testing indicated mechanical properties superior to aerospace application requisites in all studied welding conditions. Therefore, this technique was able to provide multilayered welds with mechanical strength sufficient to battery joints.
6. Lastly, the infrared analysis showed that temperatures below 80 ºC could be achieved 16s after welding at 30 mm from the welding tool. Therefore,

cell degradation can be avoided if the welding tool is placed at a significant distance from electrochemically active material.

This work has demonstrated that refill FSSW successfully welds the multilayered materials presented and has great potential for its use in battery manufacturing. Therefore, this study is a standpoint for future works which aim to either analyze other multilayered welding configurations or to further assess the use of refill FSSW directly in batteries.

7 FUTURE WORK SUGGESTIONS

This work aimed to analyze the feasibility of using refill FSSW technology for welding multilayered foils in pouch-type battery manufacturing. However, due to the lack of publications regarding multilayered welds and refill FSSW, it was necessary to assess the possibility of a multilayered weld and analyze the material's behavior during a refill FSSW weld with multiple layers and how this behavior influences the weld's properties. Therefore, this work was limited to one novel configuration – 50 foils of commercially pure aluminum between two AA2024 sheets – for a complete characterization of a multilayered weld. Since the number of foils and the materials used in battery manufacturing generally vary, the following are suggestions for future work:

1. Weld different multilayered materials – Common materials used as highly conductive surfaces in battery manufacturing are commercial-grade pure Al (1100) and commercial grade pure Cu (CDA 110) [6]. Therefore, an investigation of welding multilayered copper through refill FSSW is suggested.
2. Weld different amounts of layers – Common battery pouches have between 10 to 100 foils welded to a conducting tab. Therefore, it is suggested to investigate the material's behavior if more than 50 foils are welded (for both commercial-grade Al and Cu) and the influence of welding thicker or thinner sheets on the weld's properties.
3. Perform a refill FSSW on a sample battery – Since this work aims to analyze the feasibility of using refill FSSW in battery manufacturing, it is convenient to investigate the result and consequences of performing such weld in a sample battery. Important properties to this application, such as process temperature and contact resistance, should also be measured.

8 REFERENCES

1. Kelly JC, Sullivan JL, Burnham A, Elgowainy A (2015) Impacts of Vehicle Weight Reduction via Material Substitution on Life-Cycle Greenhouse Gas Emissions. Environ Sci Technol 49:12535–12542. https://doi.org/10.1021/acs.est.5b03192
2. Guarnieri M (2011) When Cars Went Electric. IEEE Ind Electron Mag 5:61–62. https://doi.org/10.1109/MIE.2011.940248
3. Matulka R (2014) The History of the Electric Car | Department of Energy. Dep Energy. https://doi.org/10.1049/ip-a-1.1985.0014
4. Mahmoudzadeh Andwari A, Pesiridis A, Rajoo S, et al (2017) A review of Battery Electric Vehicle technology and readiness levels. Renew Sustain Energy Rev 78:414–430. https://doi.org/10.1016/j.rser.2017.03.138
5. Sanyo (2016) Types of Battery Cells; Cylindrical Cell, Button Cell, Pouch Cell. In: Batter. Univ. http://batteryuniversity.com/learn/article/types_of_battery_cells. Accessed 20 Jul 2018
6. Cai W, Kang B, Hu SJ, et al (2017) Analysis of Li-Ion Battery Joining Technologies
7. Larsson H, Chamberlain A, Walin S, et al (2019) Welding methods for electrical connections in battery systems
8. Lee SS, Kim TH, Hu SJ, et al (2010) Joining Technologies for Automotive Lithium-Ion Battery Manufacturing: A Review. ASME 2010 Int Manuf Sci Eng Conf Vol 1 541–549. https://doi.org/10.1115/MSEC2010-34168
9. Rosendo T, Tier M, Mazzaferro J, et al (2015) Mechanical performance of AA6181 refill friction spot welds under Lap shear tensile loading. Fatigue Fract Eng Mater Struct 38:1443–1455. https://doi.org/10.1111/ffe.12312
10. Amancio-Filho ST, Camillo APC, Bergmann L, et al (2011) Preliminary Investigation of the Microstructure and Mechanical Behaviour of 2024 Aluminium Alloy Friction Spot Welds. Mater Trans 52:985–991. https://doi.org/10.2320/matertrans.L-MZ201126
11. Plaine AH, Suhuddin UFH, Alcântara NG, dos Santos JF (2017) Microstructure and mechanical behavior of friction spot welded AA6181-

T4/Ti6Al4V dissimilar joints. Int J Adv Manuf Technol 92:3703–3714. https://doi.org/10.1007/s00170-017-0439-2

12. Yong JY, Ramachandaramurthy VK, Tan KM, Mithulananthan N (2015) A review on the state-of-the-art technologies of electric vehicle, its impacts and prospects. Renew Sustain Energy Rev 49:365–385. https://doi.org/10.1016/j.rser.2015.04.130
13. Lee SS, Kim TH, Hu SJ, et al (2010) Joining technologies for automotive lithium-ion battery manufacturing - A review. ASME 2010 Int Manuf Sci Eng Conf MSEC 2010 1:541–549. https://doi.org/10.1115/MSEC2010-34168
14. Kang B, Cai W, Tan CA (2013) Dynamic response of battery tabs under ultrasonic welding. J Manuf Sci Eng Trans ASME 135:1–12. https://doi.org/10.1115/1.4024535
15. Laser Beam Welding - Equipment, Principle, Working with Advantages and Disadvantages - The Welding Master. https://www.theweldingmaster.com/laser-beam-welding/. Accessed 28 Feb 2020
16. What is Spot Welding? - TWI. https://www.twi-global.com/technical-knowledge/faqs/what-is-spot-welding. Accessed 28 Feb 2020
17. Song Q, Zhang W, Bay N (2005) An Experimental Study Determines the Electrical Contact Resistance in Resistance Welding. Suppl To Weld J
18. Brand MJ, Schmidt PA, Zaeh MF, Jossen A (2015) Welding techniques for battery cells and resulting electrical contact resistances. J Energy Storage 1:7–14. https://doi.org/10.1016/j.est.2015.04.001
19. Brand M, Gläser S, Geder J, et al (2013) Electrical safety of commercial Li-ion cells based on NMC and NCA technology compared to LFP technology. World Electr Veh J 6:572–580. https://doi.org/10.1109/EVS.2013.6914893
20. Hamedi M, Atashparva M (2017) A review of electrical contact resistance modeling in resistance spot welding. Weld World 61:269–290. https://doi.org/10.1007/s40194-016-0419-4
21. Test Tooling Solution - Study of Probe Pin Internal Resistance. https://tts-grp.com/our-company/milestones/15-library/technical-paper/402-study-of-probe-pin-internal-resistance. Accessed 20 Oct 2020

22. Ott R (1967) Thermal and electrical resistance of metal contacts. Dissertations and Theses
23. Aydin H, Bayram A, Uğuz A, Akay KS (2009) Tensile properties of friction stir welded joints of 2024 aluminum alloys in different heat-treated-state. Mater Des 30:2211–2221. https://doi.org/10.1016/j.matdes.2008.08.034
24. Perović M, Baloš S, Kozak D, et al (2017) Utjecaj kinematičkih faktora zavarivanja trenjem miješanjem na karakteristike zavarenog spoja kovanih ploča od legure aluminija EN AW 7049 A. Teh Vjesn 24:723–728. https://doi.org/10.17559/TV-20160417122830
25. Reimann M, Goebel J, Gartner TM, Jorge F (2017) Refilling termination hole in AA 2198 – T851 by refill friction stir spot welding. J Mater Process Tech 245:157–166. https://doi.org/10.1016/j.jmatprotec.2017.02.025
26. Suhuddin UFH, Fischer V, Kostka A, dos Santos JF (2017) Microstructure evolution in refill friction stir spot weld of a dissimilar Al–Mg alloy to Zn-coated steel. Sci Technol Weld Join 22:658–665. https://doi.org/10.1080/13621718.2017.1300744
27. Davis JR (2001) Aluminum and Aluminum Alloys. Light Met Alloy 66. https://doi.org/10.1361/autb2001p351
28. Kaiser Aluminum (2014) Aluminum Alloy 2024. https://www.unitedaluminum.com/united-aluminum-alloy-2024/. Accessed 19 Jul 2018
29. 2024-T3 Aluminum :: MakeItFrom.com. https://www.makeitfrom.com/material-properties/2024-T3-Aluminum. Accessed 19 Jul 2018
30. Da Silva AAM, Dos Santos JF, Rosendo TR, et al (2007) Performance evaluation of 2-mm thick alclad AA2024 T3 aluminium alloy friction spot welding. SAE Tech Pap. https://doi.org/10.4271/2007-01-3812
31. Suhuddin U, Fischer V, dos Santos J (2013) Formation of Intermetallic Compounds in Dissimilar Friction Spot Weld of Al to Mg Alloys. Mater Sci Forum 765:731–735. https://doi.org/10.4028/www.scientific.net/MSF.765.731
32. Plaine AH, Gonzalez AR, Suhuddin UFH, et al (2015) The optimization of

friction spot welding process parameters in AA6181-T4 and Ti6Al4V dissimilar joints. Mater Des 83:36–41. https://doi.org/10.1016/j.matdes.2015.05.082

33. Pieta G, Dos Santos J, Strohaecker TR, Clarke T (2014) Optimization of friction spot welding process parameters for AA2198-T8 sheets. Mater Manuf Process 29:934–940. https://doi.org/10.1080/10426914.2013.811727
34. Santana LM, Suhuddin UFH, Ölscher MH, et al (2017) Process optimization and microstructure analysis in refill friction stir spot welding of 3-mm-thick Al-Mg-Si aluminum alloy. Int J Adv Manuf Technol 92:4213–4220. https://doi.org/10.1007/s00170-017-0432-9
35. Effertz PS, Quintino L, Infante V (2017) The optimization of process parameters for friction spot welded 7050-T76 aluminium alloy using a Taguchi orthogonal array. Int J Adv Manuf Technol 91:3683–3695. https://doi.org/10.1007/s00170-017-0048-0
36. Shen J, Suhuddin UFH, Cardillo MEB, Dos Santos JF (2014) Eutectic structures in friction spot welding joint of aluminum alloy to copper. Appl Phys Lett 104:2014–2017. https://doi.org/10.1063/1.4876238
37. Shen J, Lage SBM, Suhuddin UFH, et al (2017) Texture Development and Material Flow Behavior During Refill Friction Stir Spot Welding of AlMgSc. Metall Mater Trans A 49:241–254. https://doi.org/10.1007/s11661-017-4381-6
38. Cai W, Lee S, Hu SJ Introduction. In: Ultrasonic Welding of Lithium-Ion Batteries. ASME Press
39. Campanelli LC, Suhuddin UFH, Antonialli AÍS, et al (2013) Metallurgy and mechanical performance of AZ31 magnesium alloy friction spot welds. J Mater Process Technol 213:515–521. https://doi.org/10.1016/j.jmatprotec.2012.11.002
40. Vacchi GS, Plaine AH, Silva R, et al (2017) Effect of friction spot welding (FSpW) on the surface corrosion behavior of overlapping AA6181-T4/Ti-6Al-4V joints. Mater Des 131:127–134. https://doi.org/10.1016/j.matdes.2017.06.005

41. Plaine AH, Suhuddin UFH, Alcântara NG, dos Santos JF (2016) Fatigue behavior of friction spot welds in lap shear specimens of AA5754 and Ti6Al4V alloys. Int J Fatigue 91:149–157. https://doi.org/10.1016/j.ijfatigue.2016.06.005
42. Suhuddin U, Fischer V, Kroeff F, dos Santos JF (2014) Microstructure and mechanical properties of friction spot welds of dissimilar AA5754 Al and AZ31 Mg alloys. Mater Sci Eng A 590:384–389. https://doi.org/10.1016/j.msea.2013.10.057
43. Suhuddin U, Fischer V, dos Santos JF (2016) Microstructure in dissimilar friction spot weld of A1 to Mg alloys observed by stop-action technique. Frict Stir Weld Process VII 263–270. https://doi.org/10.1007/978-3-319-48108-1_27
44. Khuri AI, Mukhopadhyay S (2010) Response surface methodology. Wiley Interdiscip Rev Comput Stat 2:128–149. https://doi.org/10.1002/wics.73
45. Box GEP, Draper NR (2008) Response Surfaces, Mixtures, and Ridge Analyses, Second Edi. John Wiley & Sons, Inc., Hoboken, New Jersey, Hoboken, New Jersey
46. Hussein SH, Alzaidi M, Hasan QO (2016) A Statistical Approach for Modelling of Lightweight Palm Oil Clinker Reinforced Concrete Beams with Openings. 5:3390–3397
47. Ferreira SLC, Bruns RE, Ferreira HS, et al (2007) Box-Behnken design: An alternative for the optimization of analytical methods. Anal. Chim. Acta 597:179–186
48. Gann JA, Winston AW (1927) Magnesium and Its Alloys
49. Montgomery DC (1984) Design and Analysis of Experiments Eighth Edition
50. Boag A, Hughes AE, Wilson NC, et al (2009) How complex is the microstructure of AA2024-T3? Corros Sci 51:1565–1568. https://doi.org/10.1016/j.corsci.2009.05.001
51. Tier M, Rosendo T, Olea CW, et al (2008) The influence of weld microstructure on mechanical properties of refill friction spot welding of 5042 aluminium alloy. 7th Int Symp Frict Stir Weld 20–22
52. Tier MD, Rosendo TS, Dos Santos JF, et al (2013) The influence of refill

FSSW parameters on the microstructure and shear strength of 5042 aluminium welds. J Mater Process Technol 213:997–1005. https://doi.org/10.1016/j.jmatprotec.2012.12.009

53. American Welding Society (2013) AWS D17.2 - Specification for Resistance Welding for Aerospace Applications
54. Plaine AH, Suhuddin UFH, Afonso CRM, et al (2016) Interface formation and properties of friction spot welded joints of AA5754 and Ti6Al4V alloys. Mater Des 93:224–231. https://doi.org/10.1016/j.matdes.2015.12.170
55. Su P, Gerlich A, North TH, Bendzsak GJ (2006) Energy utilisation and generation during friction stir spot welding. Sci Technol Weld Join. https://doi.org/10.1179/174329306X84373
56. Davis JR (1993) ASM Specialty Handbook: Aluminum and Aluminum Alloys. ASM Int. https://doi.org/10.1017/CBO9781107415324.004
57. Belyayev SP, Likhachev VA, Myshlyayev MM, Sen'kov ON (1981) Dynamic Recrystallization of Aluminium. Phys Met Metallogr 52:143–152
58. Rajat K. Roy, Additional (2016) Recrystallization. Intech i:79–98. https://doi.org/http://dx.doi.org/10.5772/58385
59. Günter Effenberg, Alan Prince , Nathalie Lebrun, Hans Leo Lukas MGH (2005) Al-Cu-Mg (Aluminium - Copper - Magnesium). 1–32. https://doi.org/10.1007/10915967_4
60. Suhuddin U, Campanelli L, Bissolatti M, et al (2013) A review on microstructural and mechanical properties of friction spot welds in Al-based similar and dissimilar joints. Proc 1st Int Jt Symp Join Weld 15–21. https://doi.org/10.1533/978-1-78242-164-1.15
61. Siqueira ML, da Silva A, de Lourdes Noronha Motta Melo M, Rodrigues G (2019) Mechanical Properties Analysis of Al2024 alloy Submitted to Different Aging Time and different Cold Plastic Deformation degree. Mater Res 22:. https://doi.org/10.1590/1980-5373-MR-2018-0598
62. Staley JT, E.A. Starke J, R.E. Sanders J, et al Aluminum Alloys - Contemporary research and Applications. Academic Press, Inc.
63. Rosendo T, Parra B, Tier MAD, et al (2011) Mechanical and microstructural investigation of friction spot welded AA6181-T4 aluminium alloy. Mater Des

32:1094–1100. https://doi.org/10.1016/j.matdes.2010.11.017

64. Ekh J, Schön J, Melin LG (2005) Secondary bending in multi fastener, composite-to-aluminium single shear lap joints. Compos Part B Eng 36:195–208. https://doi.org/10.1016/j.compositesb.2004.09.001
65. Ekh J, Schön J (2005) Effect of secondary bending on strength prediction of composite, single shear lap joints. Compos Sci Technol 65:953–965. https://doi.org/10.1016/j.compscitech.2004.10.020
66. Petrov PY, Alekseev I V., Kolesnik EA (2017) Economic evaluation for use of advanced welding equipment. In: IOP Conference Series: Earth and Environmental Science
67. Should your operation convert from spot welding to laser keyhole welding? https://www.thefabricator.com/thefabricator/article/laserwelding/should-your-operation-convert-from-spot-welding-to-laser-keyhole-welding-. Accessed 30 Sep 2020
68. High degree of automation of the laser welding machine - Knowledge - Wuhan HGLaser Engineering Co., Ltd. https://www.hgtech-laser.com/info/high-degree-of-automation-of-the-laser-welding-27812013.html. Accessed 30 Sep 2020
69. Kumar S, Wu CS, Padhy GK, Ding W (2017) Application of ultrasonic vibrations in welding and metal processing: A status review. J. Manuf. Process.
70. Montag T, Wulfsberg JP, Hameister H, Marschner R (2014) Influence of tool wear on quality criteria for refill friction stir spot welding (RFSSW) process. In: Procedia CIRP
71. Jou M (2003) Real time monitoring weld quality of resistance spot welding for the fabrication of sheet metal assemblies. J Mater Process Technol. https://doi.org/10.1016/S0924-0136(02)00409-0
72. Ambroziak A, Korzeniowski M (2010) Using resistance spot welding for joining aluminium elements in automotive industry. Arch Civ Mech Eng. https://doi.org/10.1016/s1644-9665(12)60126-5

APPENDIX A

Weld	RS (rpm)	PD (mm)	Plun./Retrac. Time (s)	WF (kN)	WT(s)	Note
6	1500	0.5	1	7.2	2.0	Good surface, no bonding to the backing
7	1500	0.5	0.8	7.2	1.6	Good surface, no bonding to the backing
8	1500	0.5	0.5	7.2	1.0	Good surface, no bonding to the backing
9	1500	0.5	0.3	7.2	0.6	Good surface, no bonding to the backing
10	1500	0.5	0.15	7.2	0.3	Good surface, no bonding to the backing, materials twisted
11	1500	0.5	0.15	8.2	0.3	Good surface, no bonding to the backing, materials twisted.
12	1600	0.5	0.15	9.2	0.3	Good surface, no bonding to the backing, materials twisted.
13	1700	0.5	0.15	9.2	0.3	Good surface, no bonding to the backing
14	1700	0.5	0.15	10	0.3	Good surface, no bonding to the backing

APPENDIX B

Note: The acronym "PR" refers to the definition of *Plunge Rate*, which is equivalent Plunge Speed.

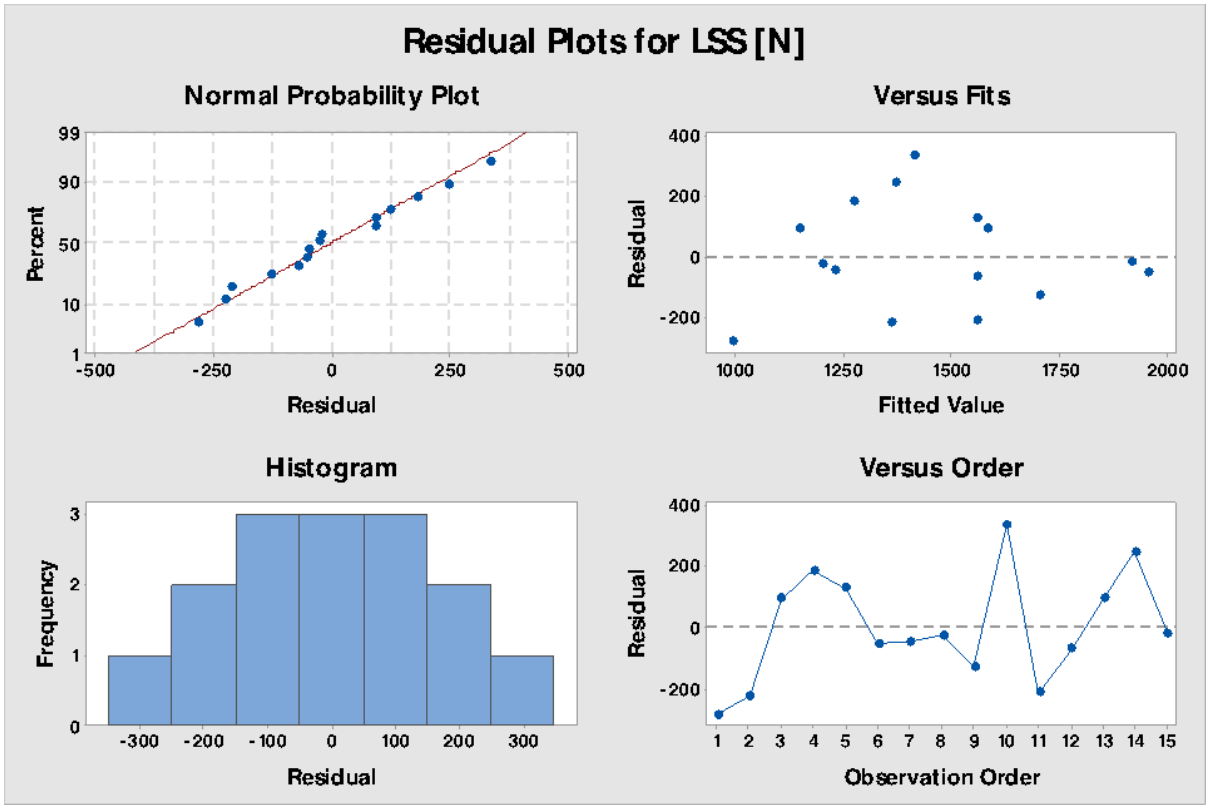

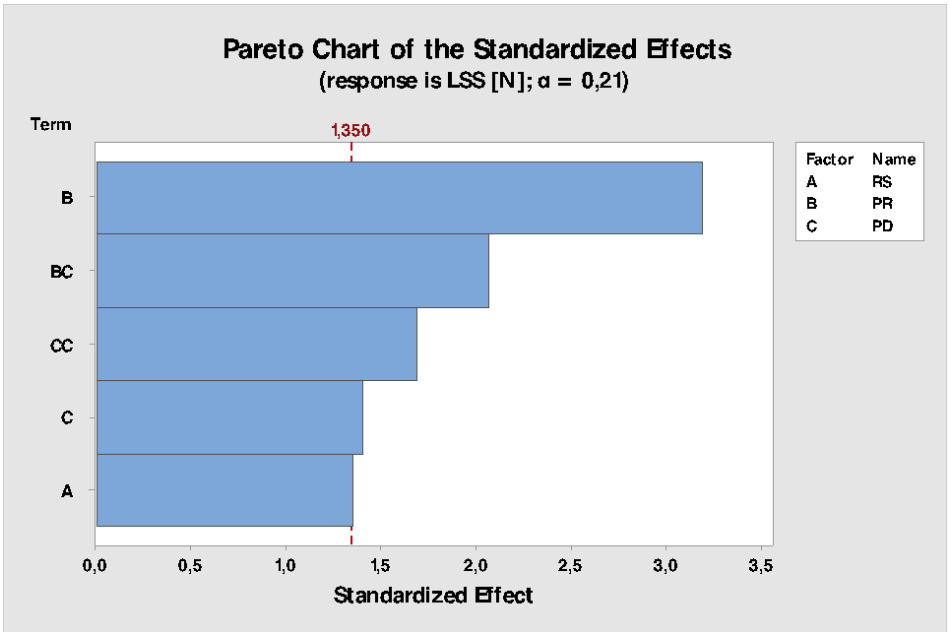

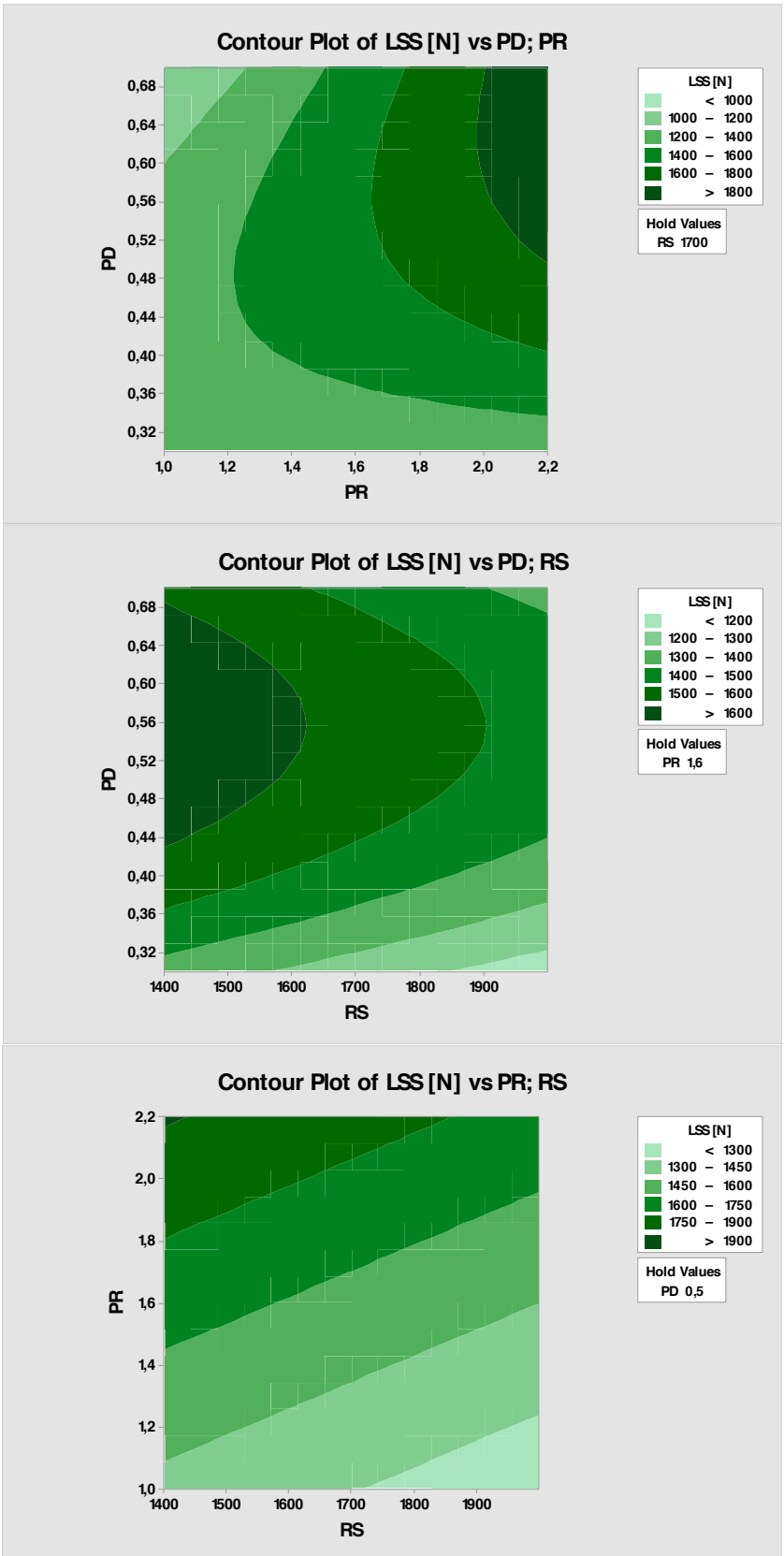
Contour Plot of LSS [N] vs PD; PR
PD
PR
0,68
0,64
0,60
0,56
0,52
0,48
0,44
0,40
0,36
0,32
1,0
1,2
1,4
1,6
1,8
2,0
2,2
LSS [N]
< 1000
1000 – 1200
1200 – 1400
1400 – 1600
1600 – 1800
> 1800
Hold Values
RS 1700
Contour Plot of LSS [N] vs PD; RS
PD
RS
0,68
0,64
0,60
0,56
0,52
0,48
0,44
0,40
0,36
0,32
1400
1500
1600
1700
1800
1900
LSS [N]
< 1200
1200 – 1300
1300 – 1400
1400 – 1500
1500 – 1600
> 1600
Hold Values
PR 1,6
Contour Plot of LSS [N] vs PR; RS
PR
RS
2,2
2,0
1,8
1,6
1,4
1,2
1,0
1400
1500
1600
1700
1800
1900
LSS [N]
< 1300
1300 – 1450
1450 – 1600
1600 – 1750
1750 – 1900
> 1900
Hold Values
PD 0,5

APPENDIX C

Note: The acronym "PR" refers to the definition of *Plunge Rate*, which is equivalent Plunge Speed.

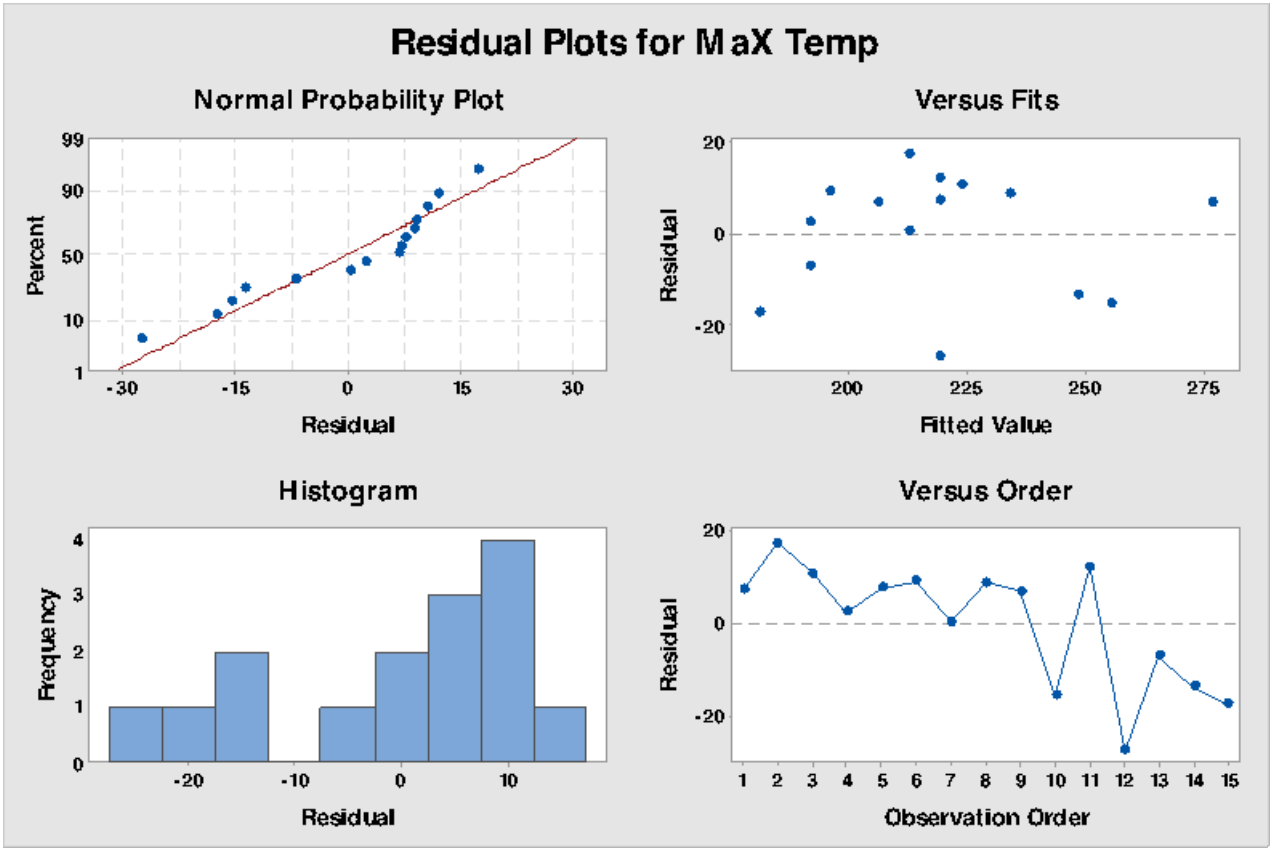

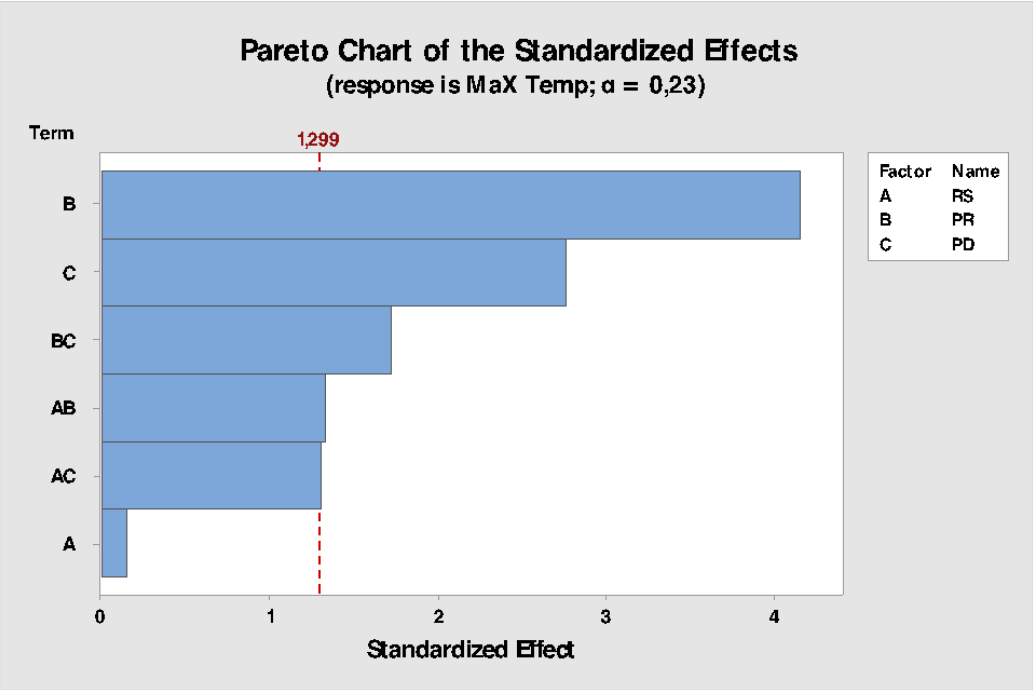
Pareto Chart of the Standardized Effects
(response is MaX Temp; α = 0,23)
Term
1,299
B
C
BC
AB
AC
A
0
1
2
3
4
Standardized Effect
Factor Name
A RS
B PR
C PD

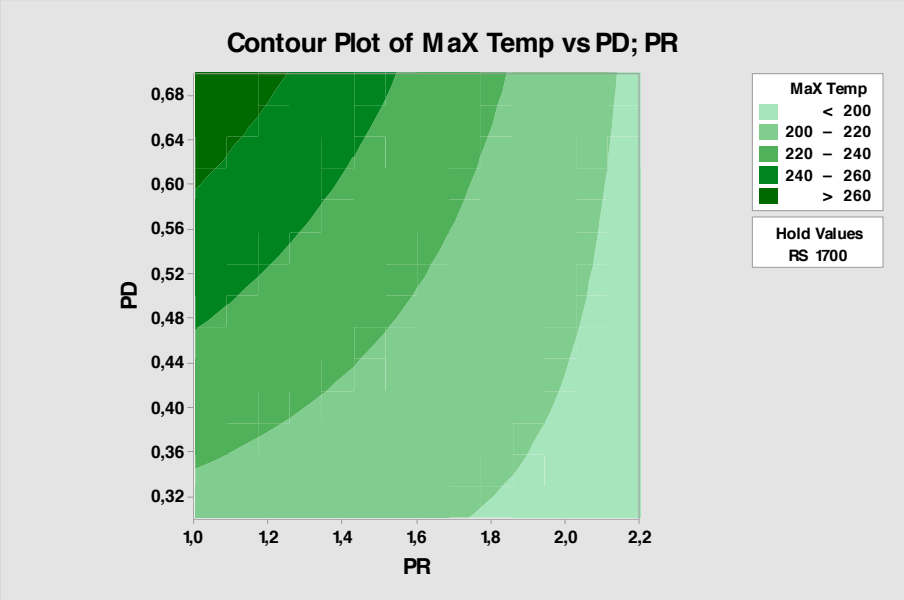
Contour Plot of MaX Temp vs PD; PR
PD
0,68
0,64
0,60
0,56
0,52
0,48
0,44
0,40
0,36
0,32
1,0
1,2
1,4
1,6
1,8
2,0
2,2
PR
MaX Temp
< 200
200 – 220
220 – 240
240 – 260
> 260
Hold Values
RS 1700

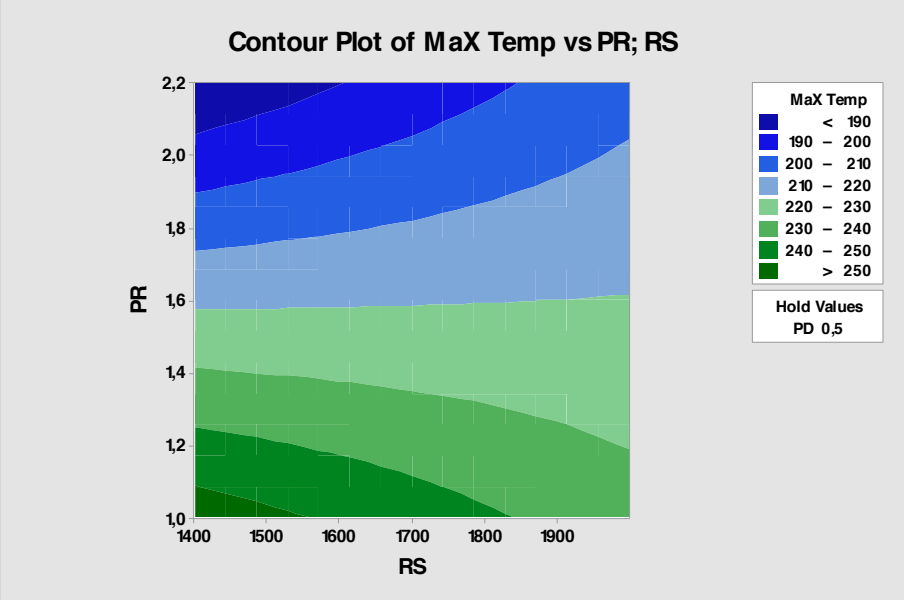
Contour Plot of MaX Temp vs PR; RS
PR
2,2
2,0
1,8
1,6
1,4
1,2
1,0
1400
1500
1600
1700
1800
1900
RS
MaX Temp
< 190
190 – 200
200 – 210
210 – 220
220 – 230
230 – 240
240 – 250
> 250
Hold Values
PD 0,5

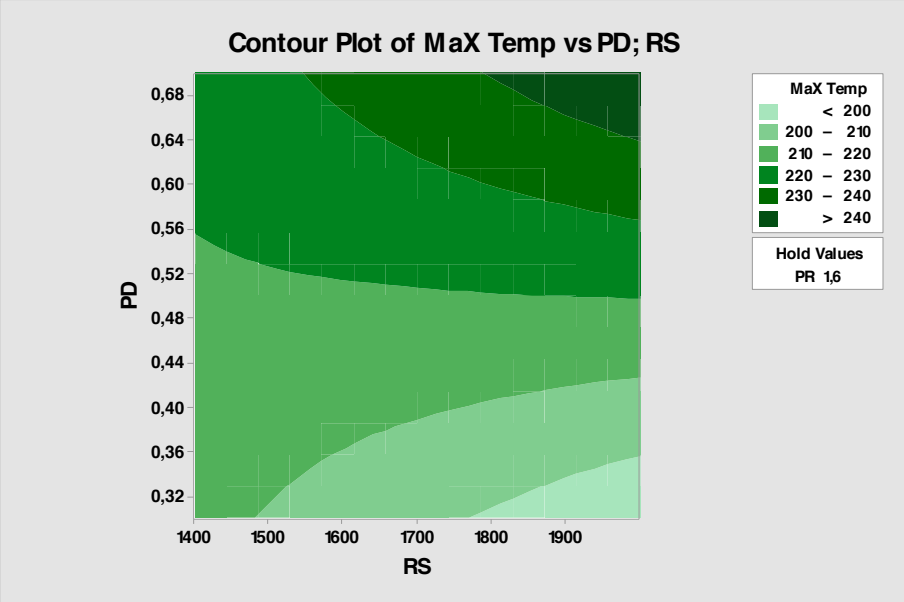
Contour Plot of MaX Temp vs PD; RS
PD
0,68
0,64
0,60
0,56
0,52
0,48
0,44
0,40
0,36
0,32
1400
1500
1600
1700
1800
1900
RS
MaX Temp
< 200
200 – 210
210 – 220
220 – 230
230 – 240
> 240
Hold Values
PR 1,6

APPENDIX D

Note: The acronym "PR" refers to the definition of *Plunge Rate*, which is equivalent Plunge Speed.

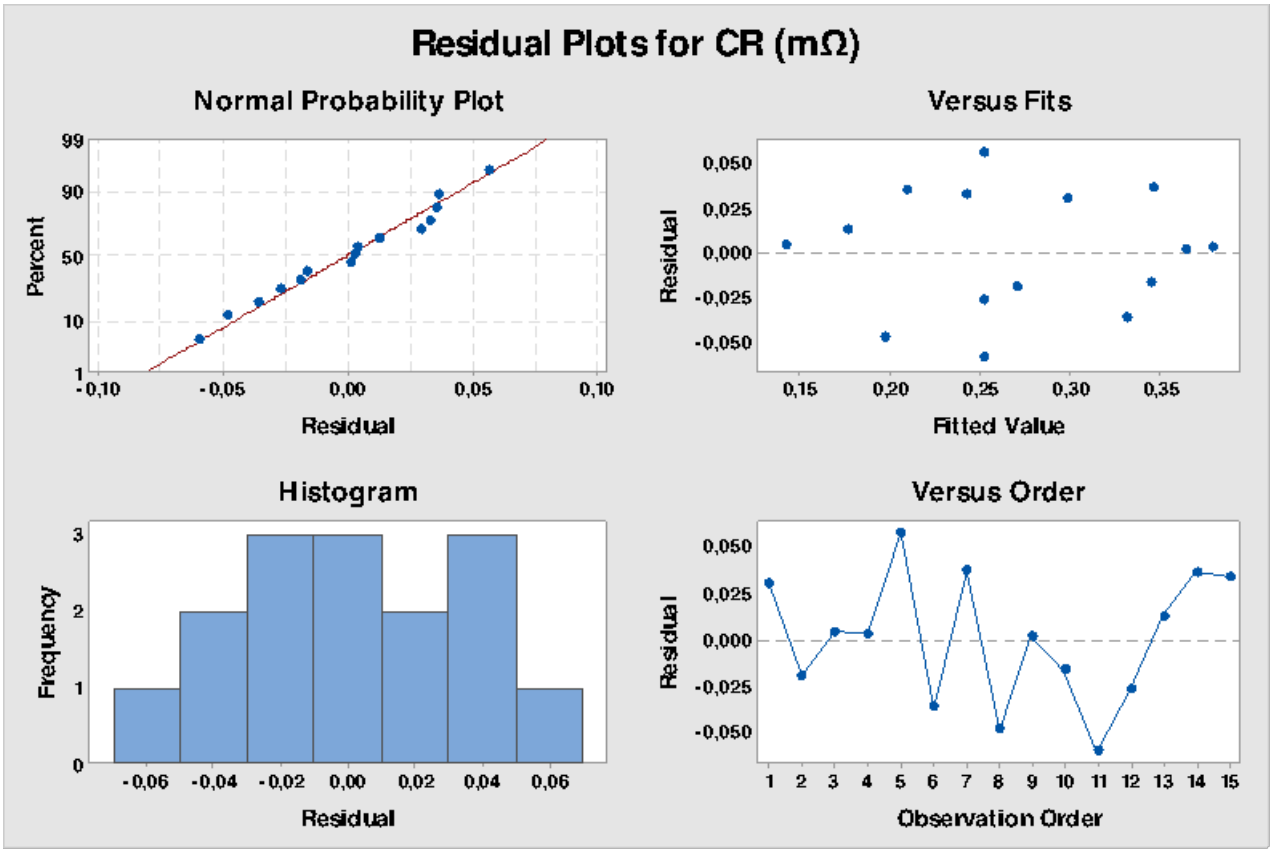

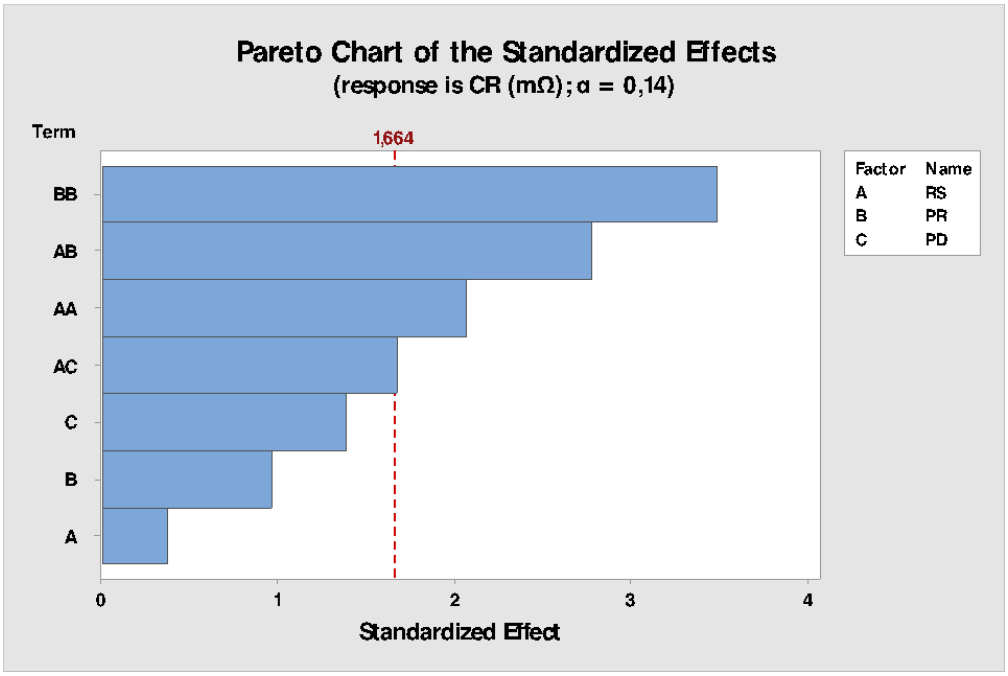

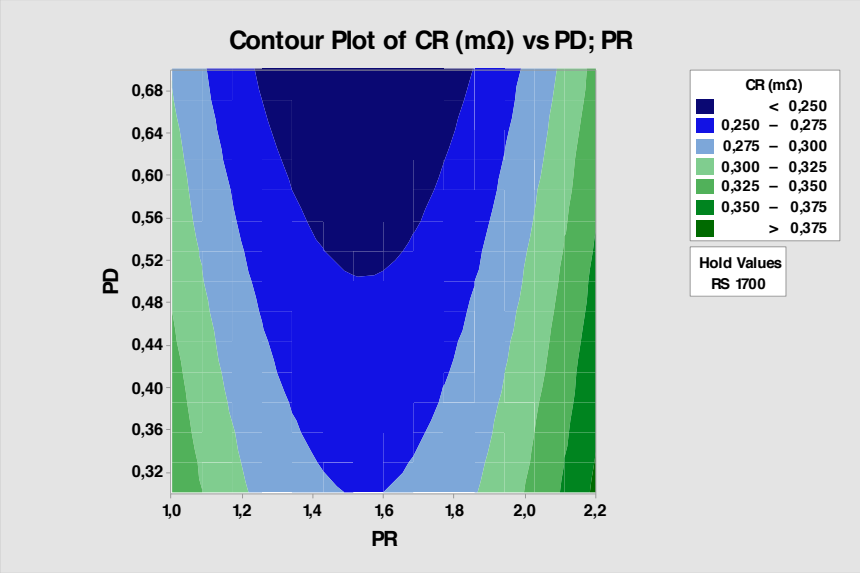
Contour Plot of CR (mΩ) vs PD; PR
PD
PR
0,68
0,64
0,60
0,56
0,52
0,48
0,44
0,40
0,36
0,32
1,0
1,2
1,4
1,6
1,8
2,0
2,2
CR (mΩ)
< 0,250
0,250 – 0,275
0,275 – 0,300
0,300 – 0,325
0,325 – 0,350
0,350 – 0,375
> 0,375
Hold Values
RS 1700

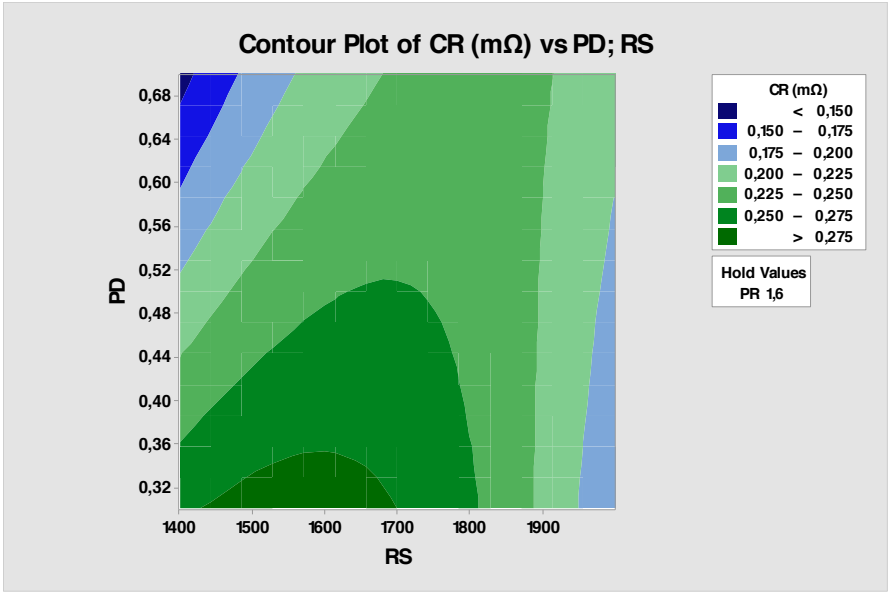
Contour Plot of CR (mΩ) vs PD; RS
PD
RS
0,68
0,64
0,60
0,56
0,52
0,48
0,44
0,40
0,36
0,32
1400
1500
1600
1700
1800
1900
CR (mΩ)
< 0,150
0,150 – 0,175
0,175 – 0,200
0,200 – 0,225
0,225 – 0,250
0,250 – 0,275
> 0,275
Hold Values
PR 1,6

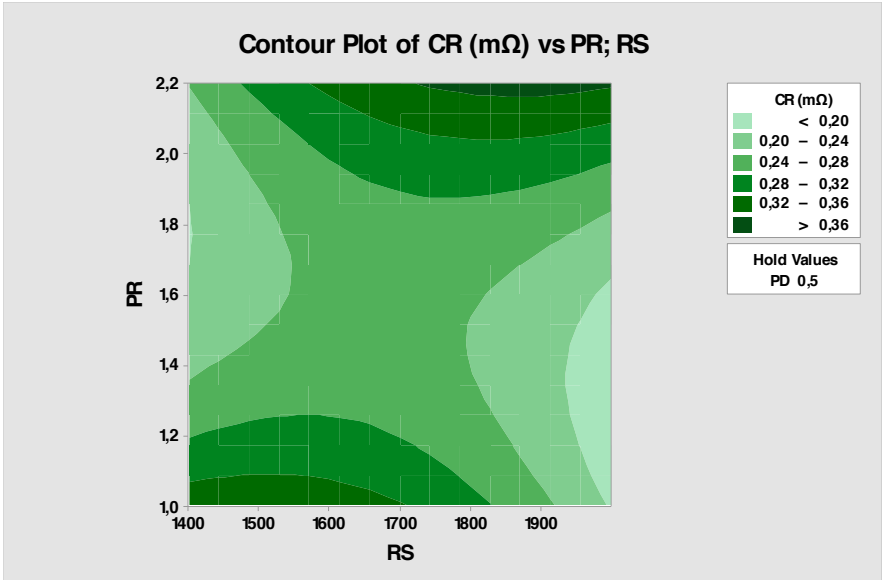
Contour Plot of CR (mΩ) vs PR; RS
PR
RS
2,2
2,0
1,8
1,6
1,4
1,2
1,0
1400
1500
1600
1700
1800
1900
CR (mΩ)
< 0,20
0,20 – 0,24
0,24 – 0,28
0,28 – 0,32
0,32 – 0,36
> 0,36
Hold Values
PD 0,5